ABSTRACT

HU, HENGRUI. A Hybrid Finite-Volume-Finite-Difference Scheme and Augmented Method for Chemotaxis System. (Under the direction of Alina Chertock.)

In this dissertation, we work on the numerical solutions for two models which are encountered in biological studies.

We start with the Patlak-Kelle-Segel chemotaxis system and related models, and develop both the second-order and fourth-order positivity-preserving hybrid finite-volume-finite-difference scheme for this type of system. The new schemes combined the finite difference scheme and the finite-volume scheme which based on modifications of a Godunov-type upwind method. We demonstrate high-accuracy, stability and computational efficiency of the proposed schemes in a number of numerical examples.

In the second part, we focus on the chemotaxis-fluid model defined in an irregular domain (the domain with curve boundary) and derived a second-order positivity-preserving finite-volume-finite-difference scheme for this system. A finite-volume upwind scheme is applied to evolve the chemotaxis part of the system, while the fluid equations are solved by a finite-difference scheme, and both of the finite-volume and finite-difference schemes involved in the proposed scheme are modified by the immersed interface method and augmented technique to work for the irregular domain problem. The performance of the new scheme is studied by a number of numerical examples.

A Hybrid Finite-Volume-Finite-Difference Scheme
and Augmented Method for Chemotaxis System

by
Hengrui Hu

A dissertation submitted to the Graduate Faculty of
North Carolina State University
in partial fulfillment of the
requirements for the Degree of
Doctor of Philosophy

Applied Mathematics

Raleigh, North Carolina

2022

APPROVED BY:

Mansoor Haider	Zhilin Li
Semyon Tsynkov	Hien Tran

Alina Chertock
Chair of Advisory Committee

DEDICATION

To my parents, whose constant support and love made this possible.

BIOGRAPHY

Hengrui Hu was borm in Suining, a small but beautiful town in China on April 27, 1990. Hengrui achieved the Bachelor degree from Sichuan University in 2011. After graduating, in Fall 2012, Hengrui joined the North Carolina State University to pursue Phd degree in Applied Math. He plans to graduate in 2022 after study in Dr. Chertock's group for few years. And after the Phd study, he plans to go to industry/technology company for another research journey.

ACKNOWLEDGEMENTS

TABLE OF CONTENTS

LIST OF TABLES

LIST OF FIGURES

CHAPTER

1

INTRODUCTION

In this dissertation, we study two different sets of systems which encountered in biological studies.

The first part of the dissertation is devoted to the development of the finite-volume-finite-difference (FVFD) method for the Patlak-Keller-Segel (PKS) chemotaxis system and related models. In the second part, we focus on a different type of system called chemotaxis-fluid system, which models the motion of swimming bacteria, so called Bacillus subtilis, living in fluid and consume oxygen. In this chapter, we briefly introduce the overview of these two models and the idea of numerical schemes for these models.

1.1 Patlak-Keller-Segel model

Chemotaxis refers to mechanisms by which cellular motion occurs in response to an external stimulus, usually a chemical one. Chemotaxis phenomenon plays an important role in bacterial aggregation and pattern formation mechanisms, as well as in tumor growth. The description of chemotaxis was first made by T W. Engelmann (1881) and W.F. Pfeffer (1884) in bacteria and H.S. Jennings (1906) in ciliates. The well-known Patlak-Keller-Segel (PKS) system introduced in (67; 68; 69; 110) is widely used for chemotaxis, this classic PDE model is governed by a system of advection-diffusion-reaction equations, which in the two-dimensional (2-D) case read as:

$$\begin{cases} \rho_t + \nabla \cdot (\chi \rho \nabla c) = \mu \Delta \rho, \\ \alpha c_t = D \Delta c - \gamma_c c + \gamma_\rho \rho, \end{cases} \quad (x, y) \in \Omega \subset \mathbb{R}^2, \ t \geq 0, \tag{1.1}$$

where $\rho(x, y, t)$ stands for the density of the bacteria, $c(x, y, t)$ denotes the concentration of the chemoattractant, $\chi > 0$ is a chemotactic sensitivity constant, μ and D are the diffusion coefficient for bacteria and chemoattractant respectively, $\gamma_\rho > 0$ and $\gamma_c > 0$ are the reaction coefficients represent the production and degradation rate of the chemoattractant. The parameter α is equal to either 1 or 0, which correspond to the parabolic-parabolic or reduced parabolic-elliptic coupling, respectively.

The PKS system Eq. 1.1 can be generalized by taking into account additional factors such as growth and death of the bacteria, presence of food or other chemicals in the system and production of the chemoattractant by the bacteria (see, e.g., (123; 122)). One may also consider a more realistic and complicated chemotactic sensitivity function $\chi = \chi(\rho, c)$ as in (57; 67) instead of just using a sensitivity constant.

Chemotaxis systems have been widely used and extensively analyzed (see, e.g., (56; 58;

2

63; 64; 112) and references therein) in the past few decades. An important common property of all the chemotaxis models is their ability to model a concentration phenomenon that mathematically leads to rapid growth of solutions in small neighborhoods of concentration points. The solutions may blow up or exhibit a very singular, spiky behavior depend on the spatial dimension and the total mass, which is conserved under the assumption that no-flux boundary conditions are imposed:

$$M := \int_{\Omega} \rho(x,y,t) dx dy = \int_{\Omega} \rho(x,y,0) dx dy. \tag{1.2}$$

In one-dimensional space case, the global solution of Eq. 1.1 exists, and converges to a stationary solution as $t \to \infty$. In two-dimensional space, it was proved that, provided the total mass of cells is below a critical threshold M_c, the solution of Eq. 1.1 exists globally in time. Otherwise, the solution blows-up in finite time (see, e.g., (19; 63; 64; 111)). In the parabolic-elliptic case ($\alpha = 0$), the threshold $M_c = \frac{8\pi}{\chi}$. In the parabolic-parabolic case ($\alpha = 1$), the solution globally exists in time and its $L^{\infty}-$norm is uniformly bounded for all time if the total mass $M < \frac{4\pi}{\chi}$, if the total mass $\frac{4\pi}{\chi} < M < \frac{8\pi}{\chi}$, the solution may blow up at the boundary of the domain Ω, and the blow-up may occurs in the solution if the total mass $M > \frac{8\pi}{\chi}$. This blow-up of solution is termed as chemotatic collapse, and it mathematically describes a bacteria concentration phenomenon that occurs in real biological experiments (see, e.g., (1; 12; 17; 18; 24; 30; 104; 113)).

While the blow-up is a reasonable model of the bacterial aggregation, it creates enormous challenges to both numerical and analytical study. And in order to get rid of the blow-up in solution, a lot of regularizations of the PKS model Eq. 1.1, which admit bounded and global-in-time solution, have been introduced in the literature. Most of the regularized

3

models can be read as the following form:

$$\begin{cases} \rho_t + \nabla \cdot (g(\rho)\, \mathbf{Q}(\chi, \nabla c)) = \mu \Delta \rho, \\ \alpha c_t = D \Delta c - \gamma_c c + \gamma_\rho \rho, \end{cases} \tag{1.3}$$

where $g > 0$ and $\mathbf{Q}$ are some smooth functions (see, e.g., (58; 63; 64; 23) and references therein).

For example, the signal-dependent sensitivity model can be obtained by taking

$$g(\rho) = \rho \quad \text{and} \quad \mathbf{Q}(\chi, \nabla c) = \frac{\chi \nabla c}{(1 + \kappa c)^2}, \tag{1.4}$$

the density-dependent sensitivity model can be obtained by setting

$$g(\rho) = \frac{\rho}{1 + \kappa \rho} \quad \text{and} \quad \mathbf{Q}(\chi, \nabla c) = \chi \nabla c, \tag{1.5}$$

where κ is a small regularization parameter and these models converges to the PKS system Eq. 1.1 as $\kappa \to 0$. There exists a global bounded solution for these models, and the regularization parameter κ makes it possible to conduct a detailed analysis and investigate properties of solutions (see, e.g., (127; 128)).

A saturated chemotactic flux model was introduced in (23), with the following g and $\mathbf{Q}$:

$$g(\rho) = \rho, \quad \text{and} \quad \mathbf{Q}(\chi, \nabla \mathbf{c}) = \begin{cases} \chi \nabla c, & \text{if } |\nabla c| \le s^*, \\ \left(\dfrac{\chi |\nabla c| - s^*}{\sqrt{1 + (\chi |\nabla c| - s^*)^2}} + s^* \right) \dfrac{\nabla c}{|\nabla c|}, & \text{otherwise,} \end{cases} \tag{1.6}$$

where s^* is a switching parameter that defines small gradient values. so that the saturated chemotactic flux function affect only large gradient regimes. For small gradient regimes, the

system Eq. 1.6 reduces to the PKS model Eq. 1.1. The solution for this saturated chemotactic flux model is spiky but bounded (see, e.g., (23; 75)).

The multi-component chemotaxis model is also widely discussed (see, e.g., (41; 42; 43; 130)). A mathematical model for two noncompetitive species was propose in (130), in two dimensional case, this two species chemotaxis model is written as following:

$$
\begin{cases}
(\rho 1)_t + \nabla \cdot (\chi_1 \rho_1 \nabla c) = \mu_1 \Delta \rho_1, \\
(\rho 2)_t + \nabla \cdot (\chi_2 \rho_2 \nabla c) = \mu_2 \Delta \rho_2, \qquad (x, y) \in \Omega \subset \mathbb{R}^2, \ t \geq 0, \\
\alpha c_t = D \Delta c + \gamma_{\rho_1} \rho_1 + \gamma_{\rho_2} \rho_2 - \gamma_c c,
\end{cases}
\tag{1.7}
$$

Here in Eq. 1.7, $\rho_1(x, y, t)$ and $\rho_2(x, y, t)$ denote the cell densities of the first and second species, $c(x, y, t)$ stands for the chemoattractant concentration, $\chi_2 > \chi_1$ are the chemotactic sensitivities, positive constants μ_1 and μ_2 are diffusion coefficients, γ_{ρ_1} and γ_{ρ_2} are the production rates for the first and second species, γ_c is the consumption rate.

Performing a dimensional analysis introduced by ESpejo in (44), the system Eq. 1.7 reduces to

$$
\begin{cases}
(\rho 1)_t + \nabla \cdot (\chi_1 \rho_1 \nabla c) = \mu_1 \Delta \rho_1, \\
(\rho 2)_t + \nabla \cdot (\chi_2 \rho_2 \nabla c) = \Delta \rho_2, \qquad (x, y) \in \Omega \subset \mathbb{R}^2, \ t \geq 0, \\
\epsilon c_t = \Delta c + \gamma_{\rho_1} \rho_1 + \gamma_{\rho_2} \rho_2 - \gamma_c c,
\end{cases}
\tag{1.8}
$$

where $\epsilon = \frac{\mu_1}{D}$. On the other hand, the molecular diffusion is much faster than the cell diffusion ($\mu_1 \ll D$), so it's natural to assume that $\epsilon \approx 0$ and obtain the following system:

$$
\begin{cases}
(\rho 1)_t + \nabla \cdot (\chi_1 \rho_1 \nabla c) = \mu_1 \Delta \rho_1, \\
(\rho 2)_t + \nabla \cdot (\chi_2 \rho_2 \nabla c) = \Delta \rho_2, \qquad (x, y) \in \Omega \subset \mathbb{R}^2, \ t \geq 0, \\
\Delta c + \gamma_{\rho_1} \rho_1 + \gamma_{\rho_2} \rho_2 - \gamma_c c = 0,
\end{cases}
\tag{1.9}
$$

Like the classical PKS system, solutions of Eq. 1.9 may either remain smooth (with decaying maxima of both ρ_1 and ρ_2) or blow up in a finite time. Moreover, only simultaneous blowup is possible (see, e.g. (41; 43)). However, in the blowup regime ρ_1 and ρ_2 may develop different types of singularities depending on the values of χ_1 and χ_2 and on the total mass of each species:

$$m_1 := \int_\Omega \rho_1(x, y, 0) d x d y \quad \text{and} \quad m_2 := \int_\Omega \rho_2(x, y, 0) d x d y. \tag{1.10}$$

It was proven in (41; 43) that the global solution exists if

$$\frac{8\pi \mu_1 m_1}{\chi_1} + \frac{8\pi m_2}{\chi_2} - (m_1 + m_2)^2 \geq 0 \quad \text{and} \quad m_2 \leq \frac{8\pi}{\chi_2}, \tag{1.11}$$

that the solution ρ_2 blows up faster than ρ_1 if

$$\frac{8\pi \mu_1 m_1}{\chi_1} + \frac{8\pi m_2}{\chi_2} - (m_1 + m_2)^2 \leq 0 \quad \text{and} \quad m_1 + m_2 \leq \frac{8\pi}{\chi_1}, \tag{1.12}$$

that the solutions ρ_1 and ρ_2 blow up at the same rate if

$$m_1 + m_2 > \frac{8\pi}{\chi_1}, \tag{1.13}$$

and for

$$\frac{8\pi \mu_1 m_1}{\chi_1} + \frac{8\pi m_2}{\chi_2} - (m_1 + m_2)^2 \geq 0 \quad \text{and} \quad m_2 > \frac{8\pi}{\chi_2}, \tag{1.14}$$

the question on the behavior of the solution remains open.

The chemotaxis term in PKS model Eq. 1.1 and Eq. 1.7 is highly nonlinear, and the diffusion term has infinite propagation speed in the context of the solution, therefore capturing blowing up or spiky solutions numerically is a very challenging task. It's difficult to guarantee nonlinear stability of the numerical method since the convective part of chemotaxis

6

system may loose hyperbolicity. In many other models, appearance of small negative values is numerically acceptable, but in the chemotaxis models, even the small negative values in numerical solution ρ will lead to the spikes of negative bacteria density, which makes the numerical solution totally irrelevant. So preserving positivity in the numerical solutions is crucial for a good numerical scheme since it is the only way to enforce the nonlinear stability. At the same time an accurate and efficient numerical method is important for the modeling and analysis of chemotaxis systems. Let us briefly review some of the numerical methods that have been proposed in the literature.

A finite-volume, (47), and finite-element, (100; 117), methods have been proposed for the PKS system with the parabolic-elliptic coupling, that is, the system Eq. 1.1 with $\alpha = 0$ using an assumption that the chemoattractant concentration c changes over much smaller time scales than the bacteria density ρ. A fractional step numerical method for fully time-dependent chemotaxis system from (123; 131) has been proposed in (124). However, the fractional step (operator splitting) approach may not be applicable for the system Eq. 1.1 since the convective part of the chemotaxis system may loose the hyperbolicity. As it has been demonstrated in (22), the latter is a generic situation for the PKS model with parabolic-parabolic ($\alpha = 1$) coupling. Several methods for the parabolic-parabolic PKS system have been recently proposed: a family of high-order discontinuous Galerkin methods has been designed in (39; 40); an implicit flux-corrected finite-element method has been developed in (119). These methods achieve high-order of accuracy, but their high memory usage and computational costs are of obvious drawbacks. A simpler and more efficient second-order finite-volume central-upwind scheme has been derived in (22) for the PKS system with $\alpha = 1$ and extended to several more realistic chemotaxis and related models. Finally, in (38) a modified version of the scheme from (22) is extended to PKS system in irregular geometry by employing the idea of the difference potentials.

7

1.2 Chemotaxis-Fluid model

Bioconvection patterns are a collective phenomenon and usually appear in shallow suspensions of upward swimming micro-organisms that are a little bit denser than water. When the upper regions of the suspensions becomes sufficiently dense due to the gathering of the micro-organisms, Rayleigh-Taylor-type instability occurs and the micro-organisms fall down. Oxytactic bacteria, such as *Bacillus subtilis*, which can swim up oxygen gradients, is commonly used in bioconvection experiments.

The chemotaxis-fluid system has been proposed in (60) to describe the bio-convection in modestly diluted cell suspensions under the assumptions that the contribution of the bacteria to the density of the suspension is small and the interactions between cells are neglected. This model couples a convective chemotaxis system with the incompressible Navier-Stokes equation. In the two-dimensional (2-D) case, the chemotaxis-fluid system can be written as:

$$
\begin{cases}
\rho_t + \mathbf{u}\cdot\nabla\rho + \chi\nabla\cdot\big[\rho\,r(c)\nabla c\big] = D_\rho\Delta\rho, \\[2mm]
c_t + \mathbf{u}\cdot\nabla c = D_c\Delta c - \rho\kappa r(c), \\[2mm]
\hat{\rho}(\mathbf{u}_t + \mathbf{u}\cdot\nabla\mathbf{u}) + \nabla p = \eta\Delta\mathbf{u} - \rho\nabla\Phi, \\[2mm]
\nabla\cdot\mathbf{u} = 0,
\end{cases}
\qquad (x,y)\in\Omega\subset\mathbb{R}^2,\ \ t\geq 0, \qquad (1.15)
$$

where $\rho(x,y,t)$ stands for the concentration of bacteria, $c(x,y,t)$ denote the chemoattractant (oxygen) concentration, $\chi > 0$ is a chemotactic sensitivity constant, κ is the oxygen consumption rate, and $\mathbf{u}$ is the velocity field of the fluid flow, with fluid density $\hat{\rho}$, pressure p and viscosity η, D_ρ and D_c are the diffusion coefficient for bacteria and oxygen, respectively. The source term $\rho\nabla\Phi := \rho\,V_b g(\rho_b - \hat{\rho})z$ in the fluid equation describes the gravity exerted by the bacterium onto the fluid, which is along the upward direction z and proportional to

the volume of the bacterium V_b, $g = 9.8m/s^2$ is the gravitation acceleration and the density of bacteria is ρ_b, which is a littler denser than water.

In Eq. 1.15, the oxygen concentration c and the bacterial concentration ρ diffuse with their diffusion constant D_ρ and D_c arise from the random swimming trajectories respectively, and convected with the fluid. The dimensionless cut-off function $r(c)$ models the inactivity threshold of the bacteria due to the low oxygen concentration, approaching unity for large c and vanishing rapidly for c below the inactivity threshold c^*. Experiments conducted by Tuval (see, e.g., (121)) suggest that we can use a step function $r(c) = \theta(c - c^*)$ to model the cut-off function. The oxygen consumed is proportional to this function $r(c)$ and the concentration of bacteria ρ. In chemotaxis, the bacteria swim to the high oxygen concentration region with a velocity proportional to the gradient of the oxygen, and depending on the chemotactic sensitivity χ and motility function $r(c)$. We remark that, unlike the Keller-Segel model, that the oxygen is consumed by the bacteria in this model Eq. 1.15, instead of produced by the bacteria. In particular, the system Eq. 1.15 describes the experiments conducted by Hillesdon et al. (see, e.g., (60)) with a suspension of *Bacillus subtilis* in a water chamber. In these experiments, the initial suspension is well stirred, the oxygen diffuses through the top water-air surface, the oxytactic bacteria, which consume oxygen, will swim up the oxygen gradient and concentrate below the surface, so a high concentration layer can be observed near the top water-air surface. The bacteria consume the oxygen and ,in some areas, the oxygen concentration will fall below the threshold c^* and the bacteria become inactive in these areas. Since the bacteria are a little bit denser than water, instabilities occur in the high concentration layer and will form some mushroom-shaped plumes that sink downward. The linear stability of the system Eq. 1.15 was discussed in (59) and the the weakly nonlinear stability was analyzed in (103) .

It has been shown in (98) that, in the three-dimensional case, the weak solutions for

system Eq. 1.15 exist locally, while in the two-dimensional case, the local existence of the weak solutions is proved under the assumption that the motion of the fluid is slow, which is for Stokes equation instead of Navier-Stokes equation. Global existence of the weak solutions for system Eq. 1.15 was proved in (Duan et al.), in the three-dimensional case, the global existence result was obtained, while in two dimensional case, the global existence is proved for Chemotaxis-Stokes system with finite bacteria mass $M_\rho := \int_\Omega \rho(x, y, 0) dx dy$ and small initial oxygen concentration c. Global existence and the asymptotic behavior of the Chemotaxis-Stokes system with nonlinear bacteria diffusion term was discussed in (Di Francesco et al.). Global existence for Chemotaxis-Navier-Stokes system in two-dimensional case with large date was obtained in (96).

Several numerical methods for chemotaxis-fluid system have been proposed in the literature. A conservative finite-difference method for a narrow, tall domain with a rigid bottom, a stress-free top and lateral boundaries in two-dimensional space has been developed in (49). A particle method coupled with a finite-volume method has been proposed in (62), which discretely represents the bacteria by individual particles instead of by continuous bacteria concentration and numerically solves the chemical transport equation and Navier-Stokes equation by a finite-volume method. A finite-volume-finite-difference method for the chemotaxis-fluid system Eq. 1.15 in a rectangular two-dimensional domain has been derived in (21), which discretizes the chemotaxis equations by a finite-volume upwind scheme, and solves the Navier-Stokes equations in vorticity form by applying a finite-difference method.

Particularly, in this dissertation, we focus on the the system Eq. 1.15 defined in a two-dimensional domain Ω with a curved boundary on the top part (see figure Fig. 1.2). This system was proposed in Tuval *et al.*(121) to describe experiments with a quasi-two-dimensional suspension of the swimming bacteria *Bacillus subtulis* in a water drop on a piece of glass

(see figure Fig. 1.1).
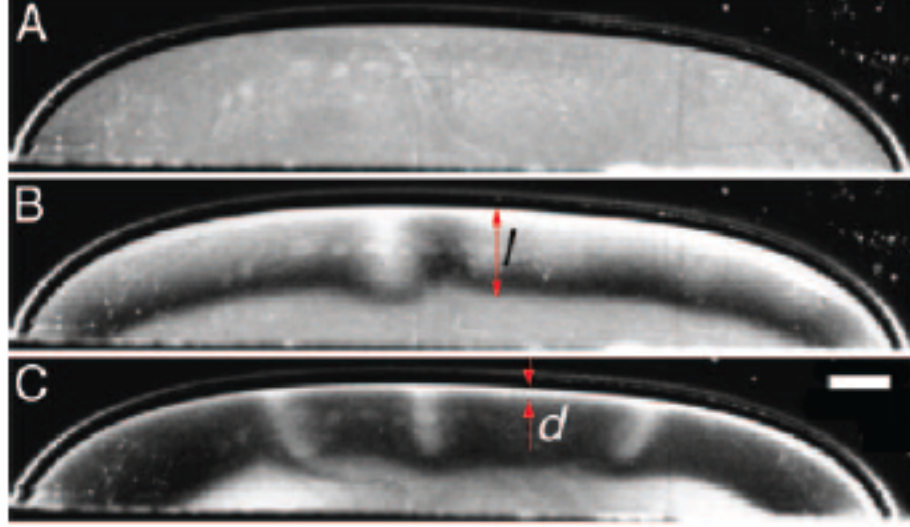
Figure 1.1:   Experimental observation of stages to self-concentration in a sessile drop from Tuval et al.(121). Initially it's a well-mixed drop on a piece of glass. First, the bacterials swim up to the fluid-air surface form a high-concentration layer near the surface. Later, due to the gravitational force and consumption of the oxygen, the instabilities form at the this layer and plumes begin to sink downward.

At the top fluid-air surface $\partial\Omega_{top}$, there is no flux of bacteria through this fluid-air interface, the oxygen concentration is assumed to be the same as the oxygen concentration in air c_{air} since the oxygen diffuse much faster in the air than in the fluid (about three orders of magnitude faster), and the surface is stress free, which leads to the normal direction fluid velocity, and the tangential fluid stress equal to zero:

$$\chi\rho r(c)c_{\mathbf{n}} - D_\rho\rho_{\mathbf{n}} = 0, \quad c = c_{air}, \quad \mathbf{u}\cdot\mathbf{n} = 0, \quad (\mathbf{n}\cdot(\nabla\mathbf{u} + \nabla\mathbf{u}^T))\times\mathbf{n} = 0, \quad \forall(x,y)\in\partial\Omega_{top}. \quad (1.16)$$

In Eq. 1.16, $\mathbf{n}$ and τ are the unit normal and tangential direction respectively. At the bottom

fluid-glass interface $\partial\Omega_{bot}$, there is no fluxes of both bacterial and oxygen, and the fluid velocity is assumed to be zero:

$$\rho_y = c_y = 0, \ \mathbf{u} = \mathbf{0}, \ \ \forall (x, y) \in \partial\Omega_{bot}. \tag{1.17}$$
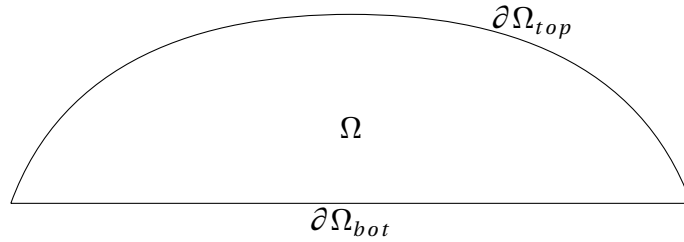
Figure 1.2: The exact domain Ω of the chemotaxis-fluid system Eq. 1.15 introduced in (121) with curve top boundary $\partial\Omega_{top}$

1.3 Finite-volume method for conservation/balance law

Finite-volume methods are widely used to numerically solve hyperbolic conservation/balance laws. Solutions of such systems may break down and develop nonsmooth structures such as shock waves, rarefaction waves and singular δ-shocks even when the initial data are smooth. The finite-volume method is a reconstruction-evolution-projection method, at some certain time t, reconstructs a global solution from the cell-averages, evolves in time based on the integral form of the conservation law and then projects back to the original grid to get the solution at next time level.

As a simple example, consider the one-dimensional conservation law:

$$q(x,t)_t + f(q)_x = 0, \quad x \in \mathbb{R}, \ t \geq 0. \tag{1.18}$$

Introduce small scales in both space (Δx) and time (Δt), and integrate the conservation law with respect to x and t over the control volume $[x - \frac{\Delta x}{2}, x + \frac{\Delta x}{2}] \times [t, t + \Delta t]$:

$$\int_t^{t+\Delta t} \int_{x-\frac{\Delta x}{2}}^{x+\frac{\Delta x}{2}} q(\xi, \tau)_\tau \, d\xi \, d\tau + \int_t^{t+\Delta t} \int_{x-\frac{\Delta x}{2}}^{x+\frac{\Delta x}{2}} f\big(q(\xi, \tau)\big)_\xi \, d\xi \, d\tau. \tag{1.19}$$

Define the cell averages of q:

$$\overline{q}(x,t) := \frac{1}{\Delta x} \int_{x-\frac{\Delta x}{2}}^{x+\frac{\Delta x}{2}} q(\xi, t) \, d\xi, \tag{1.20}$$

and the averaged fluxes:

$$F(x,t) := \frac{1}{\Delta t} \int_t^{t+\Delta t} f\big(q(x, \tau)\big) \, d\tau, \tag{1.21}$$

then Eq. 1.19 gives us the finite-volume scheme:

$$\overline{q}(x, t+\Delta t) = \overline{q}(x, t) - \frac{\Delta t}{\Delta x} \Big(F(x + \frac{\Delta x}{2}, t) - F(x - \frac{\Delta x}{2}, t) \Big). \tag{1.22}$$

Introducing a spatial grid $\{x_j\}$ such that

$$x_{j+1} - x_j = \Delta x, \quad x_{j-\frac{1}{2}} = x_j - \frac{\Delta x}{2}, \quad x_{j+\frac{1}{2}} = x_j + \frac{\Delta x}{2} \tag{1.23}$$

and the computational cells

$$I_j := [x_{j-\frac{1}{2}}, x_{j+\frac{1}{2}}].$$

The finite-volume schemes can be mainly split into two cases, central and upwind, depending on the setting of control volume.
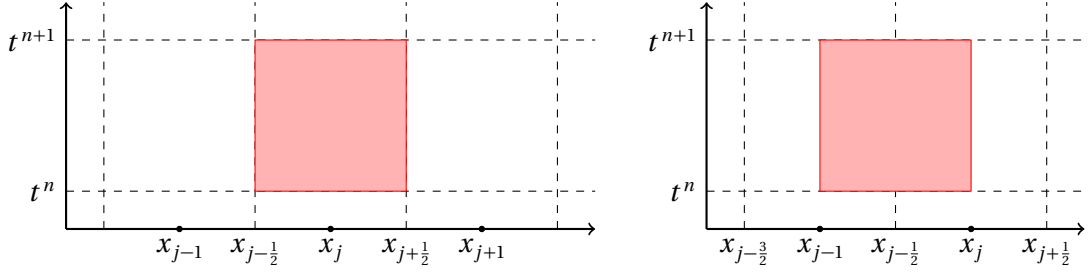
Figure 1.3: Space-time control volumes: upwind (left) and central (right) settings

For any time $t = t^n$, define $t^{n+1} = t^n + \Delta t$, in the upwind schemes, choosing the control volume $[x_{j-\frac{1}{2}}, x_{j+\frac{1}{2}}] \times [t^n, t^{n+1}]$, the cell averages $\overline{q}_j^{n+1}$ at time t^{n+1} can be obtained by:

$$\overline{q}_j^{n+1} = \overline{q}_j^n - \frac{\Delta t}{\Delta x}\left(F_{j+\frac{1}{2}}^n - F_{j-\frac{1}{2}}^n\right), \tag{1.24}$$

where

$$\overline{q}_j^n \approx \frac{1}{\Delta x} \int_{I_j} q(x, t^n) dx,$$

$$F_{j+\frac{1}{2}}^n \approx \frac{1}{\Delta t} \int_{t^n}^{t^{n+1}} f(q(x_{j+\frac{1}{2}}, t)) dt. \tag{1.25}$$

Since the solution cell averages $\overline{q}_j^n$ are constant in each computational cell I_j, and discontinuous at cell interface $x = x_{j+\frac{1}{2}}$, the numerical fluxes $F_{j+\frac{1}{2}}^n$ can be obtained by solving a Riemann problem at each cell interface (see, e.g., (51; 50; 71; 118; 13)). Thus, these upwind schemes are restricted to the systems for which an explicit formula for the solutions of the

Riemann problem is available.

On the other hand, the central schemes allow one to solve the system without solving Riemann problem. It is obtained using the same finite-volume evolution equation Eq. 1.22, but the space-time control volumes are $[x_j, x_{j+1}] \times [t^n, t^{n+1}]$:

$$\overline{q}_{j+\frac{1}{2}}^{n+1} = \frac{1}{2\Delta x}\left(\int_{x_j}^{x_{j+\frac{1}{2}}} \widetilde{q}_j^n(x)dx + \int_{x_{j+\frac{1}{2}}}^{x_{j+1}} \widetilde{q}_{j+1}^n(x)dx\right) - \frac{1}{\Delta x}\int_{t^n}^{t^{n+1}} \left[F\big(q(x_{j+1}, t)\big) - F\big(q(x_j, t)\big)\right]dt,$$

(1.26)

where $\widetilde{q}_j^n(x)$ is a piecewise function constructed from the cell averages. As long as a suitable CFL condition is chosen and no waves generated at the cell interfaces will reach the vertical segment, the solution remains constant at $x = x_j$, so the flux integrals can be exactly evaluated, and it is clear that the space integrals can be also exactly computed in a straightforward manner. The central scheme is simple and universal to solve hyperbolic systems of conservation laws due to the feature that no Riemann solver is required, but it may have a larger numerical dissipation and excessive numerical diffusion since it does not catch the resolution of nonlinear waves. Central schemes have been broadly developed including higher-order methods, multidimensional generalizations and staggered and nonstaggered grids (see, e.g., (48; 84; 105; 3; 66; 97; 10; 86; 95; 72; 76; 81; 82; 77; 107; 93; 116; 108; 109; 28)).

Recently, a new Godunov-type finite-volume method, central-upwind (CU) scheme, has been developed. The central-upwind scheme combines the high accuracy and low dissipation of the upwind scheme with the universality and simplicity of the central scheme. The key idea of the CU schemes is to select space-time control volumes in the evolution step adaptively depending on the size of Riemann fans generated at each cell interfaces, more precisely the speeds of propagation of waves at each cell interface. Based on these propagation speeds, one can choose two sets of control volumes (see figure Fig. 1.4). One contains the smooth part of the solution (the red part in Fig. 1.4), and the other contains all

15

nonlinear waves from each cell interface (the blue part in Fig. 1.4). Same as central schemes, one can always choose a proper time step which guarantee that no waves generated at cell interfaces reach the boundaries of the control volumes, thus the evolution in the control volume remains central and can be obtained in a straightforward manner.
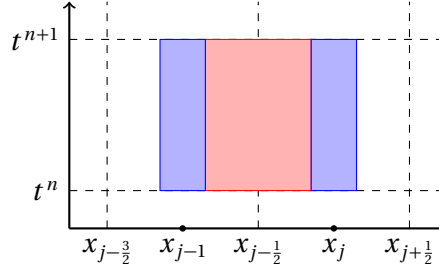
Figure 1.4: Space-time control volumes for central-upwind method

The central-upwind schemes for systems of hyperbolic conservation laws were initially posted in (81), and have been developed including multudimensional and higher-order methods (see, e.g., (77; 16; 78; 15; 79; 32; 80; 73)). These CU schemes can capture the resolution of nonlinear waves and reduce the numerical dissipation, and can be widely applied to solve the hyperbolic systems of conservation laws due to the Riemann-solver-free feature.

1.4 Immersed interface method and augmented technique

Interface problems occur in a lot of applications, for example, when there are two different kinds of materials or the same material at different states, we are dealing with an interface problem. Mathematically, the interface problem is usually modeled by a partial-differential-equation (PDE) system defined on a domain divided into several parts by some interfaces.

The input data such as the parameters and source terms in the PDE system may be discontinuous or even singular across the interfaces. Due to these irregularities, the solution to an interface problem is typically non-smooth or even discontinuous.

Immersed interface methods (see, e.g., (87; 85; 89; 90)) are developed to numerically solve PDE systems defined in an interfaced domain or a domain with irregular boundarys. For example, consider a Poisson equation defined in a domain $\Omega \subset \mathbb{R}^2$ with a curved boundary $\partial\Omega$:

$$\Delta\phi(x,y) = f(x,y), \quad (x,y) \in \Omega \subset \mathbb{R}^2, \tag{1.27}$$

subject to a Dirichlet boundary condition:

$$\phi(x,y) = g(x,y), \quad (x,y) \in \partial\Omega. \tag{1.28}$$

In order to apply the immersed interface method, we first embed the domain Ω into a rectangular computational domain $\overline{\Omega} = [a,b] \times [c,d]$ which contains Ω as Figure Fig. 1.5 and treat the domain boundary $\partial\Omega$ as an interface inside the rectangular computational domain $\overline{\Omega}$. In the region $\overline{\Omega}\backslash\Omega$, we assume the function $\phi(x,y)$ satisfies the equation

$$\Delta\phi(x,y) = 0. \tag{1.29}$$

This extension leads to an interfaced domain problem:

$$\Delta\phi(x,y) = \begin{cases} f(x,y), & \mathbf{x} \in \Omega, \\ 0, & \mathbf{x} \in \overline{\Omega}\backslash\Omega, \end{cases} \tag{1.30}$$

with the interface condition Eq. 1.28. For simplicity, we denote the solution $\phi(x,y) = \phi^-_{x,y}$ inside domain Ω, and $\phi(x,y) = \phi^+(x,y)$ in the complement of the domain $\overline{\Omega}\backslash\Omega$. The solution
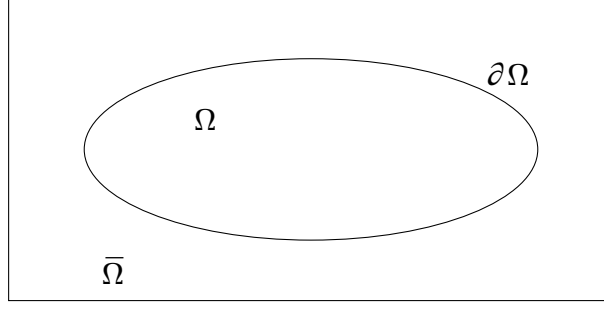
Figure 1.5: The rectangular computational domain $\overline{\Omega}$ which contains the exact elliptic domain Ω of the equation Eq. 1.27.

of this interfaced domain problem Eq. 1.30 may have a discontinuity across the interface $\partial\Omega$, thus we difine jump conditions at a point $\mathbf{X}$ on the interface $\partial\Omega$ as follows:

$$
\begin{aligned}
[\phi]_{\mathbf{x}=\mathbf{X}} &:= \lim_{\mathbf{x}\to\mathbf{X}, \mathbf{x}\in\overline{\Omega}\backslash\Omega} \phi^+(\mathbf{x}) - \lim_{\mathbf{x}\to\mathbf{X}, \mathbf{x}\in\Omega} \phi^-(\mathbf{x}), \\
[\phi_{\mathbf{n}}]_{\mathbf{x}=\mathbf{X}} &:= \lim_{\mathbf{x}\to\mathbf{X}, \mathbf{x}\in\overline{\Omega}\backslash\Omega} \phi_{\mathbf{n}}^+(\mathbf{x}) - \lim_{\mathbf{x}\to\mathbf{X}, \mathbf{x}\in\Omega} \phi_{\mathbf{n}}^-(\mathbf{x}),
\end{aligned}
\tag{1.31}
$$

where $\phi_{\mathbf{n}}(\mathbf{X}) = \frac{\partial\phi}{\partial\mathbf{n}}(\mathbf{X}) = \nabla\phi(\mathbf{X})\cdot\mathbf{n}$ is the normal derivative of ϕ at control point $\mathbf{X}$.

We consider the interfaced domain problem Eq. 1.30 in the computational rectangular domain $\overline{\Omega}\subset\mathbb{R}^2$, where we introduce a Cartesian mesh with $\Delta x = (b-a)/n_x$ and $\Delta y = (d-c)/n_y$, where n_x and n_y are the numbers of grid points used in the x and y direction, respectively. A grid point (x_j, y_k) is called regular if all the neighborhood grid points $(x_{j\pm1}, y_k)$ and $(x_j, y_{k\pm1})$ are located at the same side of the interface, otherwise, the grid point is irregular.

At a regular grid point (x_j, y_k), we approximate the Laplacian by the standard 5-points

stencil, and write a numerical scheme for problem Eq. 1.30 as:

$$\begin{cases} \dfrac{\phi^-_{j+1,k} - 2\phi^-_{j,k} + \phi^-_{j-1,k}}{(\Delta x)^2} + \dfrac{\phi^-_{j,k+1} - 2\phi^-_{j,k} + \phi^-_{j,k-1}}{(\Delta y)^2} = f_{j,k}, & \text{if}(x_j, y_k) \in \Omega, \\[4mm] \dfrac{\phi^+_{j+1,k} - 2\phi^+_{j,k} + \phi^+_{j-1,k}}{(\Delta x)^2} + \dfrac{\phi^+_{j,k+1} - 2\phi^+_{j,k} + \phi^+_{j,k-1}}{(\Delta y)^2} = 0, & \text{if}(x_j, y_k) \in \bar{\Omega}\backslash\Omega, \end{cases} \tag{1.32}$$

where $\phi^\pm_{j,k} = \phi^\pm(x_j, y_k)$ and $f_{j,k} = f(x_j, y_k)$.

At an irregular grid point (x_j, y_k), we assume the interface $\partial\Omega$ and the mesh intersect at (α, y_k) and (x_j, β) as shown in Figure Eq. 1.6.
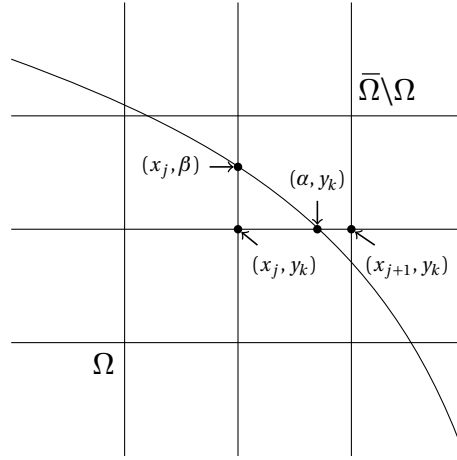
Figure 1.6: The irregular grid point (x_j, y_k), the interface $\partial\Omega$ intersect with the mesh at (α, y_k) and (x_j, β)

The central difference approximation for $\phi^-_{xx}(x_j, y_k)$ is:

$$\phi^-_{xx}(x_j, y_k) = \frac{\phi^-_{j+1,k} - 2\phi^-_{j,k} + \phi^-_{j-1,k}}{(\Delta x)^2}. \tag{1.33}$$

As shown in Figure Fig. 1.6, the grid point (x_{j+1}, y_k) is located outside the domain Ω, and the solution ϕ^- at this point $\phi^-_{j+1,k}$ is not defined. So, we expand $\phi^-_{j+1,k}$ at the intersection

(α, y_k) by the Taylor expansion, and approximate it using $\phi^+_{j+1,k}$, which is defined, and jump conditions at point (α, y_k):

$$
\begin{aligned}
\phi^-_{j+1,k} &= \phi^-(\alpha, y_k) + (x_{j+1} - \alpha)\phi^-_x(\alpha, y_k) + \frac{(x_{j+1} - \alpha)^2}{2}\phi^-_{xx}(\alpha, y_k) + O(\Delta x^3) \\
&= (\phi^+(\alpha, y_k) - [\phi](\alpha, y_k)) + (x_{j+1} - \alpha)(\phi^+_x(\alpha, y_k) - [\phi_x](\alpha, y_k)) \\
&\quad + \frac{(x_{j+1} - \alpha)^2}{2}(\phi^+_{xx}(\alpha, y_k) - [\phi_{xx}](\alpha, y_k)) + O(\Delta x^3) \\
&= \phi^+_{j+1,k} - \left([\phi](\alpha, y_k) + (x_{j+1} - \alpha)[\phi_x](\alpha, y_k) + \frac{(x_{j+1} - \alpha)^2}{2}[\phi_{xx}](\alpha, y_k)\right) + O(\Delta x^3).
\end{aligned}
$$

(1.34)

Then the central difference approximation for $\phi^-_{xx}(x_j, y_k)$ in Eq. 1.33 can be rewritten as:

$$
\phi^-_{xx}(x_j, y_k) = \frac{\left(\phi^+_{j+1,k} - C(x_{j+1}, \alpha)\right) - 2\phi^-_{j,k} + \phi^-_{j-1,k}}{(\Delta x)^2},
$$

(1.35)

where

$$
C(x_{j+1}, \alpha) = [\phi](\alpha, y_k) + (x_{j+1} - \alpha)[\phi_x](\alpha, y_k) + \frac{(x_{j+1} - \alpha)^2}{2}[\phi_{xx}](\alpha, y_k).
$$

(1.36)

Similarly, the approximation for $\phi^-_{yy}(x_j, y_k)$ can be computed as:

$$
\phi^-_{yy}(x_j, y_k) = \frac{\left(\phi^+_{j,k+1} - C(\beta, y_{k+1})\right) - 2\phi^-_{j,k} + \phi^-_{j,k-1}}{(\Delta y)^2},
$$

(1.37)

where

$$
C(\beta, y_{k+1}) = [\phi](x_j, \beta) + (y_{k+1} - \beta)[\phi_y](x_j, \beta) + \frac{(y_{k+1} - \beta)^2}{2}[\phi_{yy}](x_j, \beta).
$$

(1.38)

The numerical scheme for the domain interface problem Eq. 1.30 at an irregular grid point

(x_j, y_k) can be written as:

$$\frac{\phi^+_{j+1,k} - 2\phi^-_{j,k} + \phi^-_{j-1,k}}{(\Delta x)^2} + \frac{\phi^+_{j,k+1} - 2\phi^-_{j,k} + \phi^-_{j,k-1}}{(\Delta y)^2} = f_{j,k} + C_{j,k}, \tag{1.39}$$

where the correction term is:

$$C_{j,k} = \frac{C(x_{j+1}, \alpha)}{(\Delta x)^2} + \frac{C(\beta, y_{k+1})}{(\Delta y)^2}. \tag{1.40}$$

Combining Eq. 1.32 and Eq. 1.39, and using the proper jump conditions, the IIM method for the domain interface problem Eq. 1.30 yields:

$$\frac{\phi_{j+1,k} - 2\phi_{j,k} + \phi_{j-1,k}}{(\Delta x)^2} + \frac{\phi_{j,k+1} - 2\phi_{j,k} + \phi_{j,k-1}}{(\Delta y)^2} = f_{j,k} + C_{j,k}, \tag{1.41}$$

where

$$f_{j,k} = \begin{cases} f(x_j, y_k), & (x_j, y_k) \in \Omega, \\ 0, & (x_j, y_k) \in \bar{\Omega} \backslash \Omega, \end{cases} \tag{1.42}$$

and $C_{j,k}$ is the correction term corresponding to the irregular grid point (x_j, y_k), while for regular grid point, $C_{j,k} = 0$.

The approximation Eq. 1.41 is defined provided the jump conditions Eq. 1.31 are known. However, in our case, the proper jump conditions should be determined numerically according to the boundary condition Eq. 1.28 using the augmented technique (see, e.g., (88; 90; 91)). To this end, we assume that the jump conditions are $[\phi] = 0$ and $[\phi_\mathbf{n}] = q(x, y)$ on $\partial\Omega$, and define the augmented variable at selected control points (usually the orthogonal projections of all the irregular grid points on the interface $\partial\Omega$ or the intersections of the

interface $\partial\Omega$ and the mesh), $\mathbf{X} = [\mathbf{X}_1, \mathbf{X}_2, \cdots, \mathbf{X}_m]^T$:

$$\mathbf{Q} = [q_1, q_2, \cdots, q_m], \tag{1.43}$$

where $q_i = [\phi_\mathbf{n}](\mathbf{X}_i) = q(\mathbf{X}_i)$ is the discrete value of the jump condition $[\phi_\mathbf{n}]$ at control point $\mathbf{X}_i$. This augmented variable $\mathbf{Q}$ becomes a part of the solution for the interface problem Eq. 1.30, and should be calculated numerically. To do so, we can observe that the correction terms $C_{j,k}$'s in Eq. 1.41 are linear combinations of the jump conditions, so we can write Eq. 1.41 in the matrix form:

$$A\Phi + B\mathbf{Q} = F, \tag{1.44}$$

where A and B are sparse matrices, Φ is a vector whose components are $\phi_{j,k}$, the approximate solution to the interfaced domain problem Eq. 1.30 and F is a vector consist of $f_{j,k}$, the discrete values of the source term.

On the other hand, we can interpolate Φ and obtain $\phi^-(\mathbf{X})$, which provide an approximation to the boundary condition Eq. 1.28 as limit values of $\phi(\mathbf{X})$ from Ω^- side. The interpolation scheme depends on Φ and $\mathbf{Q}$ linearly, so we can write

$$\phi(\mathbf{X}) = C\Phi + D\mathbf{Q} = g(\mathbf{X}), \tag{1.45}$$

where C and D are two sparse matrices. Combining Eq. 1.44 and Eq. 1.45, we obtain the following system of equations:

$$\begin{bmatrix} A & B \\ C & D \end{bmatrix} \begin{bmatrix} \Phi \\ \mathbf{Q} \end{bmatrix} = \begin{bmatrix} F \\ g(\mathbf{X}) \end{bmatrix}. \tag{1.46}$$

Then the solution Φ of the linear system Eq. 1.46 gives us a discrete approximation of the

22

exact solution $\phi(x, y)$ which satisfy the equation Eq. 1.27 in the domain Ω and the Dirichlet boundary condtition Eq. 1.28 on $\partial\Omega$.

Next, we eliminate Φ from Eq. 1.46 and solve the resulted linear system for $\mathbf{Q}$:

$$(D - CA^{-1}B)\mathbf{Q} = g(\mathbf{X}) - CA^{-1}F. \tag{1.47}$$

To do so, we define the residual of the boundary condition Eq. 1.28 corresponding to the augmented variable $\mathbf{Q}$ as:

$$R(\mathbf{Q}) := R(\Phi(\mathbf{Q})) = C\Phi + D\mathbf{Q} - g(\mathbf{X}). \tag{1.48}$$

If we set the augmented variable $\mathbf{Q} = 0$, the equation Eq. 1.44 yields

$$\Phi(0) = A^{-1}F, \tag{1.49}$$

and the right hand side of the Schur-complement equation Eq. 1.47 can be computed as:

$$\begin{aligned}
g(\mathbf{X}) - CA^{-1}F &= g(\mathbf{X}) - CA^{-1}F \\
&= g(\mathbf{X}) - C\Phi(0) \\
&= g(\mathbf{X}) - (C\Phi(0) + D0) = -R(0).
\end{aligned} \tag{1.50}$$

For arbitrary augmented variable $\mathbf{Q}$, we can easily compute the left hand side matrix-vector

multiplication of Eq. 1.46 as follows:

$$
\begin{aligned}
(D - CA^{-1}B)\mathbf{Q} = D\mathbf{Q} &- CA^{-1}B\mathbf{Q} \\
&= D\mathbf{Q} - CA^{-1}(F - A\Phi(\mathbf{Q})) \\
&= D\mathbf{Q} - C\Phi(0) + C\Phi(\mathbf{Q}) \\
&= (D\mathbf{Q} + C\Phi(\mathbf{Q}) - g(\mathbf{X})) - (D0 + C\Phi(0) - g(\mathbf{X})) \\
&= R(\mathbf{Q}) - R(0).
\end{aligned}
\tag{1.51}
$$

Thus, Eq. 1.51 gives us a way to compute the matrix-vector multiplication of the Schur-complement equation Eq. 1.47, so we can solve it for the augmented variable $\mathbf{Q}$ by GMRES method which only requires to compute the matrix-vector multiplication to solve a linear system. We can also easily construct the Schur-complement matrix $D - CA^{-1}B$ by setting the augmented variable $\mathbf{Q}$ as zero and unit vectors $e_1, e_2, \cdots, e_m$ and calculate the corresponding residual $R(0)$ and $R(e_i)$ for $i = 1, 2, \cdots, m$, then difference of the residuals $R(e_i) - R(0)$ gives us the i-th column of the Schur-complement matrix. Once we constructed the matrix, we can apply any linear solver to solve for the suitable augmented variable $\mathbf{Q}$. Once the augmented variable $\mathbf{Q}$ is obtained, we can apply the IIM scheme, and plug it back into Eq. 1.44 to solve for ϕ.

1.5   Particle method

In the past several decades, particle methods have been applied to solve a broad class of problems arising in fluid dynamics, solid state physics, medical physics and astrophysics (see, e.g., (25; 27; 45; 55; 101; 61)). In these methods, the numerical solution is sought as a linear combination of Dirac delta-functions whose positions and coefficients represent

the locations and weight of the particles. The locations and weights of particles are first chosen to approximate the initial data and then evolved in time according to the system of ODEs obtained from a weak formulation of the problem. The point values of the computed solution at time $t > 0$ are obtained by regularizing the particle solution.

Particle methods are most naturally applied to solve transport equations, but over the years, these methods have beed extended to a larger class of equations that include dispersion, diffusion and other nonlinear terms. In particular, we are interested in the application of the particle methods for convection-diffusion equations. As an example, we consider the following two-dimensional convection-diffusion equation:

$$u(x, y, t)_t + \left(f(x, y, t)u\right)_x + \left(g(x, y, t)u\right) = \nu \Delta u, \quad \nu > 0, \ (x, y) \in \Omega \subset \mathbb{R}^2, \ t \geq 0, \quad (1.52)$$

subject to the initial condition:

$$u_0(x, y) = u(x, y, 0), \quad (1.53)$$

where u is an unknown function, the velocities $f(x, y, t)$, $g(x, y, t)$ and the diffusion coefficient ν are given. The particle solution is a linear combination of Dirac delta-functions,

$$u^N(x, y, t) = \sum_{i=1}^{N} w_i(t)\delta(x - x_i(t), y - y_i(t)), \quad (1.54)$$

for some set $(x_i(t), y_i(t), w_i(t))$ of points $(x_i(t), y_i(t))$ and coefficients $w_i(t)$, where N is the total number of particles, $w_i(t)$ is particle weight representing the amount of the quantity u carried by the ith partitcle and $(x_i(t), y_i(t))$ is location of the ith particle. As mentioned above, in order to apply the particle methods, the location (x_i, y_i) and weight w_i need to be

properly chosen to approximate the initial condition Eq. 1.53 at time $t = 0$:

$$u_0^N(x, y) = \sum_{i=1}^{N} w_i(0)\delta(x - x_i(0), y - y_i(0)). \tag{1.55}$$

There are many ways to determine these coefficients $w_i(0)$ and initial locations $(x_i(0), y_i(0))$, and we do this by following the steps introduced in (20). First of all, we divide the computational domain Ω into N non-overlapping subdomains Ω_i:

$$\bigcup_{i=1}^{N} \Omega_i = \Omega, \quad \Omega_i \bigcap \Omega_j = \emptyset, \ \forall i \neq j. \tag{1.56}$$

The location of the ith particle, $(x_i(0), y_i(0))$ is set to be at the center of mass of Ω_i and the initial weight is the entire mass of $u_0(x, y)$ in Ω_i, which leads to the following formula for $w_i(0)$:

$$w_i(0) = \int_{\Omega_i} u_0(x, y)dx\,dy. \tag{1.57}$$

The initial locations and weights of the particles will be evolved in time according to the system of ODEs obtained by considering a weak formulation of the problem Eq. 1.52. The ODE system corresponding to the convection-diffusion equation Eq. 1.52, reads (see, e.g., (20)) as follow:

$$\begin{aligned}
\frac{d x_i(t)}{d t} &= f(x_i(t), y_i(t), t), \\
\frac{d y_i(t)}{d t} &= g(x_i(t), y_i(t), t), \\
\frac{d w_i(t)}{d t} &= \beta_i(t), \\
\frac{d}{d t}|\Omega_i(t)| &= \big(f_x(x_i(t), y_i(t), t) + g_y(x_i(t), y_i(t), t)\big)|\Omega_i(t)|,
\end{aligned} \tag{1.58}$$

where

$$\beta_i = \frac{\nu}{\sigma^2} \sum_{j=1}^{N} \eta_\sigma(x_i(t) - x_j(t), y_i(t) - y_j(t)) \{w_j(t)|\Omega_i(t)| - w_i(t)|\Omega_j(t)|\},$$

$$\eta_\sigma(x, y) = \frac{1}{\sigma^2} \eta(\frac{x}{\sigma}, \frac{y}{\sigma}). \tag{1.59}$$

Here $\eta \in L^1(\mathbb{R}^2)$ is an even function, and σ is a characteristic length. Once the particle solution Eq. 1.54 has be obtained, we need to recover the point values of the computed solution from its particle distribution. There are many different ways to perform such a regularization. One of the most widely used methods is based on taking a convolution product with a mollification kernel, $\varsigma_\epsilon(x, y)$, satisfying the following properties

$$\varsigma_\epsilon(x, y) = \frac{1}{\epsilon^2} \varsigma(\frac{x}{\epsilon}, \frac{y}{\epsilon}) \text{ and } \int_{\mathbb{R}^2} \varsigma(x, y) dx dy = 1, \tag{1.60}$$

where ϵ is a characteristic length of the kernel $\varsigma_\epsilon(x, y)$ (see, e.g., (115)). Then the regularized solution can be defined as

$$u(x, y, t) := \sum_{i=1}^{N} w_i(t) \varsigma_\epsilon(x - x_i(t), y - y_i(t)). \tag{1.61}$$

There are many different kinds of mollification kernel like Gaussian, generalized Gaussian and compactly supported mollifiers have been derived in the past decades, and there is a lot of discussion in the literature on the selection of a mollification kernel (see, e.g., (2; 6; 7; 8; 26; 29; 33; 34; 35; 54; 102; 106; 114; 115)). And particularly, in our investigation, we applied the inverse distance weighting interpolation to recover the point values of the computed solution from the particle solution (see, e.g., (129; 99)).

CHAPTER

2

HIGH-ORDER POSITIVITY-PRESERVING HYBRID FINITE-VOLUME-FINITE-DIFFERENCE METHODS FOR CHEMOTAXIS SYSTEMS

In this chapter, we develop and study hybrid finite-volume-finite-difference (FVFD) schemes for the Patlak-Keller-Segel chemotaxis system Eq. 1.1 and related models. Our FVFD method

solve the bacteria density equation in Eq. 1.1 using a (high-order) positivity-preserving finite-volume method, while a much simpler chemoattractant concentration equation is solved by a simple (high-order) centered-difference scheme. The new schemes are highly accurate, computationally efficient and robust.

This chapter is organized as follows. First, in §2.1.1 we design a second-order positivity-preserving hybrid FVFD scheme for the PKS system Eq. 1.1. In §2.1.2, we develop a fourth-order positivity-preserving hybrid FVFD method. Finally, in §2.2 we illustrate the performance of the proposed schemes in several numerical experiments. To conduct the experiments in §2.2 we extend the developed methods to the two-species chemotaxis system Eq. 1.7 that was originally proposed and analytically studied in (31; 41; 42; 43; 44; 46; 83; 130).

2.1   Hybrid Finite-Volume-Finite-Difference Schemes

To derive high-order positivity-preserving numerical schemes for the chemotaxis system Eq. 1.1, we first rewrite it in the following equivalent form:

$$\begin{cases} \rho_t + (\chi\rho u - \rho_x)_x + (\chi\rho v - \rho_y)_y = 0, \\ \alpha c_t = \Delta c - \gamma_c c + \gamma_\rho \rho, \end{cases} \quad u := c_x, \ v := c_y, \tag{2.1}$$

where u and v are the chemotactic velocities.

We consider the system Eq. 2.1 in a square domain $\Omega \subset \mathbb{R}^2$, where we introduce a Cartesian mesh consisting of the cells $I_{j,k} := [x_{j-\frac{1}{2}}, x_{j+\frac{1}{2}}] \times [y_{k-\frac{1}{2}}, y_{k+\frac{1}{2}}]$, which, for the sake of simplicity, are assumed to be of the uniform size $\Delta x \Delta y$, that is, $x_{j+\frac{1}{2}} - x_{j-\frac{1}{2}} \equiv \Delta x$ for all j and $y_{k+\frac{1}{2}} - y_{k-\frac{1}{2}} \equiv \Delta y$ for all k. On this mesh, a general semi-discrete hybrid FVFD scheme

for the PKS system Eq. 2.1 will have the following form:

$$
\begin{cases}
\dfrac{d\overline{\rho}_{j,k}}{dt} = -\dfrac{\mathscr{F}_{j+\frac{1}{2},k} - \mathscr{F}_{j-\frac{1}{2},k}}{\Delta x} - \dfrac{\mathscr{G}_{j,k+\frac{1}{2}} - \mathscr{G}_{j,k-\frac{1}{2}}}{\Delta y}, \\
\alpha \dfrac{dc_{j,k}}{dt} = \Delta_{j,k} c - \gamma_c c_{j,k} + \gamma_\rho \rho_{j,k}.
\end{cases}
\tag{2.2}
$$

Here, the cell averages of the density, $\overline{\rho}_{j,k}(t) \approx \frac{1}{\Delta x \Delta y} \iint_{I_{j,k}} \rho(x,y,t)\,dx\,dy$, and the point values of the chemoattractant concentration, $c_{j,k}(t) \approx c(x_j, y_k, t)$, are the evolved quantities, $\mathscr{F}_{j+\frac{1}{2},k}$ and $\mathscr{G}_{j,k+\frac{1}{2}}$ are the numerical fluxes in the x- and y-directions, respectively, $\Delta_{j,k}$ is a discrete Laplacian, and $\rho_{j,k}(t) \approx \rho(x_j, y_k, t)$ are the approximate point values of the density.

In what follows, we construct the second- (§2.1.1) and fourth-order (§2.1.2) hybrid FVFD schemes. In order to distinguish between the second- and fourth-order numerical fluxes and discrete Laplacians, we will denote them by $\mathscr{F}^{\mathrm{II}}_{j+\frac{1}{2},k}, \mathscr{G}^{\mathrm{II}}_{j,k+\frac{1}{2}}, \Delta^{\mathrm{II}}_{j,k}$ and $\mathscr{F}^{\mathrm{IV}}_{j+\frac{1}{2},k}, \mathscr{G}^{\mathrm{IV}}_{j,k+\frac{1}{2}}, \Delta^{\mathrm{IV}}_{j,k}$, respectively.

2.1.1   Derivation of the Second-Order Scheme

In this section, we present a detailed derivation of the second-order hybrid FVFD scheme of the form Eq. 2.2.

We first write the second-order numerical fluxes in Eq. 2.2 as follows:

$$
\mathscr{F}^{\mathrm{II}}_{j+\frac{1}{2},k} = \chi \rho^{\mathrm{II}}_{j+\frac{1}{2},k} u^{\mathrm{II}}_{j+\frac{1}{2},k} - (\rho_x)^{\mathrm{II}}_{j+\frac{1}{2},k}, \quad \mathscr{G}^{\mathrm{II}}_{j,k+\frac{1}{2}} = \chi \rho^{\mathrm{II}}_{j,k+\frac{1}{2}} v^{\mathrm{II}}_{j,k+\frac{1}{2}} - (\rho_y)^{\mathrm{II}}_{j,k+\frac{1}{2}}.
\tag{2.3}
$$

The cell density derivatives, $(\rho_x)^{\mathrm{II}}_{j+\frac{1}{2},k}$ and $(\rho_y)^{\mathrm{II}}_{j,k+\frac{1}{2}}$, and velocities, $u^{\mathrm{II}}_{j+\frac{1}{2},k}$ and $v^{\mathrm{II}}_{j,k+\frac{1}{2}}$, are

approximated using the central differences:

$$(\rho_x)^{\text{II}}_{j+\frac{1}{2},k} = \frac{\overline{\rho}_{j+1,k} - \overline{\rho}_{j,k}}{\Delta x}, \quad (\rho_y)^{\text{II}}_{j,k+\frac{1}{2}} = \frac{\overline{\rho}_{j,k+1} - \overline{\rho}_{j,k}}{\Delta y},$$
$$u^{\text{II}}_{j+\frac{1}{2},k} = \frac{c_{j+1,k} - c_{j,k}}{\Delta x}, \qquad v^{\text{II}}_{j,k+\frac{1}{2}} = \frac{c_{j,k+1} - c_{j,k}}{\Delta y}, \tag{2.4}$$

while the point values $\rho^{\text{II}}_{j+\frac{1}{2},k}$ and $\rho^{\text{II}}_{j,k+\frac{1}{2}}$ are computed in an upwind manner:

$$\rho^{\text{II}}_{j+\frac{1}{2},k} = \begin{cases} \rho^{\text{E}}_{j,k}, & \text{if } u^{\text{II}}_{j+\frac{1}{2},k} > 0, \\ \rho^{\text{W}}_{j+1,k}, & \text{otherwise,} \end{cases} \qquad \rho^{\text{II}}_{j,k+\frac{1}{2}} = \begin{cases} \rho^{\text{N}}_{j,k}, & \text{if } v^{\text{II}}_{j,k+\frac{1}{2}} > 0, \\ \rho^{\text{S}}_{j,k+1}, & \text{otherwise.} \end{cases} \tag{2.5}$$

In Eq. 2.5, the one-sided point values at the interfaces, $\rho^{\text{E}}_{j,k}$, $\rho^{\text{W}}_{j+1,k}$, $\rho^{\text{N}}_{j,k}$ and $\rho^{\text{S}}_{j,k+1}$, are calculated using a second-order piecewise linear reconstruction

$$\widetilde{\rho}(x,y) = \overline{\rho}_{j,k} + (\rho_x)_{j,k}(x - x_j) + (\rho_y)_{j,k}(y - y_k), \quad (x,y) \in I_{j,k} \tag{2.6}$$

as follows:

$$\rho^{\text{E}}_{j,k} = \widetilde{\rho}(x_{j+\frac{1}{2}} - 0, y_k) = \overline{\rho}_{j,k} + \frac{\Delta x}{2}(\rho_x)_{j,k},$$
$$\rho^{\text{W}}_{j+1,k} = \widetilde{\rho}(x_{j+\frac{1}{2}} + 0, y_k) = \overline{\rho}_{j+1,k} - \frac{\Delta x}{2}(\rho_x)_{j+1,k},$$
$$\rho^{\text{N}}_{j,k} = \widetilde{\rho}(x_j, y_{k+\frac{1}{2}} - 0) = \overline{\rho}_{j,k} + \frac{\Delta y}{2}(\rho_y)_{j,k},$$
$$\rho^{\text{S}}_{j,k+1} = \widetilde{\rho}(x_j, y_{k+\frac{1}{2}} + 0) = \overline{\rho}_{j,k+1} - \frac{\Delta y}{2}(\rho_y)_{j,k+1}. \tag{2.7}$$

In order to ensure that the point values in Eq. 2.7 are both second-order and nonnegative,

the slopes in Eq. 2.6 are calculated adaptively using

$$
(\rho_x)_{j,k} = \begin{cases} \dfrac{\overline{\rho}_{j+1,k} - \overline{\rho}_{j-1,k}}{2\Delta x}, & \text{if } \overline{\rho}_{j,k} \pm \dfrac{\Delta x}{2} \cdot \dfrac{\overline{\rho}_{j+1,k} - \overline{\rho}_{j-1,k}}{2\Delta x} = \overline{\rho}_{j,k} \pm \dfrac{\overline{\rho}_{j+1,k} - \overline{\rho}_{j-1,k}}{4} \geq 0, \\[3mm] \text{minmod}\Big(2\dfrac{\overline{\rho}_{j+1,k} - \overline{\rho}_{j,k}}{\Delta x}, \dfrac{\overline{\rho}_{j+1,k} - \overline{\rho}_{j-1,k}}{2\Delta x}, 2\dfrac{\overline{\rho}_{j,k} - \overline{\rho}_{j-1,k}}{\Delta x}\Big), & \text{otherwise,} \end{cases}
$$

$$
(\rho_y)_{j,k} = \begin{cases} \dfrac{\overline{\rho}_{j,k+1} - \overline{\rho}_{j,k-1}}{2\Delta y}, & \text{if } \overline{\rho}_{j,k} \pm \dfrac{\Delta y}{2} \cdot \dfrac{\overline{\rho}_{j,k+1} - \overline{\rho}_{j,k-1}}{2\Delta y} = \overline{\rho}_{j,k} \pm \dfrac{\overline{\rho}_{j,k+1} - \overline{\rho}_{j,k-1}}{4} \geq 0, \\[3mm] \text{minmod}\Big(2\dfrac{\overline{\rho}_{j,k+1} - \overline{\rho}_{j,k}}{\Delta y}, \dfrac{\overline{\rho}_{j,k+1} - \overline{\rho}_{j,k-1}}{2\Delta y}, 2\dfrac{\overline{\rho}_{j,k} - \overline{\rho}_{j,k-1}}{\Delta y}\Big), & \text{otherwise.} \end{cases}
$$

(2.8)

Here,

$$
\text{minmod}(z_1, z_2, \ldots) := \begin{cases} \min(z_1, z_2, \ldots), & \text{if } z_i > 0 \ \forall i, \\[2mm] \max(z_1, z_2, \ldots), & \text{if } z_i < 0 \ \forall i, \\[2mm] 0, & \text{otherwise,} \end{cases}
$$

and the positivity of reconstructed point values is ensured by the positivity-preserving generalized minmod limiter, (94; 105; 120; 126), under the assumption that the cell averages of ρ are nonnegative.

Remark 2.1.1 We note that the minmod limiter used in Eq. 2.8 can be replaced with another (positivity-preserving) nonlinear limiter; see, e.g., (94; 105; 120; 126).

Next, we use the standard five-point stencil to obtain a second-order approximate Laplace operator in Eq. 2.2:

$$
\Delta_{j,k}^{\text{II}} c = \frac{c_{j+1,k} - 2c_{j,k} + c_{j-1,k}}{(\Delta x)^2} + \frac{c_{j,k+1} - 2c_{j,k} + c_{j,k-1}}{(\Delta y)^2}.
$$

(2.9)

This completes the derivation and the resulting second-order semi-discrete hybrid

FVFD scheme is

$$
\begin{cases}
\dfrac{d\overline{\rho}_{j,k}}{dt} = -\dfrac{\mathscr{F}^{\mathrm{II}}_{j+\frac{1}{2},k} - \mathscr{F}^{\mathrm{II}}_{j-\frac{1}{2},k}}{\Delta x} - \dfrac{\mathscr{G}^{\mathrm{II}}_{j,k+\frac{1}{2}} - \mathscr{G}^{\mathrm{II}}_{j,k-\frac{1}{2}}}{\Delta y}, \\[4mm]
\alpha \dfrac{dc_{j,k}}{dt} = \Delta^{\mathrm{II}}_{j,k} c - \gamma_c c_{j,k} + \gamma_\rho \overline{\rho}_{j,k}.
\end{cases}
\tag{2.10}
$$

We now consider the cases $\alpha = 1$ and $\alpha = 0$ separately.

Parabolic-Parabolic Case ($\alpha = 1$). In this case, the obtained scheme Eq. 2.10 is a system of time-dependent ODEs, which has to be numerically integrated using a stable and accurate ODE solver. In our numerical experiments, we use strong stability preserving Runge-Kutta methods (SSP RK); see, e.g., (52; 53). The SSP property is essential for the resulting fully discrete scheme to preserve positivity of both $\{\overline{\rho}_{j,k}\}$ and $\{c_{j,k}\}$ as stated in the following theorem. We prove this result for the first-order forward Euler discretization, but it is also valid for the SSP methods, whose time steps are convex combinations of several forward Euler steps.

Theorem 2.1.1 *Assume that the system of ODEs Eq. 2.10 with $\alpha = 1$, Eq. 2.3–Eq. 2.9 is integrated using the forward Euler method:*

$$
\overline{\rho}_{j,k}(t+\Delta t) = \overline{\rho}_{j,k}(t) - \lambda\big(\mathscr{F}^{\mathrm{II}}_{j+\frac{1}{2},k}(t) - \mathscr{F}^{\mathrm{II}}_{j-\frac{1}{2},k}(t)\big) - \mu\big(\mathscr{G}^{\mathrm{II}}_{j,k+\frac{1}{2}}(t) - \mathscr{G}^{\mathrm{II}}_{j,k-\frac{1}{2}}(t)\big),
\tag{2.11}
$$

$$
c_{j,k}(t+\Delta t) = (1 - \Delta t \gamma_c) c_{j,k}(t) + \Delta t \Delta^{\mathrm{II}}_{j,k} c(t) + \Delta t \gamma_\rho \overline{\rho}_{j,k}(t),
\tag{2.12}
$$

where $\lambda := \Delta t / \Delta x$ and $\mu := \Delta t / \Delta y$. Then, the evolved cell densities, $\overline{\rho}_{j,k}(t + \Delta t)$, and chemoattractant concentrations, $c_{j,k}(t + \Delta t)$, will be nonnegative for all j, k provided $\overline{\rho}_{j,k}(t)$ and $c_{j,k}(t)$ are nonnegative for all j, k and the following CFL-like condition is satisfied:

$$
\Delta t \le \min\left\{ \frac{\Delta x}{8a}, \frac{\Delta y}{8b}, \frac{\Delta x \Delta y}{4K}, \frac{1}{\max\{K_1, \varepsilon\}} \right\},
\tag{2.13}
$$

where

$$a := \chi \max_{j,k} |u^{\mathrm{II}}_{j+\frac{1}{2},k}|, \quad b := \chi \max_{j,k} |v^{\mathrm{II}}_{j,k+\frac{1}{2}}|,$$

$$K := \frac{\Delta x}{\Delta y} + \frac{\Delta y}{\Delta x}, \quad K_1 := \max_{j,k}\left(\gamma_c + \frac{2K}{\Delta x \Delta y} - \frac{\gamma_\rho \overline{\rho}_{j,k}}{c_{j,k}}\right). \tag{2.14}$$

Proof: We follow the lines of the positivity proof in (22). We begin with the cell density equation Eq. 2.11 and note that the positivity-preserving property of the interpolant Eq. 2.6 will guarantee that the reconstructed point values $\rho^{\mathrm{E}}_{j,k}, \rho^{\mathrm{W}}_{j,k}, \rho^{\mathrm{N}}_{j,k}$ and $\rho^{\mathrm{S}}_{j,k}$ will be nonnegative provided $\overline{\rho}_{j,k}(t) \geq 0, \ \forall j, k$. We then use Eq. 2.3–Eq. 2.5 and the conservation property for the cell densities, $\overline{\rho}_{j,k} = \frac{1}{8}(\rho^{\mathrm{E}}_{j,k} + \rho^{\mathrm{W}}_{j,k} + \rho^{\mathrm{S}}_{j,k} + \rho^{\mathrm{N}}_{j,k}) + \frac{1}{2}\overline{\rho}_{j,k}$, to regroup the terms in Eq. 2.11 as follows:

$$
\begin{aligned}
\overline{\rho}_{j,k}(t + \Delta t) = & \left[\frac{1}{8} - \frac{\lambda\chi}{2}\left(|u^{\mathrm{II}}_{j-\frac{1}{2},k}| - u^{\mathrm{II}}_{j-\frac{1}{2},k}\right)\right]\rho^{\mathrm{W}}_{j,k} + \left[\frac{1}{8} - \frac{\lambda\chi}{2}\left(|u^{\mathrm{II}}_{j+\frac{1}{2},k}| + u^{\mathrm{II}}_{j+\frac{1}{2},k}\right)\right]\rho^{\mathrm{E}}_{j,k} \\
& + \frac{\lambda\chi}{2}\left(|u^{\mathrm{II}}_{j+\frac{1}{2},k}| - u^{\mathrm{II}}_{j+\frac{1}{2},k}\right)\rho^{\mathrm{W}}_{j+1,k} + \frac{\lambda\chi}{2}\left(|u^{\mathrm{II}}_{j-\frac{1}{2},k}| + u^{\mathrm{II}}_{j-\frac{1}{2},k}\right)\rho^{\mathrm{E}}_{j-1,k} \\
& + \left[\frac{1}{8} - \frac{\mu\chi}{2}\left(|v^{\mathrm{II}}_{j,k-\frac{1}{2}}| - v^{\mathrm{II}}_{j,k-\frac{1}{2}}\right)\right]\rho^{\mathrm{S}}_{j,k} + \left[\frac{1}{8} - \frac{\mu\chi}{2}\left(|v^{\mathrm{II}}_{j,k+\frac{1}{2}}| + v^{\mathrm{II}}_{j,k+\frac{1}{2}}\right)\right]\rho^{\mathrm{N}}_{j,k} \\
& + \frac{\mu\chi}{2}\left(|v^{\mathrm{II}}_{j,k+\frac{1}{2}}| - v^{\mathrm{II}}_{j,k+\frac{1}{2}}\right)\rho^{\mathrm{S}}_{j,k+1} + \frac{\mu\chi}{2}\left(|v^{\mathrm{II}}_{j,k-\frac{1}{2}}| + v^{\mathrm{II}}_{j,k-\frac{1}{2}}\right)\rho^{\mathrm{N}}_{j,k-1} \\
& + \overline{\rho}_{j,k}(t)\left[\frac{1}{2} - \frac{2K\Delta t}{\Delta x \Delta y}\right] + \Delta t\left[\frac{\overline{\rho}_{j+1,k}(t) + \overline{\rho}_{j-1,k}(t)}{(\Delta x)^2} + \frac{\overline{\rho}_{j,k+1}(t) + \overline{\rho}_{j,k-1}(t)}{(\Delta y)^2}\right].
\end{aligned}
$$

As one can see, $\overline{\rho}_{j,k}(t + \Delta t)$ is a linear combination of the cell averages $\overline{\rho}_{j,k}(t), \overline{\rho}_{j\pm1,k}(t),$ $\overline{\rho}_{j,k\pm1}(t)$ and the reconstructed point values $\rho^{\mathrm{W}}_{j,k}, \rho^{\mathrm{E}}_{j,k}, \rho^{\mathrm{W}}_{j+1,k}, \rho^{\mathrm{E}}_{j-1,k}, \rho^{\mathrm{S}}_{j,k}, \rho^{\mathrm{N}}_{j,k}, \rho^{\mathrm{S}}_{j,k+1}, \rho^{\mathrm{N}}_{j,k-1},$ which are nonnegative. The coefficients of this linear combination are also nonnegative under the CFL-like condition Eq. 2.13, which guarantees that $\overline{\rho}_{j,k}(t + \Delta t) \geq 0$ for all j, k.

Finally, the CFL-like condition Eq. 2.13 ensures that all of the terms on the right-hand side (RHS) of Eq. 2.12 are nonnegative and thus $c_{j,k}(t + \Delta t) \geq 0$ for all j, k, which completes the proof of the theorem. $\qquad\square$

Parabolic-Elliptic Case ($\alpha = 0$). In this case, the scheme Eq. 2.10 is a system of differential-algebraic equations (DAEs). The second equation in Eq. 2.10 now reduces to a system of linear algebraic equations for $c_{j,k}$, which is to be solved by an accurate and efficient linear algebric solver. It should be observed that the matrix of this linear system is diagonally dominant, which would guarantee the positivity of c, while the positivity of ρ is enforced the same way as in the parabolic-parabolic case, but with a different CFL-like condition as summarized in the following theorem.

Theorem 2.1.2 *Assume that the first equation of the system of DAEs Eq. 2.10 with $\alpha = 0$, Eq. 2.3–Eq. 2.9 is integrated using the forward Euler method resulting in equation Eq. 2.11, while the system of linear algebraic equations for $c_{j,k}$ is solved exactly. Then, the evolved cell densities, $\overline{\rho}_{j,k}(t + \Delta t)$, and chemoattractant concentrations, $c_{j,k}(t + \Delta t)$, will be nonnegative for all j, k provided $\overline{\rho}_{j,k}(t)$ and $c_{j,k}(t)$ are nonnegative for all j, k and the following CFL-like condition is satisfied:*

$$\Delta t \leq \min\left\{\frac{\Delta x}{8a}, \frac{\Delta y}{8b}, \frac{\Delta x \Delta y}{4K}\right\},$$

where a, b and K are given by Eq. 2.14.

2.1.2 Derivation of the Fourth-Order Scheme

In this section, we present a detailed derivation of the fourth-order hybrid FVFD scheme of the form Eq. 2.2.

We first write the fourth-order numerical fluxes as follows:

$$\mathscr{F}^{\text{IV}}_{j+\frac{1}{2},k} = \chi(\rho u)^{\text{IV}}_{j+\frac{1}{2},k} - (\rho_x)^{\text{IV}}_{j+\frac{1}{2},k}, \quad \mathscr{G}^{\text{IV}}_{j,k+\frac{1}{2}} = \chi(\rho v)^{\text{IV}}_{j,k+\frac{1}{2}} - (\rho_y)^{\text{IV}}_{j,k+\frac{1}{2}}. \tag{2.15}$$

As in the case of the second-order scheme, the cell density derivatives are approximated

using the central differences:

$$
\begin{aligned}
(\rho_x)^{\mathrm{IV}}_{j+\frac{1}{2},k} &= \frac{\overline{\rho}_{j-1,k} - 15\overline{\rho}_{j,k} + 15\overline{\rho}_{j+1,k} - \overline{\rho}_{j+2,k}}{12\Delta x}, \\
(\rho_y)^{\mathrm{IV}}_{j,k+\frac{1}{2}} &= \frac{\overline{\rho}_{j,k-1} - 15\overline{\rho}_{j,k} + 15\overline{\rho}_{j,k+1} - \overline{\rho}_{j,k+2}}{12\Delta y}
\end{aligned}
\tag{2.16}
$$

while the chemotactic flux terms are computed in an upwind manner:

$$
(\rho u)^{\mathrm{IV}}_{j+\frac{1}{2},k} =
\begin{cases}
\rho^{\mathrm{NE}}_{j,k} u_{j+\frac{1}{2},k+\frac{1}{2}} + 4\rho^{\mathrm{E}}_{j,k} u_{j+\frac{1}{2},k} + \rho^{\mathrm{SE}}_{j,k} u_{j+\frac{1}{2},k-\frac{1}{2}}, & \text{if } u_{j+\frac{1}{2},k} > 0, \\
\rho^{\mathrm{NW}}_{j+1,k} u_{j+\frac{1}{2},k+\frac{1}{2}} + 4\rho^{\mathrm{W}}_{j+1,k} u_{j+\frac{1}{2},k} + \rho^{\mathrm{SW}}_{j+1,k} u_{j+\frac{1}{2},k-\frac{1}{2}}, & \text{otherwise,}
\end{cases}
$$

$$
(\rho v)^{\mathrm{IV}}_{j,k+\frac{1}{2}} =
\begin{cases}
\rho^{\mathrm{NW}}_{j,k} v_{j-\frac{1}{2},k+\frac{1}{2}} + 4\rho^{\mathrm{N}}_{j,k} v_{j,k+\frac{1}{2}} + \rho^{\mathrm{NE}}_{j,k} v_{j+\frac{1}{2},k+\frac{1}{2}}, & \text{if } v_{j,k+\frac{1}{2}} > 0, \\
\rho^{\mathrm{SW}}_{j,k+1} v_{j-\frac{1}{2},k+\frac{1}{2}} + 4\rho^{\mathrm{S}}_{j,k+1} v_{j,k+\frac{1}{2}} + \rho^{\mathrm{SE}}_{j,k+1} v_{j+\frac{1}{2},k+\frac{1}{2}}, & \text{otherwise.}
\end{cases}
\tag{2.17}
$$

The velocities u and v in Eq. 2.17 are obtained using the fourth-order central differences:

$$
\begin{aligned}
u_{j+\frac{1}{2},k} &= \frac{c_{j-1,k} - 27c_{j,k} + 27c_{j+1,k} - c_{j+2,k}}{24\Delta x}, \\
v_{j,k+\frac{1}{2}} &= \frac{c_{j,k-1} - 27c_{j,k} + 27c_{j,k+1} - c_{j,k+2}}{24\Delta y},
\end{aligned}
\tag{2.18}
$$

and

$$
\begin{aligned}
u_{j+\frac{1}{2},k+\frac{1}{2}} &= \frac{1}{48\Delta x}\Big[30(c_{j+1,k+1} - c_{j,k+1} + c_{j+1,k} - c_{j,k}) \\
&\quad - 3(c_{j+1,k+2} - c_{j,k+2} + c_{j+1,k-1} - c_{j,k-1}) - (c_{j+2,k+1} - c_{j-1,k+1} + c_{j+2,k} - c_{j-1,k})\Big], \\
v_{j+\frac{1}{2},k+\frac{1}{2}} &= \frac{1}{48\Delta y}\Big[30(c_{j+1,k+1} - c_{j+1,k} + c_{j,k+1} - c_{j,k}) \\
&\quad - 3(c_{j+2,k+1} - c_{j+2,k} + c_{j-1,k+1} - c_{j-1,k}) - (c_{j+1,k+2} - c_{j+1,k-1} + c_{j,k+2} - c_{j,k-1})\Big].
\end{aligned}
\tag{2.19}
$$

The discrete point values of the cell density along the interfaces, $\rho^{\mathrm{E}}_{j,k}$, $\rho^{\mathrm{W}}_{j,k}$, $\rho^{\mathrm{N}}_{j,k}$, $\rho^{\mathrm{S}}_{j,k}$, $\rho^{\mathrm{NE}}_{j,k}$,

$\rho_{j,k}^{\mathrm{NW}}$, $\rho_{j,k}^{\mathrm{SE}}$ and $\rho_{j,k}^{\mathrm{SW}}$, are calculated using a fourth-order piecewise polynomial reconstruction

$$\widetilde{\rho}(x,y) = \sum_{j,k} \mathscr{P}_{j,k}(x,y)\mathbb{1}_{j,k}(x,y) \tag{2.20}$$

as follows:

$$\rho_{j,k}^{\mathrm{E}} = \widetilde{\rho}(x_{j+\frac{1}{2}}-0, y_k), \ \rho_{j,k}^{\mathrm{W}} = \widetilde{\rho}(x_{j-\frac{1}{2}}+0, y_k), \ \rho_{j,k}^{\mathrm{N}} = \widetilde{\rho}(x_j, y_{k+\frac{1}{2}}-0),$$

$$\rho_{j,k}^{\mathrm{S}} = \widetilde{\rho}(x_j, y_{k-\frac{1}{2}}+0), \ \rho_{j,k}^{\mathrm{NE}} = \widetilde{\rho}(x_{j+\frac{1}{2}}-0, y_{k+\frac{1}{2}}-0), \ \rho_{j,k}^{\mathrm{NW}} = \widetilde{\rho}(x_{j-\frac{1}{2}}+0, y_{k+\frac{1}{2}}-0), \tag{2.21}$$

$$\rho_{j,k}^{\mathrm{SE}} = \widetilde{\rho}(x_{j+\frac{1}{2}}-0, y_{k-\frac{1}{2}}+0), \ \rho_{j,k}^{\mathrm{SW}} = \widetilde{\rho}(x_{j-\frac{1}{2}}+0, y_{k-\frac{1}{2}}+0).$$

In Eq. 2.20, $\mathbb{1}_{j,k}(x,y)$ is the characteristic function of cell $I_{j,k}$, and the polynomials $\mathscr{P}_{j,k}(x,y)$ are

$$\begin{aligned}
\mathscr{P}_{j,k}(x,y) = \ &\rho_{j,k} + (\rho_x)_{j,k}(x-x_j) + (\rho_y)_{j,k}(y-y_k) \\
&+ \frac{1}{2}(\rho_{xx})_{j,k}(x-x_j)^2 + (\rho_{xy})_{j,k}(x-x_j)(y-y_k) + \frac{1}{2}(\rho_{yy})_{j,k}(y-y_k)^2 \\
&+ \frac{1}{6}(\rho_{xxx})_{j,k}(x-x_j)^3 + \frac{1}{2}(\rho_{xxy})_{j,k}(x-x_j)^2(y-y_k) \\
&+ \frac{1}{2}(\rho_{xyy})_{j,k}(x-x_j)(y-y_k)^2 + \frac{1}{6}(\rho_{yyy})_{j,k}(y-y_k)^3 \\
&+ \frac{1}{24}(\rho_{xxxx})_{j,k}(x-x_j)^4 + \frac{1}{4}(\rho_{xxyy})_{j,k}(x-x_j)^2(y-y_k)^2 + \frac{1}{24}(\rho_{yyyy})_{j,k}(y-y_k)^4
\end{aligned} \tag{2.22}$$

with the coefficients calculated from the following 13 conservation requirements (see (74) for details including the precise expressions for the reconstructed point values of ρ in terms of its cell averages):

$$\frac{1}{\Delta x \Delta y} \iint\limits_{I_{j+m,k+\ell}} \mathscr{P}_{j,k}(x,y)\,dx\,dy = \overline{\rho}_{j+m,k+\ell}, \quad \{m,\ell \in \mathbb{Z} : |m|+|\ell| \le 2\}. \tag{2.23}$$

Next, we use the nine-point stencil to obtain a fourth-order approximate Laplace oper-

ator,

$$\Delta^{\mathrm{IV}}_{j,k} c = \frac{-c_{j-2,k} + 16c_{j-1,k} - 30c_{j,k} + 16c_{j+1,k} - c_{j+2,k}}{12(\Delta x)^2}$$

$$+ \frac{-c_{j,k-2} + 16c_{j,k-1} - 30c_{j,k} + 16c_{j,k+1} - c_{j,k+2}}{12(\Delta y)^2},$$

which can be rewritten in terms of diffusion fluxes as

$$\Delta^{\mathrm{IV}}_{j,k} c = -\frac{\mathscr{H}^{\mathrm{IV}}_{j+\frac{1}{2},k} - \mathscr{H}^{\mathrm{IV}}_{j-\frac{1}{2},k}}{\Delta x} - \frac{\mathscr{L}^{\mathrm{IV}}_{j,k+\frac{1}{2}} - \mathscr{L}^{\mathrm{IV}}_{j,k-\frac{1}{2}}}{\Delta y} \tag{2.24}$$

with

$$\mathscr{H}^{\mathrm{IV}}_{j+\frac{1}{2},k} = \frac{-c_{j-1,k} + 15c_{j,k} - 15c_{j+1,k} + c_{j+2,k}}{12\Delta x},$$

$$\mathscr{L}^{\mathrm{IV}}_{j,k+\frac{1}{2}} = \frac{-c_{j,k-1} + 15c_{j,k} - 15c_{j,k+1} + c_{j,k+2}}{12\Delta y}. \tag{2.25}$$

The obtained fourth-order semi-discrete hybrid FVFD scheme is

$$\begin{cases} \dfrac{d\overline{\rho}_{j,k}}{dt} = -\dfrac{\mathscr{F}^{\mathrm{IV}}_{j+\frac{1}{2},k} - \mathscr{F}^{\mathrm{IV}}_{j-\frac{1}{2},k}}{\Delta x} - \dfrac{\mathscr{G}^{\mathrm{IV}}_{j,k+\frac{1}{2}} - \mathscr{G}^{\mathrm{IV}}_{j,k-\frac{1}{2}}}{\Delta y}, \\[3mm] \alpha \dfrac{dc_{j,k}}{dt} = -\dfrac{\mathscr{H}^{\mathrm{IV}}_{j+\frac{1}{2},k} - \mathscr{H}^{\mathrm{IV}}_{j-\frac{1}{2},k}}{\Delta x} - \dfrac{\mathscr{L}^{\mathrm{IV}}_{j,k+\frac{1}{2}} - \mathscr{L}^{\mathrm{IV}}_{j,k-\frac{1}{2}}}{\Delta y} - \gamma_c c_{j,k} + \gamma_\rho \rho_{j,k}, \end{cases} \tag{2.26}$$

where $\rho_{j,k}$ is a point value of ρ at the center of cell $I_{j,k}$ given by

$$\rho_{j,k} = \frac{1}{5760}\Big[27\big(\overline{\rho}_{j-2,k} + \overline{\rho}_{j,k-2} + \overline{\rho}_{j,k+2} + \overline{\rho}_{j+2,k}\big) + 10\big(\overline{\rho}_{j-1,k-1} + \overline{\rho}_{j-1,k+1} + \overline{\rho}_{j+1,k-1} + \overline{\rho}_{j+1,k+1}\big)$$

$$- 368\big(\overline{\rho}_{j-1,k} + \overline{\rho}_{j,k-1} + \overline{\rho}_{j,k+1} + \overline{\rho}_{j+1,k}\big) + 7084\overline{\rho}_{j,k}\Big]. \tag{2.27}$$

As in the case of the second-order scheme, we consider the cases $\alpha = 1$ and $\alpha = 0$ separately.

Parabolic-Parabolic Case ($\alpha = 1$). In this case, the obtained scheme Eq. 2.26 is a system of time-dependent ODEs, which, as before, has to be numerically integrated. Unfortunately, even if one uses an SSP ODE solver, positivity of ρ and c cannot be guaranteed. We therefore

modify the numerical fluxes following the approach proposed in (11) in the context of shallow water models.

For simplicity of presentation, we consider the forward Euler time discretization of Eq. 2.26:

$$\overline{\rho}_{j,k}(t+\Delta t) = \overline{\rho}_{j,k}(t) - \lambda\big(\mathscr{F}^{\mathrm{IV}}_{j+\frac{1}{2},k}(t) - \mathscr{F}^{\mathrm{IV}}_{j-\frac{1}{2},k}(t)\big) - \mu\big(\mathscr{G}^{\mathrm{IV}}_{j,k+\frac{1}{2}}(t) - \mathscr{G}^{\mathrm{IV}}_{j,k-\frac{1}{2}}(t)\big),$$

$$c_{j,k}(t+\Delta t) = (1 - \Delta t \gamma_c) c_{j,k}(t) + \Delta t \gamma_\rho \rho_{j,k}(t) \qquad (2.28)$$

$$\qquad - \lambda\big(\mathscr{H}^{\mathrm{IV}}_{j+\frac{1}{2},k}(t) - \mathscr{H}^{\mathrm{IV}}_{j-\frac{1}{2},k}(t)\big) - \mu\big(\mathscr{L}^{\mathrm{IV}}_{j,k+\frac{1}{2}}(t) - \mathscr{L}^{\mathrm{IV}}_{j,k-\frac{1}{2}}(t)\big),$$

where Δt is selected according to the CFL-like condition similar to Eq. 2.13. In order to design a positivity-preserving algorithm, we first introduce "draining" time steps:

$$\Delta t^{\rho}_{j,k} := \frac{\Delta x \Delta y \overline{\rho}_{j,k}(t)}{f^{\rho}_{j,k}\Delta y + g^{\rho}_{j,k}\Delta x} \quad \text{and} \quad \Delta t^{c}_{j,k} := \frac{\Delta x \Delta y [(1 - \Delta t \gamma_c) c_{j,k}(t) + \Delta t \gamma_\rho \rho_{j,k}(t)]}{f^{c}_{j,k}\Delta y + g^{c}_{j,k}\Delta x}, \quad (2.29)$$

where

$$f^{\rho}_{j,k} := \max(\mathscr{F}^{\mathrm{IV}}_{j+\frac{1}{2},k}, 0) + \max(-\mathscr{F}^{\mathrm{IV}}_{j-\frac{1}{2},k}, 0), \qquad g^{\rho}_{j,k} := \max(\mathscr{G}^{\mathrm{IV}}_{j,k+\frac{1}{2}}, 0) + \max(-\mathscr{G}^{\mathrm{IV}}_{j,k-\frac{1}{2}}, 0),$$
$$(2.30)$$
$$f^{c}_{j,k} := \max(\mathscr{H}^{\mathrm{IV}}_{j+\frac{1}{2},k}, 0) + \max(-\mathscr{H}^{\mathrm{IV}}_{j-\frac{1}{2},k}, 0), \quad g^{c}_{j,k} := \max(\mathscr{L}^{\mathrm{IV}}_{j,k+\frac{1}{2}}, 0) + \max(-\mathscr{L}^{\mathrm{IV}}_{j,k-\frac{1}{2}}, 0).$$

We note that one can easily show that under the following time step restriction:

$$\Delta t \leq \min_{j,k}\left\{\min\big(\Delta t^{\rho}_{j,k}, \Delta t^{c}_{j,k}\big)\right\}, \qquad (2.31)$$

the fully discrete scheme Eq. 2.28 is positivity preserving. However, the time step bound Eq. 2.31 is too severe and impractical since it may lead to appearance of very small and decreasing time steps, which will not only make the scheme inefficient, but may simply not allow the code to run through the final computational time.

We therefore follow the idea in (11) and define the following quantities:

$$\begin{aligned}
\Delta t^{\rho}_{j+\frac{1}{2},k} &:= \min(\Delta t, \Delta t^{\rho}_{m,k}), \quad & m &= j + \frac{1}{2} - \frac{\operatorname{sgn}(\mathscr{F}^{\mathrm{IV}}_{j+\frac{1}{2},k})}{2}, \\
\Delta t^{\rho}_{j,k+\frac{1}{2}} &:= \min(\Delta t, \Delta t^{\rho}_{j,\ell}), \quad & \ell &= k + \frac{1}{2} - \frac{\operatorname{sgn}(\mathscr{G}^{\mathrm{IV}}_{j,k+\frac{1}{2}})}{2}, \\
\Delta t^{c}_{j+\frac{1}{2},k} &:= \min(\Delta t, \Delta t^{c}_{p,k}), \quad & p &= j + \frac{1}{2} - \frac{\operatorname{sgn}(\mathscr{H}^{\mathrm{IV}}_{j+\frac{1}{2},k})}{2}, \\
\Delta t^{c}_{j,k+\frac{1}{2}} &:= \min(\Delta t, \Delta t^{c}_{j,q}), \quad & q &= k + \frac{1}{2} - \frac{\operatorname{sgn}(\mathscr{L}^{\mathrm{IV}}_{j,k+\frac{1}{2}})}{2},
\end{aligned} \tag{2.32}$$

and use them to replace the numerical fluxes in Eq. 2.28 with

$$\begin{aligned}
\widehat{\mathscr{F}}^{\mathrm{IV}}_{j+\frac{1}{2},k} &= \frac{\Delta t^{\rho}_{j+\frac{1}{2},k}}{\Delta t} \mathscr{F}^{\mathrm{IV}}_{j+\frac{1}{2},k}, \quad & \widehat{\mathscr{G}}^{\mathrm{IV}}_{j,k+\frac{1}{2}} &= \frac{\Delta t^{\rho}_{j,k+\frac{1}{2}}}{\Delta t} \mathscr{G}^{\mathrm{IV}}_{j,k+\frac{1}{2}} \\
\widehat{\mathscr{H}}^{\mathrm{IV}}_{j+\frac{1}{2},k} &= \frac{\Delta t^{c}_{j+\frac{1}{2},k}}{\Delta t} \mathscr{H}^{\mathrm{IV}}_{j+\frac{1}{2},k}, \quad & \widehat{\mathscr{L}}^{\mathrm{IV}}_{j,k+\frac{1}{2}} &= \frac{\Delta t^{c}_{j,k+\frac{1}{2}}}{\Delta t} \mathscr{L}^{\mathrm{IV}}_{j,k+\frac{1}{2}}.
\end{aligned} \tag{2.33}$$

The modified version of the fully discrete scheme Eq. 2.28 then reads as

$$\overline{\rho}_{j,k}(t+\Delta t) = \overline{\rho}_{j,k}(t) - \lambda\left(\widehat{\mathscr{F}}^{\mathrm{IV}}_{j+\frac{1}{2},k}(t) - \widehat{\mathscr{F}}^{\mathrm{IV}}_{j-\frac{1}{2},k}(t)\right) - \mu\left(\widehat{\mathscr{G}}^{\mathrm{IV}}_{j,k+\frac{1}{2}}(t) - \widehat{\mathscr{G}}^{\mathrm{IV}}_{j,k-\frac{1}{2}}(t)\right), \tag{2.34}$$

$$c_{j,k}(t+\Delta t) = (1 - \Delta t \gamma_c) c_{j,k}(t) + \Delta t \gamma_{\rho} \rho_{j,k}(t)$$

$$\qquad - \lambda\left(\widehat{\mathscr{H}}^{\mathrm{IV}}_{j+\frac{1}{2},k}(t) - \widehat{\mathscr{H}}^{\mathrm{IV}}_{j-\frac{1}{2},k}(t)\right) - \mu\left(\widehat{\mathscr{L}}^{\mathrm{IV}}_{j,k+\frac{1}{2}}(t) - \widehat{\mathscr{L}}^{\mathrm{IV}}_{j,k-\frac{1}{2}}(t)\right). \tag{2.35}$$

We now prove its positivity-preserving property.

Theorem 2.1.3 *The cell densities $\overline{\rho}_{j,k}(t+\Delta t)$ and chemoattractant concentrations $c_{j,k}(t + \Delta t)$, computed by the fully discrete scheme Eq. 2.34, Eq. 2.35, Eq. 2.29, Eq. 2.30, Eq. 2.32, Eq. 2.33, Eq. 2.15–Eq. 2.25 will be nonnegative provided $\overline{\rho}_{j,k}(t)$ and $c_{j,k}(t)$ are nonnegative for all j,k.*

40

Proof: In order to prove positivity of ρ, one needs to consider different cases depending on the sign of the fluxes $\mathscr{F}^{\mathrm{IV}}_{j+\frac{1}{2},k}$ and $\mathscr{G}^{\mathrm{IV}}_{j,k+\frac{1}{2}}$ given by Eq. 2.15. We will only consider one of these cases, namely, assuming that

$$\mathscr{F}^{\mathrm{IV}}_{j+\frac{1}{2},k} > 0, \ \mathscr{F}^{\mathrm{IV}}_{j-\frac{1}{2},k} > 0 \quad \text{and} \quad \mathscr{G}^{\mathrm{IV}}_{j,k+\frac{1}{2}} < 0, \ \mathscr{G}^{\mathrm{IV}}_{j,k-\frac{1}{2}} < 0. \tag{2.36}$$

in the cell $I_{j,k}$. All of the other cases can be analyzed in a similar way.

First, we use the definitions in Eq. 2.30 to obtain

$$f^{\rho}_{j,k} = \mathscr{F}^{\mathrm{IV}}_{j+\frac{1}{2},k}, \quad g^{\rho}_{j,k} = -\mathscr{G}^{\mathrm{IV}}_{j,k-\frac{1}{2}}, \tag{2.37}$$

and then substituting Eq. 2.37 into Eq. 2.29 results in

$$\Delta t^{\rho}_{j,k} = \frac{\Delta x \Delta y \overline{\rho}_{j,k}(t)}{\mathscr{F}^{\mathrm{IV}}_{j+\frac{1}{2},k} \Delta y - \mathscr{G}^{\mathrm{IV}}_{j,k-\frac{1}{2}} \Delta x} > 0. \tag{2.38}$$

It also follows from Eq. 2.36 and Eq. 2.32 that

$$\begin{aligned}
\Delta t^{\rho}_{j+\frac{1}{2},k} &= \min(\Delta t, \Delta t^{\rho}_{j,k}), \quad &\Delta t^{\rho}_{j-\frac{1}{2},k} &= \min(\Delta t, \Delta t^{\rho}_{j-1,k}), \\
\Delta t^{\rho}_{j,k+\frac{1}{2}} &= \min(\Delta t, \Delta t^{\rho}_{j,k+1}), \quad &\Delta t^{\rho}_{j,k-\frac{1}{2}} &= \min(\Delta t, \Delta t^{\rho}_{j,k}).
\end{aligned} \tag{2.39}$$

We now rewrite the cell density equation Eq. 2.34 as

$$\overline{\rho}_{j,k}(t + \Delta t) = \overline{\rho}_{j,k}(t) + \frac{\Delta t^{\rho}_{j-\frac{1}{2},k}}{\Delta x} \mathscr{F}^{\mathrm{IV}}_{j-\frac{1}{2},k} - \frac{\Delta t^{\rho}_{j,k+\frac{1}{2}}}{\Delta y} \mathscr{G}^{\mathrm{IV}}_{j,k+\frac{1}{2}} + \frac{\Delta t^{\rho}_{j,k-\frac{1}{2}}}{\Delta y} \mathscr{G}^{\mathrm{IV}}_{j,k-\frac{1}{2}} - \frac{\Delta t^{\rho}_{j+\frac{1}{2},k}}{\Delta x} \mathscr{F}^{\mathrm{IV}}_{j+\frac{1}{2},k}, \tag{2.40}$$

and show that the RHS of Eq. 2.40 is positive. To this end, we first note that Eq. 2.36 implies

$$\frac{\Delta t^{\rho}_{j-\frac{1}{2},k}}{\Delta x}\, \mathscr{F}^{\mathrm{IV}}_{j-\frac{1}{2},k} - \frac{\Delta t^{\rho}_{j,k+\frac{1}{2}}}{\Delta y}\, \mathscr{G}^{\mathrm{IV}}_{j,k+\frac{1}{2}} > 0. \tag{2.41}$$

We then note that $\Delta t^{\rho}_{j+\frac{1}{2},k} = \Delta t^{\rho}_{j,k-\frac{1}{2}} \le \Delta t^{\rho}_{j,k}$, and therefore using Eq. 2.38, Eq. 2.40 and Eq. 2.41, we conclude with

$$
\begin{aligned}
\overline{\rho}_{j,k}(t+\Delta t) &> \overline{\rho}_{j,k}(t) + \frac{\Delta t^{\rho}_{j,k-\frac{1}{2}}}{\Delta y}\, \mathscr{G}^{\mathrm{IV}}_{j,k-\frac{1}{2}} - \frac{\Delta t^{\rho}_{j+\frac{1}{2},k}}{\Delta x}\, \mathscr{F}^{\mathrm{IV}}_{j+\frac{1}{2},k} \\
&\ge \overline{\rho}_{j,k}(t) + \frac{\Delta x \overline{\rho}_{j,k}(t)}{\mathscr{F}^{\mathrm{IV}}_{j+\frac{1}{2},k}\Delta y - \mathscr{G}^{\mathrm{IV}}_{j,k-\frac{1}{2}}\Delta x}\, \mathscr{G}^{\mathrm{IV}}_{j,k-\frac{1}{2}} - \frac{\Delta y \overline{\rho}_{j,k}(t)}{\mathscr{F}^{\mathrm{IV}}_{j+\frac{1}{2},k}\Delta y - \mathscr{G}^{\mathrm{IV}}_{j,k-\frac{1}{2}}\Delta x}\, \mathscr{F}^{\mathrm{IV}}_{j+\frac{1}{2},k} = 0,
\end{aligned}
$$

which shows that $\overline{\rho}_{j,k}(t+\Delta t) \ge 0$ for all j,k, provided that $\overline{\rho}_{j,k}(\Delta t) \ge 0$ for all j,k.

The positivity proof for the c component of the solution can be obtained similarly, and the proof of the theorem will be completed. □

Remark 2.1.2 We would like to emphasize that unlike Theorem 2.1.1, Theorem 2.1.3 guarantees positivity of ρ and c independently of the CFL condition. However, taking large Δt will affect the stability of the fourth-order scheme. In practice, we have used the same CFL condition Eq. 2.13 when implemented the fourth-order method.

Remark 2.1.3 Note that the positivity-preserving property of the second-order scheme can be also enforced using the "draining" time step technique instead of the adaptive reconstruction approach implemented in §2.1.1.

Parabolic-Elliptic Case ($\alpha = 0$).   In this case, the scheme Eq. 2.26 is a system of DAEs. The second equation in Eq. 2.26 is a system of linear algebraic equations for $c_{j,k}$, which, as before, is to be solved by an accurate and efficient linear algebra solver. However, the matrix

of this linear system is no longer diagonally dominant, and thus the positivity of c is not guaranteed (the positivity of ρ is enforced the same way as in the parabolic-parabolic case). At the same time, in our numerical experiments, we have never observed any negative values of c. We would also like to stress that even if some small negative values of c appear, this would not lead to any negative blowup similar to the ones observed in (22), where appearance of small negative values of ρ led the computed cell density to a meaningless negative blowup.

2.2   Numerical Experiments

In this section, we test the developed second- and fourth-order hybrid FVFD schemes on two numerical examples. In all of the examples, we have employed the zero Neumann boundary conditions implemented using the standard ghost cell/ghost point technique. The second-order scheme is implemented using the three-state third-order SSP RK method, while the fourth-order scheme is realized using the five-stage fourth-order SSP RK method. In both cases, time steps were chosen to ensure the positivity of the computed densities and changed adaptively according to the CFL conditions identified in Theorems 2.1.1 and 2.1.2 for the second-order scheme and in Theorem 2.1.3 for the fourth-order scheme.

Example 1—Fast Blowup in the PKS Chemotaxis Model

In the first example taken from (22), we consider the initial-boundary value problem (IBVP) for the PKS system Eq. 1.1 with $\chi = \gamma_c = \gamma_\rho = \alpha = 1$ in a square domain $[-\frac{1}{2}, \frac{1}{2}] \times [-\frac{1}{2}, \frac{1}{2}]$ subject to the radially symmetric bell-shaped initial data:

$$\rho(x, y, 0) = 1000\, e^{-100(x^2+y^2)}, \quad c(x, y, 0) = 500\, e^{-50(x^2+y^2)}. \tag{2.42}$$

As it was demonstrated in (22), the solution of this IBVP is expected to develop a δ-type singularity at the center of the computational domain in a very short time.

We first implement the proposed second- and fourth-order hybrid FVFD schemes on a uniform mesh with $\Delta x = \Delta y = 1/201$. The cell densities computed at two pre-blowup times $t = 10^{-6}$ and 5×10^{-6}, at which the solution still preserves its initial shape, are shown in Figure 2.1. We also compute the solution at near-blowup $t = 7.5 \times 10^{-5}$ and past-blowup $t = 1.5 \times 10^{-4}$ times, and plot the obtained cell densities in Figure 2.2. As one can see, the obtained solutions are oscillation-free and the spiky structure is quite accurately resolved by both schemes, but the blowup phenomenon is better resolved by the fourth-order method.
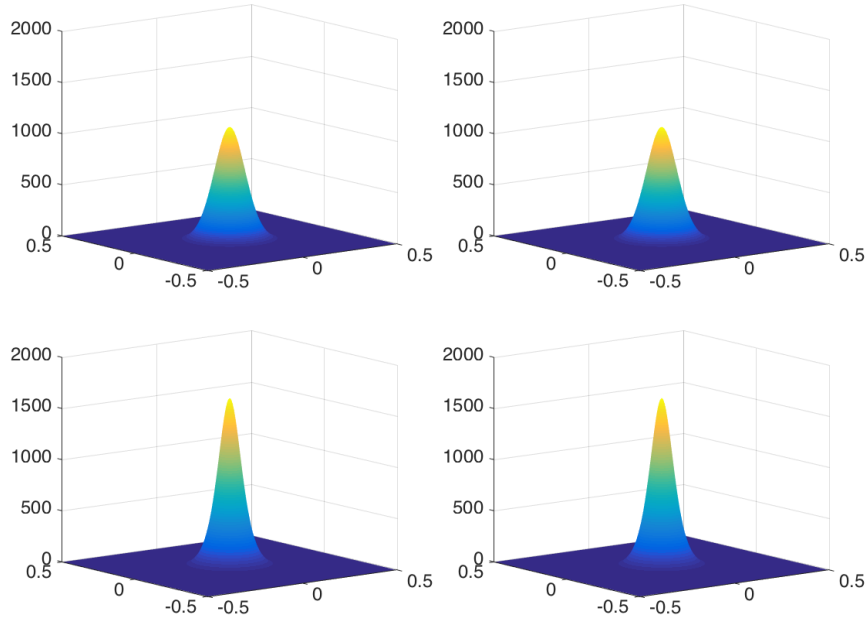
Figure 2.1: Example 1: ρ computed by the proposed second- (left column) and fourth-order (right column) schemes on a uniform mesh with $\Delta x = \Delta y = 1/201$ at pre-blowup times $t = 10^{-6}$ (top row) and 5×10^{-6} (bottom row).

Next, we conduct a comparison study of the second- and fourth-order schemes. We
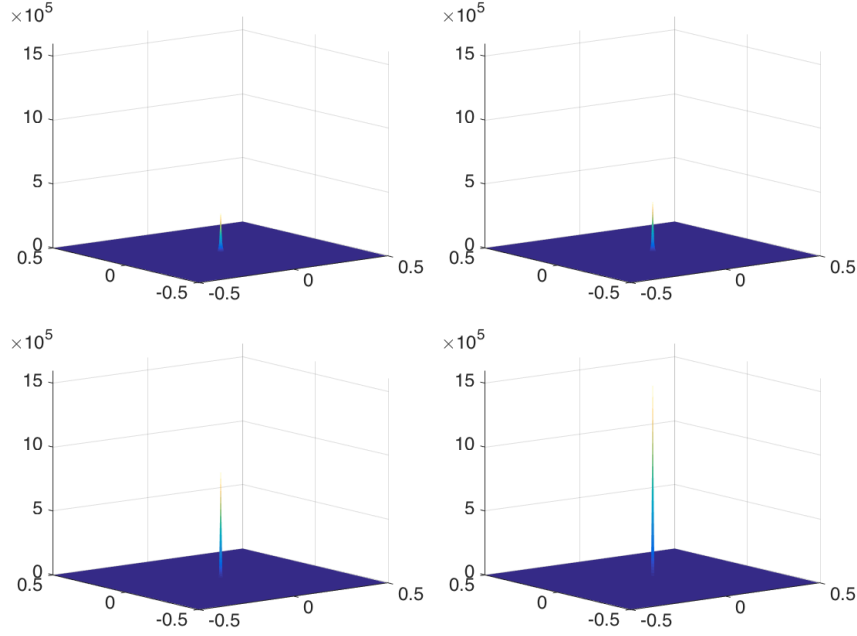
Figure 2.2: Example 1: The same as in Figure Fig. 2.1, but at near-blowup 7.5×10^{-5} (top) and past-blowup 1.5×10^{-4} (bottom) times.

first perform the accuracy test at a small pre-blowup time $t = 10^{-6}$, at which the solution of the IBVP Eq. 1.1, Eq. 2.42 is smooth. In order to measure the convergence rate, we compute the solutions on a five different grids and compare the obtained results with the reference solution, computed by the proposed fourth-order method on a fine mesh with $\Delta x = \Delta y = 1/801$. The results are presented in Table 2.1, where one can clearly observe an expected or even higher order of convergence for both ρ and c.

Finally, we numerically investigate the blowup in the PKS system by plotting the time evolution of $\|\rho\|_\infty$ computed by both the second- and fourth-order schemes on three consecutive meshes; see Figure 2.3. The vertical lines in these figures indicate the numerical blowup times that are the times by which the value of $\|\rho\|_\infty$ increases by a factor of four as the grid is refined since the magnitude of finite-volume approximations of a δ-type singularity is always proportional to $1/(\Delta x \Delta y)$. As one can observe, the numerical blowup times

Table 2.1: Example 1: L^∞-errors for ρ and c and experimental rates of convergence for the second- (left) and fourth-order (right) schemes.

grid	ρ-error	rate	c-error	rate		grid	ρ-error	rate	c-error	rate
101×101	2.88E-1		2.44E-4			101×101	7.56E-4		1.59E-6	
201×201	6.90E-2	2.09	6.18E-5	2.00		201×201	1.26E-5	5.94	1.01E-7	4.00
301×301	3.04E-2	2.03	2.76E-5	2.00		301×301	1.15E-6	5.95	1.99E-8	4.04
401×401	1.71E-2	2.01	1.55E-5	2.00		401×401	2.07E-7	5.96	6.03E-9	4.16
501×501	1.09E-2	2.01	9.95E-6	2.00		501×501	5.34E-8	6.09	2.24E-9	4.46

for the second- and fourth-order schemes are quite different: the solution computed by the second-order scheme blows up at about $t \approx 1.2 \times 10^{-4}$, while its fourth-order counterpart blows up at an earlier time $t \approx 1.1 \times 10^{-4}$. This together with the fact that the magnitude of the fourth-order solution is about twice larger than the magnitude of the second-order one at the time of blowup, indicate that the use of a higher-order scheme is advantageous when the blowup time should be estimated numerically.

Figure 2.3: Example 1: Time evolution of $\|\rho\|_\infty$ for the second- (left) and fourth-order (right) schemes on three consecutive meshes. The numerical blowup times are indicated by the corresponding vertical lines.

46

Example 2—Slow Blowup in the PKS Chemotaxis Model

In this example also taken from (22), we consider the same IBVP as in Example 1, but with the uniform initial condition for the chemoattractant concentration:

$$c(x, y, 0) = 0.$$

According to (22), the solution of this IBVP develops the same δ-type singularity as in Example 1, but at a much later time.

We implement the proposed second- and forth-order hybrid FVFD schemes on a uniform mesh with $\Delta x = \Delta y = 1/201$. The cell densities computed at a pre-blowup time $t = 0.3$ and a past-blowup time $t = 0.4$ are presented in Figure 2.4. One can observe that the obtained solutions are oscillation-free, and both of the second- and fourth-order scheme can capture the spiky structure of the solutions. The blowup phenomenon is however better resolved by the fourth-order scheme. This can be seen if the maximum cell density values are compared: while for the second-order results, $\max_x \rho(x, 0.3) \approx 1626.7$, the fourth-order maximum is substantially larger, $\max_x \rho(x, 0.3) \approx 1713.9$.

We also numerically study the blowup phenomenon by plotting the time evolution of $\|\rho\|_\infty$ computed by both the second- and fourth-order schemes on three consecutive meshes with $\Delta x = \Delta y = 1/101$, $1/201$ and $1/801$; see Figure 2.5. The numerical blowup time for both schemes are measured based on the way the magnitude of ρ increases (as it has been explained in Example 1): the second-order solution blows up at $t \approx 0.375$, while the fourth-order solution blows up at an earlier time $t \approx 0.35$. One can also see that the magnitude of the fourth-order solution is about twice as large as the magnitude of the second-order one at the past-blowup time. These two facts confirm the advantage of the higher-order scheme when the blowup time should be estimated numerically.
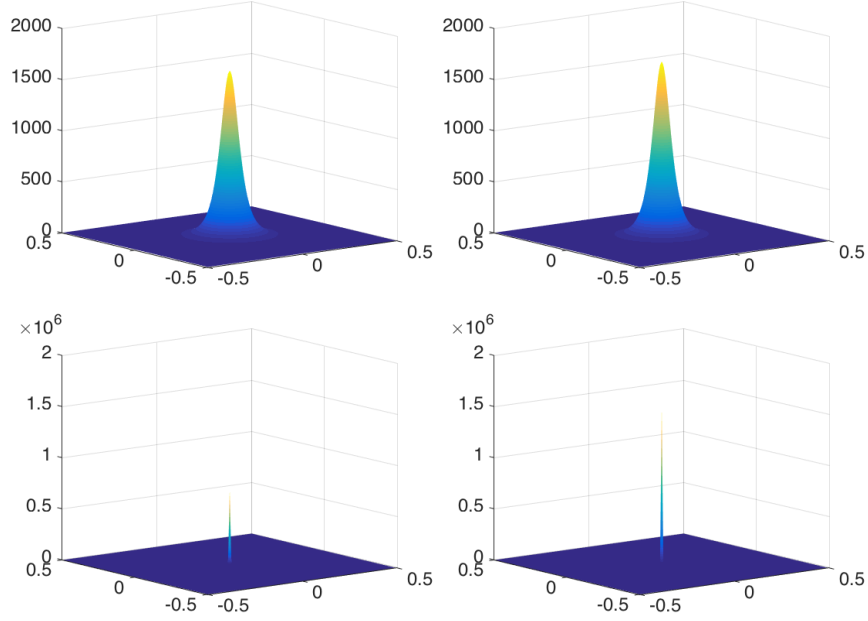
Figure 2.4:   Example 2: ρ computed by the proposed second- (left column) and fourth-order (right column) schemes on a uniform mesh with $\Delta x = \Delta y = 1/201$ at pre-blowup $t = 0.3$ (top row) and past-blowup $t = 0.4$ (bottom row) times.
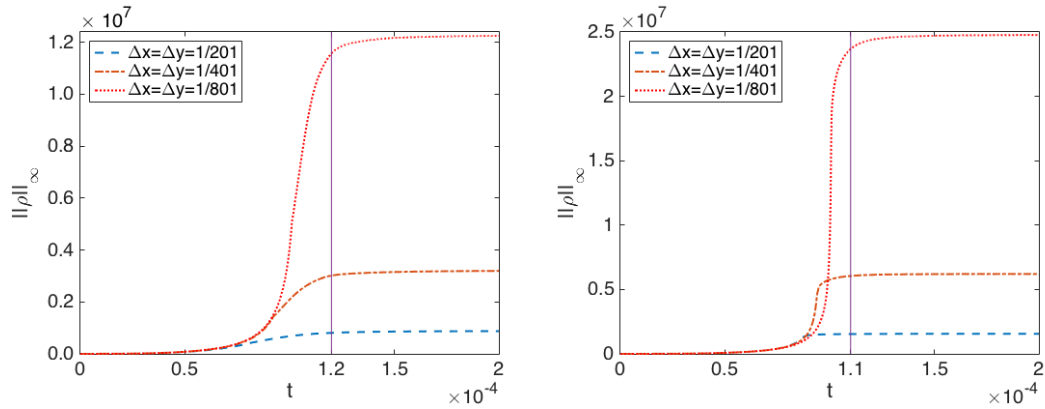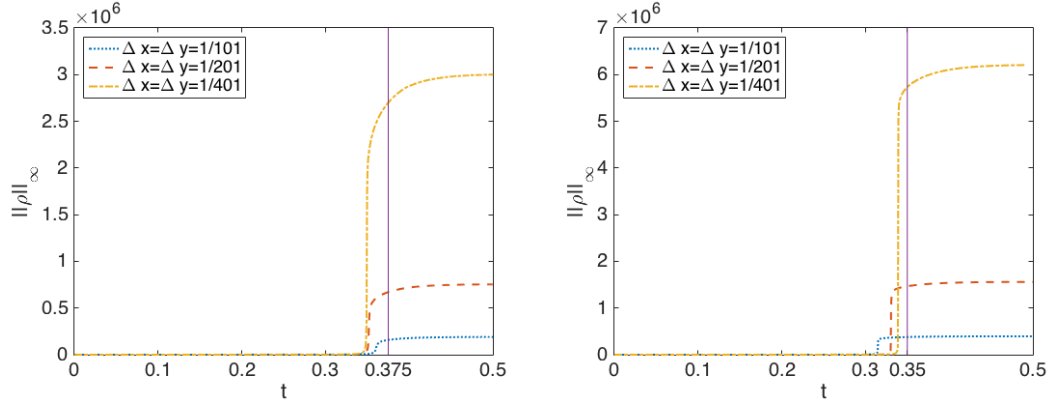

Figure 2.5:   Example 2: Time evolution of $\|\rho\|_\infty$ for the second- (left) and fourth-order (right) schemes on three consecutive meshes. The numerical blowup times are indicated by the corresponding vertical lines.

It would also be instructive to look at the actual time-step size Δt used in the numerical simulations. To this end, we provide Figure 2.6, where we plot Δt as a function of time

48

t computed by both the second- and fourth-order schemes with $\Delta x = \Delta y = 1/201$. The time-step size is chosen according to the CFL condition specified in Eq. 2.13 to guarantee the positivity of the computed solution for both the second- and fourth-order schemes (see Remark 2.1.2). As one can see, the upper bound on the time step in Eq. 2.13 is a minimum of four terms: The first two, $\Delta x/(8a)$ and $\Delta y/(8b)$, are related to the chemotaxis flux in the first equation in Eq. 1.1, while the third and fourth ones are due to the parabolic terms in the system Eq. 1.1. In the (near) blowup regime, a and b in Eq. 2.13 become large and thus the first two terms determine the size of time steps, in which case an explicit method is efficient enough. However, when a and b are small, the third and fourth terms in Eq. 2.13 dominate, which reduces the efficiency of the explicit method. One of the ways to overcome this difficulty is to use positivity preserving implicit-explicit (IMEX) methods (4; 5; 65) as long as a and b remain relatively small; see, e.g., (22). The implementation of an IMEX algorithm is outside the scope of the current study.
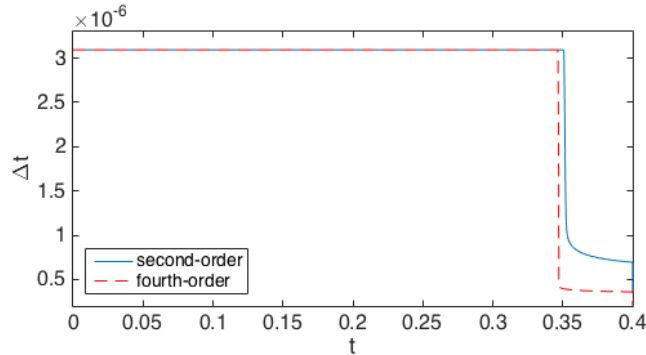
Figure 2.6: Example 2: Time step size Δt as a function of time t computed by both the second- and fourth-order schemes with $\Delta x = \Delta y = 1/201$.

Example 3—Blowup in the Two-Species Chemotaxis Model

In this example, we consider the IBVP for two-species chemotaxis model

$$\begin{cases} (\rho_1)_t + \nabla\cdot(\chi_1\rho_1\nabla c) = \Delta\rho_1, \\ (\rho_2)_t + \nabla\cdot(\chi_2\rho_2\nabla c) = \Delta\rho_2, \quad (x,y)\in\Omega\subset\mathbb{R}^2, \ t>0, \\ \Delta c + \rho_1 + \rho_2 - c = 0, \end{cases} \quad (2.43)$$

which was proposed in (130) and then further studied both analytically, (31; 41; 42; 43; 44; 46; 83), and numerically, (75). In Eq. 2.43, $\rho_1(x,y,t)$ and $\rho_2(x,y,t)$ denote the cell densities of the first and second non-competing species, $c(x,y,t)$ stands for the chemoattractant concentration, $\chi_2 > \chi_1 > 0$ are the chemotactic sensitivity constants for the first and second species, respectively.

As it was proven in (41; 43), solutions of Eq. 2.43 may either remain smooth (with decaying maxima of both ρ_1 and ρ_2) or blow up in a finite time. Moreover, only simultaneous blowup is possible. However, in the blowup regime ρ_1 and ρ_2 may develop different types of singularities depending on the values of χ_1 and χ_2 and on the initial mass of each species:

$$m_1 := \int_\Omega \rho_1(x,y,0)\,dx\,dy \quad \text{and} \quad m_2 := \int_\Omega \rho_2(x,y,0)\,dx\,dy.$$

In particular, if
$$\frac{8\pi m_1}{\chi_1} + \frac{8\pi m_2}{\chi_2} - (m_1+m_2)^2 \geq 0 \quad \text{and} \quad m_2 \geq \frac{8\pi}{\chi_2}, \quad (2.44)$$

then ρ_2 is expected to develop much stronger singularity than ρ_1.

We now numerically study a specific example taken from (75), where the system Eq. 2.43 with $\chi_1 = 1$ and $\chi_2 = 20$ was considered on the domain $\Omega = [-3,3]\times[-3,3]$ and subject to

50

the bell-shaped initial data:

$$\rho_1(x,y,0)=\rho_2(x,y,0)=50e^{-100(x^2+y^2)}. \tag{2.45}$$

In this case, the total masses are $m_1=m_2\approx\pi/2$ and the condition Eq. 2.44 is satisfied.

Although the schemes presented in §2.1 have been derived for the one-species PKS model, they can be straightforwardly extended to the two-species system Eq. 2.43 since the equations for ρ_1 and ρ_2 are only coupled through the c-equation. We note that a detailed description of the second-order hybrid FVFD scheme for the two-species model can be found in (75).

We first conduct numerical simulations using both the second- and fourth-order schemes on a uniform mesh with $\Delta x=\Delta y=6/201$. The cell densities ρ_1 and ρ_2 computed at time $t=3.3\times10^{-3}$ are presented in Figure 2.7. As in Example 1, one can observe that while both schemes accurately capture the spiky structure of the solution, the fourth-order scheme achieves a higher resolution of the blowup phenomenon.

Next, we numerically investigate the blowup behavior of the system Eq. 2.43 by plotting the time evolution of $\|\rho_1\|_\infty$ and $\|\rho_2\|_\infty$ computed by both second- and fourth-order schemes on the four consecutive uniform meshes with $\Delta x=\Delta y=6/201,6/401,6/801$ and $6/1601$; see Figures 2.8 and 2.9. We measure the numerical blowup time for both schemes based on the way the magnitude of ρ_2 increases (as it has been explained in Example 1) and observe that the second-order solution blows up at about $t=3.8\times10^{-3}$, while the fourth-order solution blows up a little earlier at about $t=3.3\times10^{-3}$. However, $\|\rho_1\|_\infty$ behaves completely different from $\|\rho_2\|_\infty$: it first decreases, then increases and at the blowup time the maximum of ρ_1 is significantly smaller than the maximum of ρ_2. Looking at the results in Figure 2.8, one may conclude that only ρ_2 blows up, but the analytical results proved in
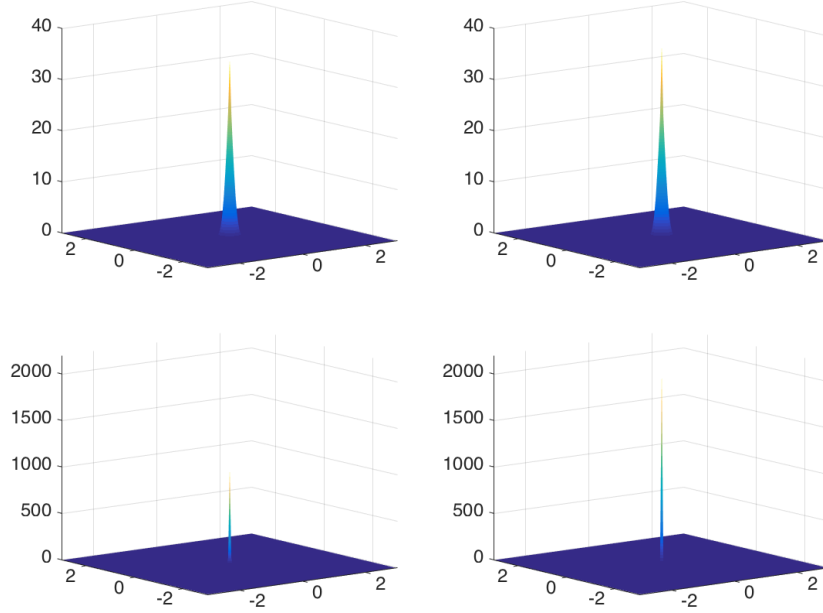
Figure 2.7: Example 3: ρ_1 (top row) and ρ_2 (bottom row) computed by the second- (left column) and fourth-order (right column) schemes on a uniform mesh with $\Delta x = \Delta y = 6/201$ at time $t = 3.3 \times 10^{-3}$.

(41; 43) state that only simultaneous blowup is possible, which suggests that the maximum of ρ_1 should also blow up at about $t = 3.3 \times 10^{-3}$ though at a much slower rate than the maximum of ρ_2. In order to numerically verify this, we perform a mesh refinement study and monitor $\|\rho_1\|_\infty$ and $\|\rho_2\|_\infty$ as functions of Δx, which is equal to Δy in this numerical experiment. These functions are presented in Figure 2.10. As one can see from Figure 2.10 (left), the maximum of ρ_1 computed by the second-order scheme behaves like the function $f_1^{II}(\Delta x) = 9(\frac{3.51}{\Delta x} + 90)^{1/4}$, while the maximum of ρ_1 computed by the fourth-order scheme behaves like the function $f_1^{IV}(\Delta x) = 11.15(\frac{2.94}{\Delta x} + 25)^{1/4}$. This shows that ρ_1 blows up at the rate of

$$\|\rho_1\|_\infty \sim \frac{1}{(\Delta x \Delta y)^{\frac{1}{8}}}.$$

At the same time, Figure 2.10 (right) illustrates that $\|\rho_2\|_\infty$ behaves like $f_2^{II}(\Delta x) = \frac{0.756}{(\Delta x)^2}$ for the second-order results and like $f_2^{IV}(\Delta x) = \frac{1.656}{(\Delta x)^2}$ for the fourth-order ones. This indicates that ρ_2 collapses to a δ-type singularity as

$$\|\rho_2\|_\infty \sim \frac{1}{\Delta x \Delta y}.$$
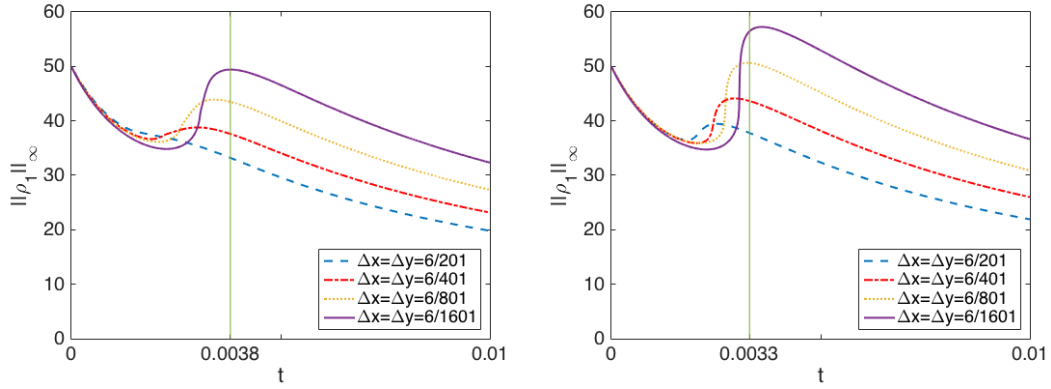
Figure 2.8:   Example 3: $\|\rho_1\|_\infty$ as a function of t computed by the second- (left) and fourth-order (right) schemes. The numerical blowup times are indicated by the corresponding vertical lines.

We would like to emphasize that even though both the second- and fourth-order schemes asymptotically behave in a similar way in the blowup regime, the magnitude of both ρ_1 and ρ_2 are substantially larger in the fourth-order computations; see Figures 2.8–2.10. This clearly demonstrates the main advantage of using higher-order methods for the two-species chemotaxis system. At the same time, it seems to be necessary to use either adaptive mesh refinement or adaptive moving mesh technique to numerically detect the blowup in ρ_1 in a more convincing way. Development of adaptive techniques for the
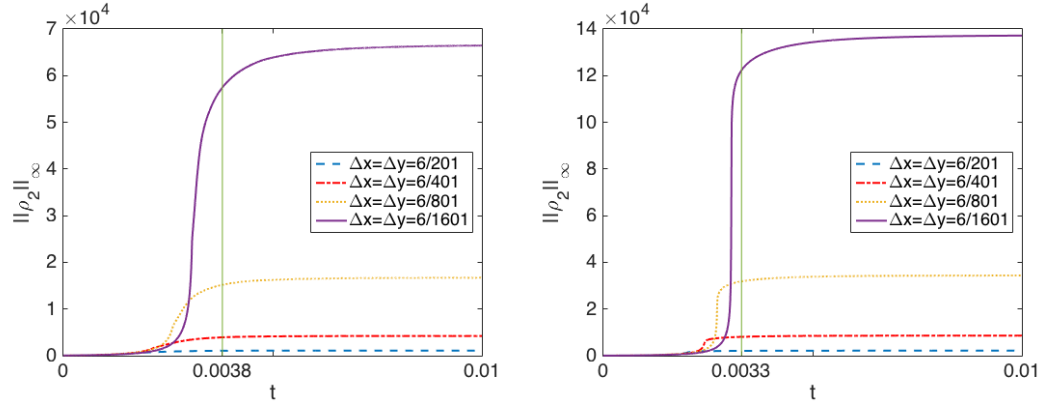
Figure 2.9: Example 3: $\|\rho_2\|_\infty$ as a function of t computed by the second- (left) and fourth-order (right) schemes. The numerical blowup times are indicated by the corresponding vertical lines.
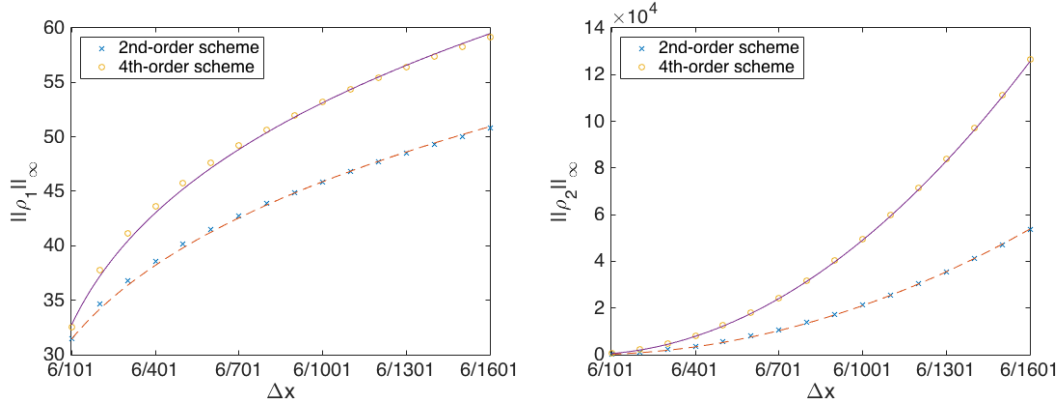
Figure 2.10: Example 3: $\|\rho_1(x, y, 0.0033)\|_\infty$ computed by the second- and fourth-order schemes plotted along with the functions $f_1^{II}(\Delta x) = 9(\frac{3.51}{\Delta x} + 90)^{1/4}$ and $f_1^{IV}(\Delta x) = 11.15(\frac{2.94}{\Delta x} + 25)^{1/4}$ (left) and $\|\rho_2(x, y, 0.0033)\|_\infty$ computed by the second- and fourth-order schemes plotted along with the functions $f_2^{II}(\Delta x) = \frac{0.756}{(\Delta x)^2}$ and $f_2^{IV}(\Delta x) = \frac{1.656}{(\Delta x)^2}$ (right) for $\Delta x = \Delta y = 6/101, 6/201, \ldots, 6/1601$.

chemotaxis systems is beyond the scope of this paper and is left for future studies.

3

POSITIVITY-PRESERVING HYBRID FINITE-VOLUME-FINITE-DIFFERENCE METHODS FOR CHEMOTAXIS-FLUID SYSTEMS

In this chapter, we derive and study a hybrid finite-volume-finite-difference scheme for the chemotaxis-fluid systems Eq. 1.15 defined on the domain with a curved boundary.

Our FVFD method is a splitting method which evolves the velocity filed of the fluid by solving the incompressible Navier-Stokes equation using the projection method (see, e.g., (92)), then solves the oxygen concentration equation by a finite-volume upwind scheme to update the oxygen concentration c. Lastly, the bacteria concentration equation is solved by a finite-volume method.

This chapter is organized as follows. First, in §3.1 we introduce a dimensionless system Eq. 3.3 which is obtained by rescaling the chemotaxis-fluid system Eq. 1.15. In §3.2, we develop a FVFD scheme for the chemotaxis-fluid system Eq. 3.3, in §3.2.1 we briefly introduce the projection method we applied to evolve the incompressible Navier-Stokes equations in system Eq. 3.3, in §3.2.2, we illustrate the finite-volume upwind scheme for the chemoattractant (oxygen) concentration equation and the finite-volume upwind scheme for the bacteria concentration equation was derived in §3.2.3. Finally, in §3.3, we implement the proposed scheme on several numerical examples.

3.1   Scaling and numerical set-up

In this dissertation, we consider the chemotaxis-fluid system Eq. 1.15 proposed in (121), which is defined in a two-dimensional domain with a curved boundary on the top (see Fig. 1.1 and Fig. 1.2) and subject to the boundary conditions Eq. 1.16 and Eq. 1.17. We denote a characteristic length (for example, the depth of the fluid drop) by L and the characteristic bacteria concentration by ρ_r, and rescale the variables in system Eq. 1.15 according to Tuval et al. (121):

$$\mathbf{x}' = \frac{\mathbf{x}}{L}, \quad t' = \frac{D_\rho}{L^2}t, \quad c' = \frac{c}{c_{air}}, \quad \rho' = \frac{\rho}{\rho_r}, \quad p' = \frac{L^2}{\eta D_\rho}p, \quad \mathbf{u}' = \frac{L}{D_\rho}\mathbf{u}. \tag{3.1}$$

56

This rescaling of variables will nondimensionalize the system Eq. 1.15 and give us five dimensionless parameters to characterize it:

$$\alpha := \frac{\chi c_{air}}{D_\rho}, \quad \beta := \frac{\kappa \rho_r L^2}{c_{air} D_\rho}, \quad \gamma := \frac{V_b \rho_r g(\rho_b - \hat{\rho})L^3}{\eta D_\rho}, \quad \delta := \frac{D_c}{D_\rho}, \quad \mathbf{Sc} := \frac{\eta}{D_\rho \hat{\rho}} \tag{3.2}$$

where **Sc** is the Schmidt number and c_{air} is the oxygen concentration in the air surround the fluid drop. Three of these parameters, α, δ and **Sc**, are determined by the properties of bacteria, fluid and air, particularly for *Bacillus subtilis* in water, we have $\alpha = 10$, $\delta = 5$ and **Sc** $= 500$ (see, e.g. (121; 21)). The remaining two parameters β and γ depend on the characteristic length L and the characteristic bacteria concentration ρ_r, and will vary in different examples. Using these dimensionless parameters and the rescaled variables without the prime notation, the chemotaxis-fluid system can be written as:

$$\begin{cases} \rho_t + \nabla \cdot (\mathbf{u}\rho) + \alpha \nabla \cdot [\rho r(c)\nabla c] = \Delta \rho, \\ c_t + \nabla \cdot (\mathbf{u}c) = \delta \Delta c - \beta r(c)\rho, \\ \mathbf{u}_t + \mathbf{u} \cdot \nabla \mathbf{u} + \mathbf{Sc}\nabla p = \mathbf{Sc}\Delta \mathbf{u} - \gamma \mathbf{Sc}\rho z, \\ \nabla \cdot \mathbf{u} = 0, \end{cases} \quad (x,y) \in \Omega \subset \mathbb{R}^2, \ t \geq 0. \tag{3.3}$$

The rescaled boundary conditions for the system Eq. 3.3 are:

$$\alpha \rho r(c)c_{\mathbf{n}} - \rho_{\mathbf{n}} = 0, \ c = 1, \ \mathbf{u} \cdot \mathbf{n} = 0, \ (\mathbf{n} \cdot (\nabla \mathbf{u} + \nabla \mathbf{u}^T)) \times \mathbf{n} = 0, \ \forall (x,y) \in \partial \Omega_{top}, \tag{3.4}$$

and

$$\rho_y = c_y = 0, \ \mathbf{u} = \mathbf{0}, \ \forall (x,y) \in \partial \Omega_{bot}. \tag{3.5}$$

57

3.2   Derivation of the finite-volume-finite-difference scheme

In this section, we derive a finite-volume-finite-difference method for chemotaxis system Eq. 3.3 defined in a domain Ω with curve boundary (see Fig. 1.2). The system Eq. 3.3 can be written in coordinate form as follows:

$$\begin{cases} \rho_t + \left[(u + \alpha r(c)c_x)\rho\right]_x + \left[(v + \alpha r(c)c_y)\rho\right]_y = \Delta\rho, \\ c_t + (uc)_x + (vc)_y = \delta\Delta c - \beta r(c)\rho, \\ u_t + uu_x + vu_y + \mathbf{Sc}p_x = \mathbf{Sc}\Delta u, \qquad\qquad (x,y)\in\Omega\subset\mathbb{R}^2, \ \ t \geq 0. \qquad (3.6) \\ v_t + uv_x + vv_y + \mathbf{Sc}p_y = \mathbf{Sc}\Delta v - \mathbf{Sc}\gamma\rho, \\ u_x + v_y = 0, \end{cases}$$

where u and v are the horizontal and vertical component of the velocity field $\mathbf{u}$. In this system Eq. 3.6, the oxygen concentration c is convected by the flow, diffused and affected by the oxygen uptake source term $-\beta r(c)\rho$. The bacteria concentration ρ is governed by convection chemotaxis fluxes, $(u + \alpha r(c)c_x)\rho$ and $(v + \alpha r(c)c_y)\rho$, and the diffusion term. As shown in Fig. 1.2, the domain of the system Ω is irregular (has a curved boundary on the top part), so we apply the augmented method to solve the system Eq. 3.6. In the numerical scheme presented, instead of just solving the system Eq. 3.6 in its exact domain Ω, we embed the the domain Ω in to a rectangular computational domain $\overline{\Omega} = [a,b]\times[c,d]$ which contains Ω and the bottom side coincides with the solid surface (the no-slip bottom boundary $\partial\Omega_{bot}$ of the exact domain). And for (x,y) in the domain $\overline{\Omega}\backslash\Omega$, we assume that the bacteria concentration ρ, oxygen concentration c and the fluid velocity $\mathbf{u} = (u,v)^T$

satisfy the following equations:

$$\begin{cases} \rho_t = \Delta\rho, \\ c_t = \delta\Delta c, \\ u_t = \mathbf{Sc}\Delta u, \\ v_t = \mathbf{Sc}\Delta v, \end{cases} \quad (x,y)\in\overline{\Omega}\backslash\Omega, \;\; t \geq 0. \tag{3.7}$$

Then, we can treat the problem as an interfaced domain problem defined in the rectangular computational domain $\overline{\Omega}$ and we can treat the top boundary of the exact domain $\partial\Omega_{top}$ as an interface in $\overline{\Omega}$ and apply the immersed interface method to evolve the systems Eq. 3.6 and Eq. 3.7 on the entire computational domain $\overline{\Omega}$.

From one time level to the next, a splitting method was applied to evolve the velocity $\mathbf{u}$, oxygen concentration c and bacteria concentration ρ separately. We evolve the velocity $\mathbf{u}$ in time by solving the incompressible Navier-Stokes equation in Eq. 3.6 using the projection method (see, e.g., (92)). The oxygen-concentration equation and bacteria-concentration equation are solved by a finite-volume upwind method.

To apply the splitting method, we divide the system Eq. 3.6 into three different parts. The bacteria concentration equation:

$$\rho_t + \left[(u + \alpha r(c)c_x)\rho\right]_x + \left[(v + \alpha r(c)c_y)\rho\right]_y = \Delta\rho, \tag{3.8}$$

with boundary conditions:

$$\alpha\rho\, r(c)c_{\mathbf{n}} - \rho_{\mathbf{n}} = 0, \quad \forall(x,y)\in\partial\Omega_{top}, \tag{3.9}$$

and

$$\rho_y = 0, \quad \forall (x, y) \in \partial \Omega_{bot}. \tag{3.10}$$

The oxygen concentration equation:

$$c_t + (uc)_x + (vc)_y = \delta \Delta c - \beta r(c) \rho, \tag{3.11}$$

with the boundary conditions:

$$c = 1, \quad \forall (x, y) \in \partial \Omega_{top}, \tag{3.12}$$

and

$$c_y = 0, \quad \forall (x, y) \in \partial \Omega_{bot}. \tag{3.13}$$

And the fluid equation:

$$\begin{cases} u_t + u u_x + v u_y + \mathbf{Sc} p_x = \mathbf{Sc} \Delta u, \\ v_t + u v_x + v v_y + \mathbf{Sc} p_y = \mathbf{Sc} \Delta v - \mathbf{Sc} \gamma \rho, \\ u_x + v_y = 0, \end{cases} \tag{3.14}$$

with boundary conditions:

$$\mathbf{u} \cdot \mathbf{n} = 0, \ (\mathbf{n} \cdot (\nabla \mathbf{u} + \nabla \mathbf{u}^T)) \times \mathbf{n} = 0, \quad \forall (x, y) \in \partial \Omega_{top}, \tag{3.15}$$

and

$$u = 0, \ v = 0, \quad \forall (x, y) \in \partial \Omega_{bot}. \tag{3.16}$$

Given the solutions $u(x, y, t)$, $v(x, y, t)$, $c(x, y, t)$ and $\rho(x, y, t)$ at time t, we first solve

60

the incompressible Navier-Stokes equation Eq. 3.14 to obtain the solutions at time $t + \Delta t$ by the projection method proposed in (92).

For the oxygen concentration equation Eq. 3.11, we use the evolved velocity at time $t + \Delta t$, take care of the diffusion term implicitly and discretize the equation in time by forward Euler. This leads to an elliptic equation. In the exact domain Ω, we have:

$$\delta \Delta c(x, y, t + \Delta t) - \frac{1}{\Delta t} c(x, y, t + \Delta t) = \left[u(x, y, t + \Delta t) c(x, y, t) \right]_x + \left[v(x, y, t + \Delta t) c(x, y, t) \right]_y$$
$$+ \beta r(c(x, y, t)) \rho(x, y, t) - \frac{1}{\Delta t} c(x, y, t),$$

(3.17)

while in the domain $\overline{\Omega} \backslash \Omega$, the equation is:

$$\delta \Delta c(x, y, t + \Delta t) - \frac{1}{\Delta t} c(x, y, t + \Delta t) = -\frac{1}{\Delta t} c(x, y, t),$$

(3.18)

At last, we use a similar strategy to solve the bacteria concentration equation Eq. 3.8 based on the updated solutions $u(x, y, t + \Delta t)$, $v(s, y, t + \Delta t)$ and $c(x, y, t + \Delta t)$, which gives us:

$$\Delta \rho(x, y, t + \Delta t) - \frac{1}{\Delta t} \rho(x, y, t + \Delta t) = \left\{ \left[u(x, y, t + \Delta t) + \alpha r(c(x, y, t + \Delta t)) c_x(x, y, t + \Delta t) \right] \rho(x, y, t) \right\}_x$$
$$+ \left\{ \left[v(x, y, t + \Delta t) + \alpha r(c(x, y, t + \Delta t)) c_y(x, y, t + \Delta t) \right] \rho(x, y, t) \right\}_y$$
$$- \frac{1}{\Delta t} \rho(x, y, t),$$

(3.19)

for $(x, y) \in \Omega$, and when $(x, y) \in \overline{\Omega} \backslash \Omega$, the elliptic equation is:

$$\Delta \rho(x, y, t + \Delta t) - \frac{1}{\Delta t} \rho(x, y, t + \Delta t) = -\frac{1}{\Delta t} \rho(x, y, t).$$

(3.20)

3.2.1 Projection method for the fluid equation

In this section, we briefly illustrate the numerical method we used to solve the fluid equations Eq. 3.14 in the chemotaxis-fluid system. There are many different versions of the projection method for the incompressible Navier-Stokes equations (see, e.g. (9; 14; 125; 70) and references therein), and the one we used is originally posted in (14) and modified for irregular domain case in (92) which is based on the pressure increment formulations. We consider the equation Eq. 3.14 in the computational rectangular domain $\overline{\Omega} = [a, b] \times [c, d]$, where we introduce a Cartesian mesh consisting of cells $I_{j,k} := [x_{j-\frac{1}{2}}, x_{j+\frac{1}{2}}] \times [y_{k-\frac{1}{2}}, y_{k+\frac{1}{2}}]$ with uniform size $\Delta x \Delta y$ for simplicity, that is $x_{j+\frac{1}{2}} - x_{j-\frac{1}{2}} \equiv \Delta x$ and $y_{k+\frac{1}{2}} - y_{k-\frac{1}{2}} \equiv \Delta y$ for all j, k. On this mesh, given the velocities (u^m, v^m), the pressure p^m at time level t^m and an initial guess of augmented variable $\mathbf{q}^{m+1} = (q_1, q_2)$, the solutions at time t^{m+1} are evolved by the following steps.

Step 1: Prediction step

$$
\frac{u^*_{j,k} - u^m_{j,k}}{\Delta t} =
\begin{cases}
-\mathbf{Sc}(p^m_x)_{j,k} - u^m_{j,k}(u^m_x)_{j,k} - v^m_{j,k}(u^m_y)_{j,k} + \mathbf{Sc}\Delta_{j,k} u^*, & \mathbf{x} \in \Omega, \\
\mathbf{Sc}\Delta u^m, & \mathbf{x} \in \overline{\Omega}\backslash\Omega,
\end{cases}
$$

$$
\frac{v^*_{j,k} - v^m_{j,k}}{\Delta t} =
\begin{cases}
-\mathbf{Sc}(p^m_y)_{j,k} - u^m_{j,k}(v^m_x)_{j,k} - v^m_{j,k}(v^m_y)_{j,k} + \mathbf{Sc}\Delta_{j,k} v^* - \mathbf{Sc}\gamma \rho^m_{j,k}, & \mathbf{x} \in \Omega, \\
\mathbf{Sc}\Delta v^m, & \mathbf{x} \in \overline{\Omega}\backslash\Omega,
\end{cases}
$$
$$\tag{3.21}$$

with jump conditions

$$
[u^*]_{\partial\Omega_{top}} = 0, \quad [v^*]_{\partial\Omega_{top}} = 0, \quad \left[\frac{\partial u^*}{\partial \mathbf{n}}\right]_{\partial\Omega_{top}} = \mathbf{q}^{m+1}_u, \quad \left[\frac{\partial v^*}{\partial \mathbf{n}}\right]_{\partial\Omega_{top}} = \mathbf{q}^{m+1}_v, \tag{3.22}
$$

and boundary conditions

$$
u^*|_{\partial\overline{\Omega}} = 0, \quad v^*|_{\partial\overline{\Omega}} = 0. \tag{3.23}
$$

Step 2: Projection step

$$\Delta_{j,k}\phi^{m+1} = \frac{(u_x^*)_{j,k} + (v_y^*)_{j,k}}{\mathbf{Sc}\Delta t}, \quad \mathbf{x} \in \overline{\Omega}, \tag{3.24}$$

with jump conditions

$$[\phi^{m+1}]_{\partial\Omega_{top}} = 0, \quad \left[\frac{\partial\phi^{m+1}}{\partial\mathbf{n}}\right]_{\partial\Omega_{top}} = 0, \tag{3.25}$$

and boundary conditions

$$\frac{\partial\phi^{m+1}}{\partial\mathbf{n}}\bigg|_{\partial\overline{\Omega}} = 0. \tag{3.26}$$

$$\begin{cases} u_{j,k}^{m+1} = u_{j,k}^* - \mathbf{Sc}\Delta t(\phi_x^{m+1})_{j,k}, & \mathbf{x} \in \overline{\Omega}, \\ v_{j,k}^{m+1} = v_{j,k}^* - \mathbf{Sc}\Delta t(\phi_y^{m+1})_{j,k}, & \mathbf{x} \in \overline{\Omega} \\ \nabla p_{j,k}^{m+1} = \nabla p_{j,k}^m + \nabla\phi_{j,k}^{m+1}, & \mathbf{x} \in \Omega. \end{cases} \tag{3.27}$$

Step 3: Interpolation and computing the residual of the boundary conditions

$$E_1^{m+1} = \mathbf{u}\cdot\mathbf{n}, \text{ and } E_2^{m+1} = (\mathbf{n}\cdot(\nabla\mathbf{u}+\nabla\mathbf{u}^T))\times\mathbf{n} \text{ on } \partial\Omega_{top}. \tag{3.28}$$

Step 1 and step 2 are the traditional steps of the projection method for the Navier-Stokes equation in an interfaced domain. The augmented variables $\mathbf{q}_u^{m+1}$ and $\mathbf{q}_v^{m+1}$ defined only along the top boundary of the exact domain $\partial\Omega_{top}$ are introduced in the prediction step and must be properly chosen to guarantee that the boundary conditions Eq. 3.15 and Eq. 3.16 are satisfied at time t^{m+1}, which means the residuals E_1^{m+1} and E_2^{m+1} computed in step 3 will equal to 0. Then, the obtained the velocity $\mathbf{u}^{m+1} = (u^{m+1}, v^{m+1})$ will satisfy the equation Eq. 3.14 in the domain Ω and the boundary conditions Eq. 3.15 and Eq. 3.16.

3.2.2 Finite-volume upwind scheme for the oxygen concentration equation

In this section, we introduce the second-order finite-volume scheme for the oxygen concentration equation Eq. 3.11. The discrete finite-volume upwind scheme for Eq. 3.17 and Eq. 3.18 can be written in the following form:

$$
\delta \Delta_{j,k} \overline{c}^{m+1} - \frac{1}{\Delta t} \overline{c}_{j,k}^{m+1} = \begin{cases} \dfrac{\mathscr{G}_{j+\frac{1}{2},k}^x - \mathscr{G}_{j-\frac{1}{2},k}^x}{\Delta x} + \dfrac{\mathscr{G}_{j,k+\frac{1}{2}}^y - \mathscr{G}_{j,k-\frac{1}{2}}^y}{\Delta y} + \beta \, r(\overline{c}_{j,k}^m) \overline{p}_{j,k}^m - \dfrac{1}{\Delta t} \overline{c}_{j,k}^m, & \mathbf{x} \in \Omega, \\[2em] -\dfrac{1}{\Delta t} \overline{c}_{j,k}^m, & \mathbf{x} \in \overline{\Omega} \backslash \Omega. \end{cases}
$$

$$(3.29)$$

with jump conditions

$$
[c^{m+1}]_{\partial \Omega_{top}} = 0, \quad \left[\frac{\partial c^{m+1}}{\partial \mathbf{n}} \right]_{\partial \Omega_{top}} = \mathbf{q}_c^{m+1} \tag{3.30}
$$

where the cell averages of the concentrations, $\overline{c}_{j,k}(t) = \frac{1}{\Delta x \Delta y} \int \int_{I_{j,k}} c(x,y,t) dx dy$, are the evolved quantities, $\mathscr{G}_{j+\frac{1}{2},k}^x$ and $\mathscr{G}_{j,k+\frac{1}{2}}^y$ are the numerical fluxes in the x- and y-direction for oxygen concentration c, respectively, and $\mathbf{q}_c^{m+1}$ is the augmented variable defined along $\partial \Omega_{top}$ which can be chosen properly by the IIM and augmented method (see §1.4). The numerical fluxes $\mathscr{G}_{j+\frac{1}{2},k}^x$ and $\mathscr{G}_{j,k+\frac{1}{2}}^y$ are computed as follows:

$$
\mathscr{G}_{j+\frac{1}{2},k}^x = u_{j+\frac{1}{2},k} c_{j+\frac{1}{2},k}, \quad \mathscr{G}_{j,k+\frac{1}{2}}^y = v_{j,k+\frac{1}{2}} c_{j,k+\frac{1}{2}}. \tag{3.31}
$$

At a regular cell interfaces, which means both of the cells corresponding to the interface are regular cell, the velocities $u_{j+\frac{1}{2},k}$ and $v_{j,k+\frac{1}{2}}$ are computed by mid point rule:

$$
u_{j+\frac{1}{2},k} = \frac{u_{j,k} + u_{j+1,k}}{2}, \quad v_{j,k+\frac{1}{2}} = \frac{v_{j,k} + v_{j,k+1}}{2}, \tag{3.32}
$$

64

and for the irregular cell interface, we approximate the velocities as:

$$u_{j+\frac{1}{2},k} = \begin{cases} u_{j,k}, & \text{if } I_{j+1,k} \in \overline{\Omega} \backslash \Omega, \\ u_{j+1,k}, & \text{if } I_{j,k} \in \overline{\Omega} \backslash \Omega, \end{cases} \quad v_{j,k+\frac{1}{2}} = \begin{cases} v_{j,k}, & \text{if } I_{j,k+1} \in \overline{\Omega} \backslash \Omega, \\ v_{j,k+1}, & \text{if } I_{j,k} \in \overline{\Omega} \backslash \Omega. \end{cases} \qquad (3.33)$$

At regular cell interface, the point values $c_{j+\frac{1}{2},k}$ and $c_{j,k+\frac{1}{2}}$ can be computed in an upwind manner:

$$c_{j+\frac{1}{2},k} = \begin{cases} c_{j,k}^{\text{E}}, & \text{if } u_{j+\frac{1}{2},k} > 0, \\ c_{j+1,k}^{\text{W}}, & \text{otherwise,} \end{cases} \quad c_{j,k+\frac{1}{2}} = \begin{cases} c_{j,k}^{\text{N}}, & \text{if } v_{j,k+\frac{1}{2}} > 0, \\ c_{j,k+1}^{\text{S}}, & \text{otherwise.} \end{cases} \qquad (3.34)$$

In Eq. 3.34, the one-sided point values at cell interface $c_{j,k}^{\text{E,W,NS}}$ are calculated using a second-order piecewise linear reconstruction:

$$\widetilde{c}(x,y) = \overline{c}_{j,k} + (c_x)_{j,k}(x - x_j) + (c_y)_{j,k}(y - y_k), \quad (x,y) \in I_{j,k}, \qquad (3.35)$$

as follows:

$$\begin{aligned} c_{j,k}^{\text{E}} &= \widetilde{c}(x_{j+\frac{1}{2}} - 0, y_k) = \overline{c}_{j,k} + \frac{\Delta x}{2}(c_x)_{j,k}, \ c_{j,k}^{\text{W}} = \widetilde{c}(x_{j-\frac{1}{2}} + 0, y_k) = \overline{c}_{j,k} - \frac{\Delta x}{2}(c_x)_{j,k}, \\ c_{j,k}^{\text{N}} &= \widetilde{c}(x_j, y_{k+\frac{1}{2}} - 0) = \overline{c}_{j,k} + \frac{\Delta y}{2}(c_y)_{j,k}, \ c_{j,k}^{\text{S}} = \widetilde{c}(x_j, y_{k-\frac{1}{2}} + 0) = \overline{c}_{j,k} - \frac{\Delta y}{2}(c_y)_{j,k}. \end{aligned} \qquad (3.36)$$

65

In order to guarantee that the point values computed by Eq. 3.36 have second-order accuracy and nonnegative, we numerically calculate the slopes in Eq. 3.35 adaptively using:

$$
\begin{aligned}
(c_x)_{j,k} &=
\begin{cases}
\dfrac{\overline{c}_{j+1,k}-\overline{c}_{j-1,k}}{2\Delta x}, & \text{if } \overline{c}_{j,k} \pm \dfrac{\Delta x}{2}\cdot\dfrac{\overline{c}_{j+1,k}-\overline{c}_{j-1,k}}{2\Delta x} = \overline{c}_{j,k} \pm \dfrac{\overline{c}_{j+1,k}-\overline{c}_{j-1,k}}{4} \geq 0, \\[2ex]
\mathrm{minmod}\Big(2\dfrac{\overline{c}_{j+1,k}-\overline{c}_{j,k}}{\Delta x},\ \dfrac{\overline{c}_{j+1,k}-\overline{c}_{j-1,k}}{2\Delta x},\ 2\dfrac{\overline{c}_{j,k}-\overline{c}_{j-1,k}}{\Delta x}\Big), & \text{otherwise,}
\end{cases} \\[4ex]
(c_y)_{j,k} &=
\begin{cases}
\dfrac{\overline{c}_{j,k+1}-\overline{c}_{j,k-1}}{2\Delta y}, & \text{if } \overline{c}_{j,k} \pm \dfrac{\Delta y}{2}\cdot\dfrac{\overline{c}_{j,k+1}-\overline{c}_{j,k-1}}{2\Delta y} = \overline{c}_{j,k} \pm \dfrac{\overline{c}_{j,k+1}-\overline{c}_{j,k-1}}{4} \geq 0, \\[2ex]
\mathrm{minmod}\Big(2\dfrac{\overline{c}_{j,k+1}-\overline{c}_{j,k}}{\Delta y},\ \dfrac{\overline{c}_{j,k+1}-\overline{c}_{j,k-1}}{2\Delta y},\ 2\dfrac{\overline{c}_{j,k}-\overline{c}_{j,k-1}}{\Delta y}\Big), & \text{otherwise.}
\end{cases}
\end{aligned}
\tag{3.37}
$$

While for irregular cell interface, similar to the velocities, we easily approximate the point values $c_{j+\frac{1}{2},k}$ and $c_{j,k+\frac{1}{2}}$ as following:

$$
c_{j+\frac{1}{2},k} =
\begin{cases}
c_{j,k}^{\mathrm{E}}, & \text{if } I_{j+1,k}\in\overline{\Omega}\backslash\Omega, \\[1.5ex]
c_{j+1,k}^{\mathrm{W}} & \text{if } I_{j,k}\in\overline{\Omega}\backslash\Omega,
\end{cases}
\qquad
c_{j,k+\frac{1}{2}} =
\begin{cases}
c_{j,k}^{\mathrm{N}} & \text{if } I_{j,k+1}\in\overline{\Omega}\backslash\Omega, \\[1.5ex]
c_{j,k+1}^{\mathrm{S}} & \text{if } I_{j,k}\in\overline{\Omega}\backslash\Omega.
\end{cases}
\tag{3.38}
$$

3.2.3 Finite-volume upwind scheme for the bacteria concentration equation

In this section, we introduce the second-order finite-volume scheme corresponding to the bacteria concentration equation Eq. 3.8. The discrete finite-volume upwind scheme for Eq. 3.19 and Eq. 3.20 can be written in the following form:

$$
\Delta_{j,k}\overline{\rho}^{m+1} - \frac{1}{\Delta t}\overline{\rho}_{j,k}^{m+1} =
\begin{cases}
\dfrac{\mathscr{F}^{x}_{j+\frac{1}{2},k} - \mathscr{F}^{x}_{j-\frac{1}{2},k}}{\Delta x} + \dfrac{\mathscr{F}^{y}_{j,k+\frac{1}{2}} - \mathscr{F}^{y}_{j,k-\frac{1}{2}}}{\Delta y} - \dfrac{1}{\Delta t}\overline{\rho}_{j,k}^{m}, & \mathbf{x}\in\Omega, \\[3ex]
-\dfrac{1}{\Delta t}\overline{\rho}_{j,k}^{m}, & \mathbf{x}\in\overline{\Omega}\backslash\Omega,
\end{cases}
\tag{3.39}
$$

with jump conditions

$$[\rho]_{\partial\Omega_{top}} = 0, \quad \left[\frac{\partial\rho}{\partial\mathbf{n}}\right]_{\partial\Omega_{top}} = \mathbf{q}_\rho^{m+1}, \tag{3.40}$$

where the cell averages of the bacterial concentration, $\overline{\rho}_{j,k}(t) = \frac{1}{\Delta x \Delta y} \int\int_{I_{j,k}} \rho(x,y,t) dx dy$, is the evolved quantity, $\mathcal{F}_{j+\frac{1}{2},k}^x$ and $\mathcal{F}_{j,k+\frac{1}{2}}^y$ are the numerical fluxes of ρ in the x- and y-direction, respectively, and $\mathbf{q}_\rho^{m+1}$ is the augmented variable defined along $\partial\Omega_{top}$ which can be properly computed by the IIM and augmented method (see §1.4). The numerical fluxes $\mathcal{F}_{j+\frac{1}{2},k}^x$ and $\mathcal{F}_{j,k+\frac{1}{2}}^y$ are computed as following:

$$\mathcal{F}_{j+\frac{1}{2},k}^x = [u_{j+\frac{1}{2},k} + \alpha r(c_{j+\frac{1}{2},k})(c_x)_{j+\frac{1}{2},k}]\rho_{j+\frac{1}{2},k}, \quad \mathcal{F}_{j,k+\frac{1}{2}}^y = [v_{j,k+\frac{1}{2}} + \alpha r(c_{j,k+\frac{1}{2}})(c_y)_{j,k+\frac{1}{2}}]\rho_{j,k+\frac{1}{2}}, \tag{3.41}$$

The velocities $u_{j+\frac{1}{2},k}$ and $v_{j,k+\frac{1}{2}}$ are computed using Eq. 3.32 and Eq. 3.33, which is exactly the same as what we do for the oxygen concentration equation. For regular cell interfaces, we calculate the point values of the oxygen concentration $c_{j+\frac{1}{2},k}$ and $c_{j,k+\frac{1}{2}}$ in Eq. 3.41 as follows:

$$c_{j+\frac{1}{2},k} = \frac{c_{j,k}^E + c_{j,k+1}^W}{2}, \quad c_{j,k+\frac{1}{2}} = \frac{c_{j,k}^N + c_{j,k+1}^S}{2}, \tag{3.42}$$

while for the irregular cell interfaces, these point values are computed as:

$$c_{j+\frac{1}{2},k} = \begin{cases} c_{j,k}^E, & \text{if } I_{j+1,k} \in \overline{\Omega}\backslash\Omega, \\ c_{j+1,k}^W, & \text{if } I_{j,k} \in \overline{\Omega}\backslash\Omega, \end{cases} \quad c_{j,k+\frac{1}{2}} = \begin{cases} c_{j,k}^N, & \text{if } I_{j,k+1} \in \overline{\Omega}\backslash\Omega, \\ c_{j,k+1}^S, & \text{if } I_{j,k} \in \overline{\Omega}\backslash\Omega. \end{cases} \tag{3.43}$$

At regular cell interfaces, the derivatives of oxygen concentration $(c_x)_{j+\frac{1}{2},k}$ and $(c_y)_{j,k+\frac{1}{2}}$ are approximated using central difference:

$$(c_x)_{j+\frac{1}{2},k} = \frac{\overline{c}_{j+1,k} - \overline{c}_{j,k}}{\Delta x}, \quad (c_y)_{j,k+\frac{1}{2}} = \frac{\overline{c}_{j,k+1} - \overline{c}_{j,k}}{\Delta y}, \tag{3.44}$$

while at irregular cell interfaces, we approximate $(c_x)_{j+\frac{1}{2},k}$ and $(c_y)_{j,k+\frac{1}{2}}$ as

$$(c_x)_{j+\frac{1}{2},k} = \begin{cases} \dfrac{\overline{c}_{j,k}-\overline{c}_{j-1,k}}{\Delta x}, & \text{if } I_{j+1,k} \in \overline{\Omega}\backslash\Omega, \\[3mm] \dfrac{\overline{c}_{j+2,k}-\overline{c}_{j+1,k}}{\Delta x}, & \text{if } I_{j,k} \in \overline{\Omega}\backslash\Omega, \end{cases} \qquad c_{j,k+\frac{1}{2}} = \begin{cases} \dfrac{\overline{c}_{j,k}-\overline{c}_{j,k-1}}{\Delta y}, & \text{if } I_{j,k+1} \in \overline{\Omega}\backslash\Omega, \\[3mm] \dfrac{\overline{c}_{j,k+2}-\overline{c}_{j,k+1}}{\Delta y}, & \text{if } I_{j,k} \in \overline{\Omega}\backslash\Omega. \end{cases}$$

$$(3.45)$$

The point values of the bacteria concentration at cell interfaces, $\rho_{j+\frac{1}{2},k}$ and $\rho_{j,k+\frac{1}{2}}$, are approximated by the same method which is applied to approximate the oxygen concentration. At regular cell interfaces the point values $\rho_{j+\frac{1}{2},k}$ and $\rho_{j,k+\frac{1}{2}}$ are approximated in an upwind manner:

$$\rho_{j+\frac{1}{2},k} = \begin{cases} \rho_{j,k}^{\mathrm{E}}, & \text{if } u_{j+\frac{1}{2},k} + \alpha r(c_{j+\frac{1}{2},k})(c_x)_{j+\frac{1}{2},k} > 0, \\[3mm] \rho_{j+1,k}^{\mathrm{W}}, & \text{otherwise}, \end{cases}$$

$$\rho_{j,k+\frac{1}{2}} = \begin{cases} \rho_{j,k}^{\mathrm{N}}, & \text{if } v_{j,k+\frac{1}{2}} + \alpha r(c_{j,k+\frac{1}{2}})(c_y)_{j,k+\frac{1}{2}} > 0, \\[3mm] \rho_{j,k+1}^{\mathrm{S}}, & \text{otherwise}. \end{cases}$$

$$(3.46)$$

In Eq. 3.46, the one-sided point values at cell interface $\rho_{j,k}^{\mathrm{E,W,N,S}}$ are calculated using a second-order piecewise linear reconstruction

$$\widetilde{\rho}(x,y) = \overline{\rho}_{j,k} + (\rho_x)_{j,k}(x-x_j) + (\rho_y)_{j,k}(y-y_k), \quad (x,y) \in I_{j,k},$$

$$(3.47)$$

as follows:

$$\rho_{j,k}^{\mathrm{E}} = \widetilde{\rho}(x_{j+\frac{1}{2}}-0,y_k) = \overline{\rho}_{j,k} + \frac{\Delta x}{2}(\rho_x)_{j,k}, \quad \rho_{j,k}^{\mathrm{W}} = \widetilde{\rho}(x_{j-\frac{1}{2}}+0,y_k) = \overline{\rho}_{j,k} - \frac{\Delta x}{2}(\rho_x)_{j,k},$$

$$\rho_{j,k}^{\mathrm{N}} = \widetilde{\rho}(x_j,y_{k+\frac{1}{2}}-0) = \overline{\rho}_{j,k} + \frac{\Delta y}{2}(\rho_y)_{j,k}, \quad \rho_{j,k}^{\mathrm{S}} = \widetilde{\rho}(x_j,y_{k-\frac{1}{2}}+0) = \overline{\rho}_{j,k} - \frac{\Delta y}{2}(\rho_y)_{j,k},$$

$$(3.48)$$

To guarantee that the point values computed by Eq. 3.48 have second-order accuracy and nonnegative, we numerically calculate the slopes in Eq. 3.47 adaptively using:

$$(\rho_x)_{j,k} = \begin{cases} \dfrac{\overline{\rho}_{j+1,k}-\overline{\rho}_{j-1,k}}{2\Delta x}, & \text{if } \overline{\rho}_{j,k} \pm \dfrac{\Delta x}{2}\cdot\dfrac{\overline{\rho}_{j+1,k}-\overline{\rho}_{j-1,k}}{2\Delta x} = \overline{\rho}_{j,k} \pm \dfrac{\overline{\rho}_{j+1,k}-\overline{\rho}_{j-1,k}}{4} \geq 0, \\ \text{minmod}\left(2\dfrac{\overline{\rho}_{j+1,k}-\overline{\rho}_{j,k}}{\Delta x}, \dfrac{\overline{\rho}_{j+1,k}-\overline{\rho}_{j-1,k}}{2\Delta x}, 2\dfrac{\overline{\rho}_{j,k}-\overline{\rho}_{j-1,k}}{\Delta x}\right), & \text{otherwise}, \end{cases}$$

$$(\rho_y)_{j,k} = \begin{cases} \dfrac{\overline{\rho}_{j,k+1}-\overline{\rho}_{j,k-1}}{2\Delta y}, & \text{if } \overline{\rho}_{j,k} \pm \dfrac{\Delta y}{2}\cdot\dfrac{\overline{\rho}_{j,k+1}-\overline{\rho}_{j,k-1}}{2\Delta y} = \overline{\rho}_{j,k} \pm \dfrac{\overline{\rho}_{j,k+1}-\overline{\rho}_{j,k-1}}{4} \geq 0, \\ \text{minmod}\left(2\dfrac{\overline{\rho}_{j,k+1}-\overline{\rho}_{j,k}}{\Delta y}, \dfrac{\overline{\rho}_{j,k+1}-\overline{\rho}_{j,k-1}}{2\Delta y}, 2\dfrac{\overline{\rho}_{j,k}-\overline{\rho}_{j,k-1}}{\Delta y}\right), & \text{otherwise}, \end{cases}$$

$$(3.49)$$

While for irregular cell interface, we approximate the point values $\rho_{j+\frac{1}{2},k}$ and $\rho_{j,k+\frac{1}{2}}$ as following:

$$\rho_{j+\frac{1}{2},k} = \begin{cases} \rho_{j,k}^{\text{E}}, & \text{if } I_{j+1,k} \in \overline{\Omega}\backslash\Omega, \\ \rho_{j+1,k}^{\text{W}} & \text{if } I_{j,k} \in \overline{\Omega}\backslash\Omega, \end{cases} \qquad \rho_{j,k+\frac{1}{2}} = \begin{cases} \rho_{j,k}^{\text{N}} & \text{if } I_{j,k+1} \in \overline{\Omega}\backslash\Omega, \\ \rho_{j,k+1}^{\text{S}} & \text{if } I_{j,k} \in \overline{\Omega}\backslash\Omega. \end{cases} \qquad (3.50)$$

3.3   Numerical example

In this section, we test the developed numerical scheme on some numerical examples. We first design two test cases to test that our numerical scheme presents a correct numerical solution, and performed a mesh refinement test to obtain the accuracy order. Then we would apply the developed numerical scheme on an experimental example.

Example 1—Test Function Defined on a Half Circle

In the first example, we designed test functions defined on a half unit circle domain, $\Omega = \{(x, y) \mid x^2 + y^2 \leq 1, \ y \geq 0\}$, and we set up the test functions u, v, p, c and ρ as following:

$$
\begin{cases}
u(x, y, t) = y(x^2 + y^2 - 1)(1 + t), \\
v(x, y, t) = -x(x^2 + y^2 - 1)(1 + t), \\
p(x, y, t) = 1 + t, \\
c(x, y, t) = 1 - y^2(x^2 + y^2 - 1)(1 + t), \\
\rho(x, y, t) = (x^2 + y^2)(1 + t).
\end{cases} \tag{3.51}
$$

These test functions are solutions for the following modified chemotaxis-fluid system:

$$
\begin{cases}
\rho_t + \left[(u + \alpha r(c)c_x)\rho\right]_x + \left[(v + \alpha r(c)c_y)\rho\right]_y = \Delta\rho + S_\rho, \\
c_t + (uc)_x + (vc)_y = \delta\Delta c - \beta r(c)\rho + S_c, \\
u_t + u u_x + v u_y + \mathbf{Sc}p_x = \mathbf{Sc}\Delta u + S_u, \qquad (x, y) \in \Omega, \ t \geq 0. \\
v_t + u v_x + v v_y + \mathbf{Sc}p_y = \mathbf{Sc}\Delta v - \mathbf{Sc}\gamma\rho + S_v, \\
u_x + v_y = 0,
\end{cases} \tag{3.52}
$$

These source terms S_u, S_v, S_c and S_ρ corresponding to u, v, c and ρ, respectively, are computed by plugging Eq. 3.51 into the chemotaxis-fluid system Eq. 3.6:

$$
\begin{aligned}
S_u &= y(x^2 + y^2 - 1) - x(x^2 + y^2 - 1)^2(1 + t)^2 - 8\mathbf{Sc}y(1 + t), \\
S_v &= -x(x^2 + y^2 - 1) - y(x^2 + y^2 - 1)^2(1 + t)^2 - 8\mathbf{Sc}x(1 + t) + \mathbf{Sc}\gamma\rho, \\
S_c &= -y^2(x^2 + y^2 - 1) + 2x y(x^2 + y^2 - 1)^2(1 + t)^2 - \delta(2x^2 + 14y^2 - 2)(1 + t), \\
S_\rho &= (x^2 + y^2) - 4(1 + t) - (1 + t)^2(24x^2 y^2 + 22y^4 - 6y^2 + 2x^4 - 2x^2).
\end{aligned} \tag{3.53}
$$

70

In order to apply the IIM scheme, as described in previous section §1.4, we embed the half circle domain into a rectangular $\overline{\Omega} = [-1.5, 1.5] \times [0, 1.5]$, and choose proper function values in the region outside the half circle $\overline{\Omega} \backslash \Omega$ to make our test function to be continuous across the boundary $\partial \Omega$. The the extended test functions defined on the domain $\overline{\Omega}$ are as following:

$$
\begin{aligned}
u(x, y, t) &= \begin{cases} y(x^2 + y^2 - 1)(1 + t), & \text{if } x^2 + y^2 < 1, \\ 0, & \text{otherwise.} \end{cases} \\
v(x, y, t) &= \begin{cases} -x(x^2 + y^2 - 1)(1 + t), & \text{if } x^2 + y^2 < 1, \\ 0, & \text{otherwise.} \end{cases} \\
c(x, y, t) &= \begin{cases} 1 - y^2(x^2 + y^2 - 1)(1 + t), & \text{if } x^2 + y^2 < 1, \\ 1, & \text{otherwise.} \end{cases} \\
\rho(x, y, t) &= \begin{cases} (x^2 + y^2)(1 + t), & \text{if } x^2 + y^2 < 1, \\ 1 + t, & \text{otherwise.} \end{cases}
\end{aligned}
\tag{3.54}
$$

We first implement the proposed numerical scheme on a uniform mesh with $\Delta x = \Delta y = 3/128$ at time $t = 0.05$, the solutions are plotted in figure Fig. 3.1 and Fig. 3.2. As one can see, the obtained solutions can preserve the positivity and match with the exact solutions pretty well.

Next, we conduct the accuracy test at a small time, in order to measure the convergence rate, we perform a mesh refine test and compare the obtained results with the exact solutions. The results are presented in Table 3.1
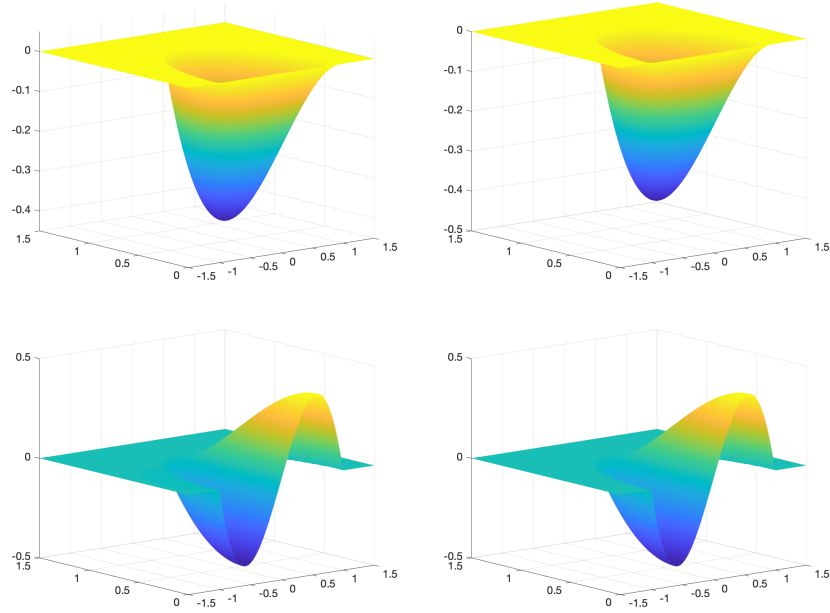
71

Figure 3.1: Example 1: velocities u (top row) and v (bottom row) computed by proposed numerical scheme (left column) on a uniform mesh with $\Delta x = \Delta y = 3/128$ compare with the exact values of the test case (right column) at time $t = 5 \times 10^{-2}$.

Table 3.1: Example 1: L^∞-errors for u, v, c and ρ computed by the proposed scheme.

grid	u-error	rate	v-error	rate	c-error	rate	ρ-error	rate
64×32	1.25E-3		2.08E-3		2.76E-4		4.23E-2	
128×64	5.15E-4	1.28	5.40E-4	1.95	6.92E-5	2.00	2.59E-2	0.71
256×128	1.69E-4	1.61	1.39E-4	1.96	1.79E-5	1.95	1.39E-2	0.90
512×256	5.71E-5	1.57	3.49E-5	1.99	4.78E-6	1.90	7.51E-3	0.89

Example 2—Test Function Without Given Pressure p

Normally in practice, the given initial conditions for the IBVP Eq. 3.6 will only have the value of velocity filed u and v, and the densities c and ρ at time $t = 0$. We need to solve the Pressure Poisson Equation (PPE) corresponding to the incompressible NS equation with some proper chosen boundary conditions to get the pressure information p. While the projection method we applied to evolve the NS equation does not require an exact initial
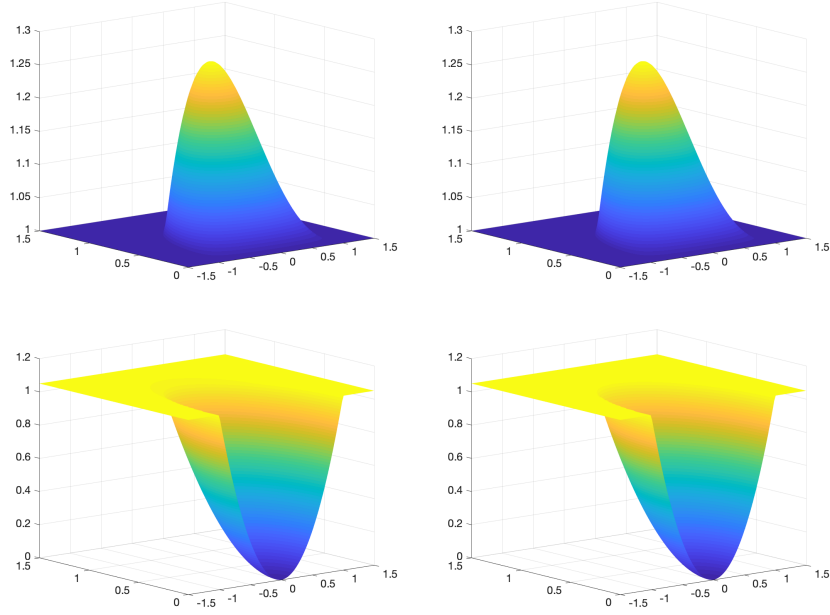
Figure 3.2: Example 1: c (top row) and ρ (bottom row) computed by proposed numerical scheme (left column) on a uniform mesh with $\Delta x = \Delta y = 3/128$ compare with the exact values of the test case (right column) at time $t = 5 \times 10^{-2}$.

value for p, even if we input a initial guess for p at beginning, the solution u and v we obtained for small time t may have some oscillation, but as time goes on, when t becomes larger, that oscillation will be smoothed out and give us a good numerical solution. In order to test this property, we design the following test functions defined in the half unit circle

domain, and investigate the solutions with different input p at different times.

$$u(x, y, t) = \frac{y}{4}t,$$

$$v(x, y, t) = -\frac{x}{4}(1 - x^2)t,$$

$$p(x, y, t) = (-\frac{3}{4}x^3 + \frac{3}{8}x)y, \qquad (3.55)$$

$$c(x, y, t) = 1 + (x^2 + y^2 - 1)t,$$

$$\rho(x, y, t) = (x^2 + y^2)t.$$

Same as in the previous Example 1, we embed the half unit circle domain Ω into the rectangular domain $\overline{\overline{\Omega}} = [-1.5, 1.5] \times [0, 1.5]$, and extend the test functions to $\overline{\overline{\Omega}}$:

$$u(x, y, t) = \begin{cases} \dfrac{y}{4}t, & \text{if } x^2 + y^2 < 1, \\ \dfrac{y}{4}(x^2 + y^2)t, & \text{otherwise.} \end{cases}$$

$$v(x, y, t) = \begin{cases} -\dfrac{x}{4}(1 - x^2)t, & \text{if } x^2 + y^2 < 1, \\ -\dfrac{x\,y^2}{4}t, & \text{otherwise.} \end{cases}$$

$$p(x, y, t) = \begin{cases} (-\dfrac{3}{4}x^3 + \dfrac{3}{8}x)y, & \text{if } x^2 + y^2 < 1, \\ 0, & \text{otherwise.} \end{cases} \qquad (3.56)$$

$$c(x, y, t) = \begin{cases} 1 + (x^2 + y^2 - 1)t, & \text{if } x^2 + y^2 < 1, \\ 1, & \text{otherwise.} \end{cases}$$

$$\rho(x, y, t) = \begin{cases} (x^2 + y^2)t, & \text{if } x^2 + y^2 < 1, \\ t, & \text{otherwise.} \end{cases}$$

We compute the source terms S_u, S_v, S_c and S_ρ corresponding to our test functions 3.56

74

and the IBVP Eq. 3.6, Eq. 3.7:

$$
S_u(x,y,t) = \begin{cases} \dfrac{y}{4} - \dfrac{x(1-x^2)}{16}t^2 + \mathbf{Sc}(-\dfrac{9}{4}x^2 + \dfrac{3}{8})y, & \text{if } x^2 + y^2 < 1, \\[2ex] \dfrac{(x^2+y^2)}{4}y - 2\mathbf{Sc}\,y\,t, & \text{otherwise.} \end{cases}
$$

$$
S_v(x,y,t) = \begin{cases} -\dfrac{x}{4}(1-x^2) + \dfrac{y(3x^2-1)}{16}t + \mathbf{Sc}(-\dfrac{3}{4}x^3 + \dfrac{3}{8}x) - \mathbf{Sc}\dfrac{3}{2}x\,t, & \text{if } x^2 + y^2 < 1, \\[2ex] -\dfrac{x\,y^2}{4} + \mathbf{Sc}\dfrac{x}{2}t, & \text{otherwise.} \end{cases}
$$

$$
S_c(x,y,t) = \begin{cases} (x^2 + y^2 - 1) + \dfrac{x^3 y}{2}t^2 - 4\delta t, & \text{if } x^2 + y^2 < 1, \\[2ex] 0, & \text{otherwise.} \end{cases}
$$

$$
S_\rho(x,y,t) = \begin{cases} (x^2 + y^2) + (8x^2 + 8y^2 + \dfrac{x^3 y}{2})t^2 - 4t, & \text{if } x^2 + y^2 < 1, \\[2ex] 1, & \text{otherwise.} \end{cases}
$$

$$\tag{3.57}$$

We first implement the scheme on a uniform mesh with $\Delta x = \Delta y = 3/128$, and evaluate the system at a small time $t = 1.37 \times 10^{-3}$ using the exact initial values of pressure p. The solutions are shown in figure Fig. 3.3 and Fig. 3.4, and we can observe that the numerical solutions agree with the exact solutions.

We next implement the numerical scheme on the same mesh, but with initial condition $p = 0$, and plot the solutions in figure Fig. 3.5. We can clearly observe some oscillation in the numerical solution for u and v, so they do not match with our test case plotted in Fig. 3.3. While we keep the same initial setting and evaluate the numerical solutions at a later time $t = 5 \times 10^{-2}$, plotting the solutions in figure Fig. 3.6 and Fig. 3.7, we can observe that the oscillation has been smoothed out and the obtained numerical solutions converge to the exact solutions.
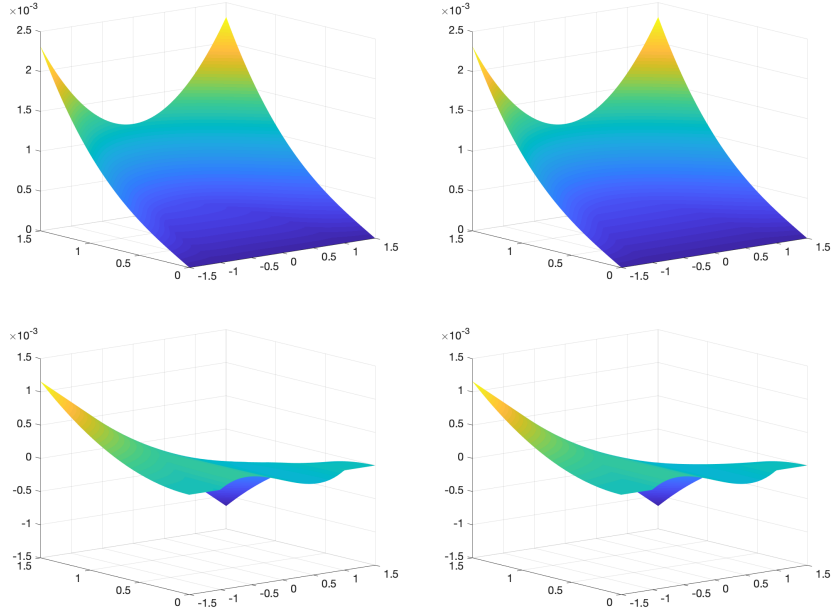
Figure 3.3:   Example 2: velocities u (top row) and v (bottom row) computed by proposed numerical scheme (left column) on a uniform mesh with $\Delta x = \Delta y = 3/128$ compare with the exact values of the test case (right column) at time $t = 1.37 \times 10^{-3}$.

Example 3—Chemotaxis-Fluid system With Experimental Data

In this example taken from (21), we investigate the chemotaxis-fluid system Eq. 3.6 with

$$\alpha = 10, \quad \beta = 100, \quad \delta = 5, \quad \gamma = 10000 \quad \text{and} \quad \mathbf{Sc} = 500, \tag{3.58}$$

in a flat drop-like domain, which can be described as a half ellipse:

$$\Omega = \{(x, y) \mid \frac{x^2}{64} + y^2 \leq \frac{1}{4}, \ y \geq 0\}. \tag{3.59}$$
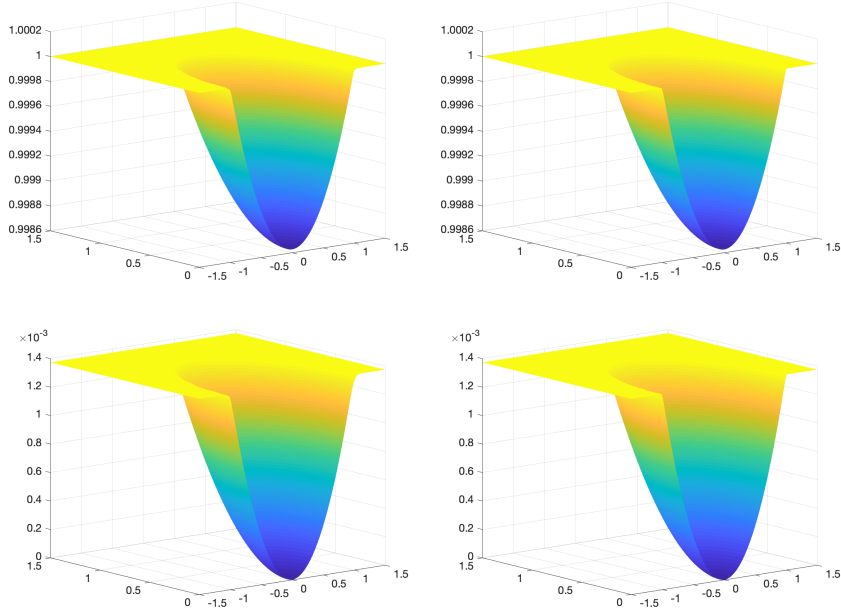
Figure 3.4: Example 2: c (top row) and ρ (bottom row) computed by proposed numerical scheme (left column) on a uniform mesh with $\Delta x = \Delta y = 3/128$ compare with the exact values of the test case (right column) at time $t = 1.37 \times 10^{-3}$.

and subject to the initial data:

$$u = 0, \quad v = 0, \quad c = 1,$$

$$\rho = \begin{cases} 0.5, & \text{if } y < \sqrt{0.35^2 - (\dfrac{x}{8})^2} - 0.01 \cos(2\pi x), \\ 1, & \text{otherwise.} \end{cases} \tag{3.60}$$

In practice, we found that the the non-linear chemotaxis term in bacteria equation, the large parameter γ and schmidt number **Sc** will lead to some stability issue close to the curve boundary, the numerical solution obtained by our proposed finite-volume upwind scheme will blow-up at the center of the top boundary. So practically in this example, we applied a particle method to evolve the bacteria equation. We embed the half ellipse domain Ω into
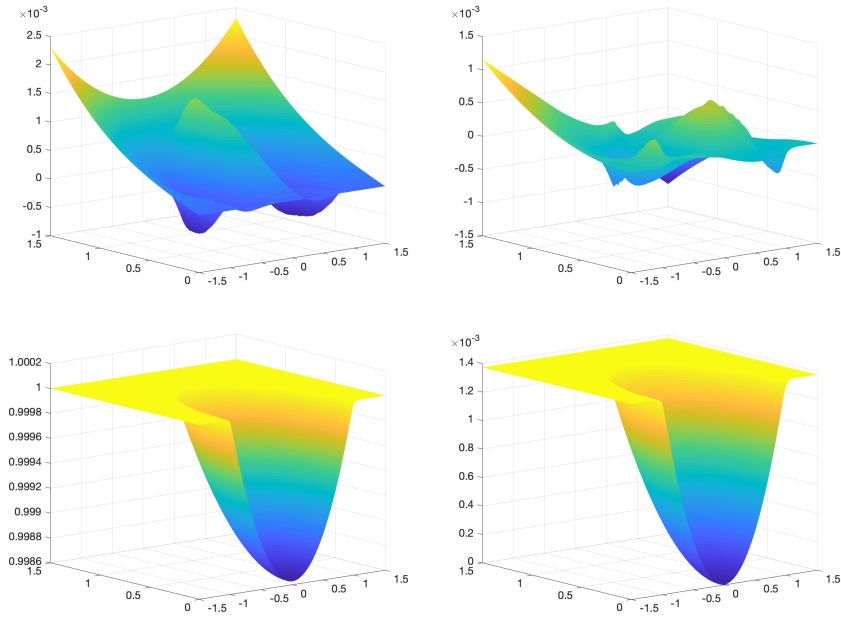
Figure 3.5: Example 2: velocities u (top-left), v (top-right), c (bottom-left) and ρ (bottom-right) computed by proposed numerical scheme on a uniform mesh with $\Delta x = \Delta y = 3/128$ at time $t = 1.37 \times 10^{-3}$.

a rectangular domain $\bar{\Omega} = [-5, 5] \times [0, 1]$, implement the numerical scheme on a uniform mesh $\Delta x = \frac{10}{201}$ and $\Delta y = \frac{1}{40}$, and compute the solutions at different times. The bacteria concentration ρ, the oxygen concentration c and the velocity field (u, v) computed at a small time $t = 1.2 \times 10^{-3}$ are presented in figure Fig. 3.8. We can observe that the bacteria are moving toward the top boundary and form a higher concentration layer near the top boundary, and in this layer, the oxygen consumption is larger due to the higher bacteria concentration, so we have smaller oxygen concentration value c corresponding to this layer.

We also computed the solutions for later time $t = 8 \times 10^{-3}$, and plot the solutions in figure Fig. 3.9, we can observe that as time goes on, the oxygen concentration c will become smaller and gravity start to be dominant, so the bacteria will fall down and form a high
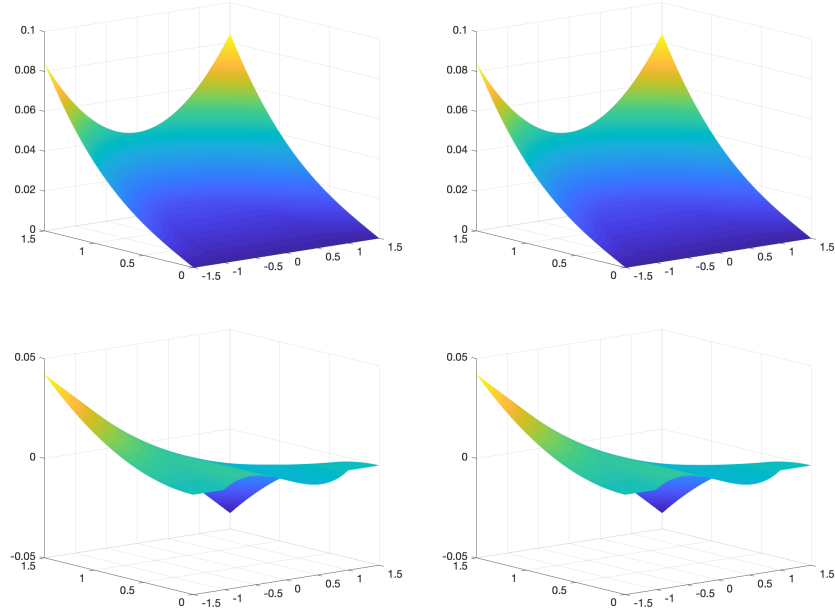
Figure 3.6: Example 2: velocities u (top row) and v (bottom row) computed by proposed numerical scheme (left column) on a uniform mesh with $\Delta x = \Delta y = 3/128$ compare with the exact values of the test case (right column) at time $t = 5 \times 10^{-2}$.

concentration part close to the corner, and the large oxygen consumption in this region leads to a low oxygen concentration c until it reaches the threshold value $c_{crit} = 0.3$ which the bacteria will become inactive.

Some physical experiments suggest that in some case, the bacteria will swim toward the top boundary and form a high concentration layer, but instead of falling down along the boundary, the bacteria may sink downward at the middle and present some finger like plumes. In our numerical experiment, we did not get a numerical solution which can simulate this process. However, the chemotaxis-fluid system is complicated, and pretty sensitive to the shape of top curve boundary and the parameters. Thus, one needs to work with scientist in biology and modeling to investigate a proper shape of domain and corresponding parameters, and perform more experiment to capture these phenomena.

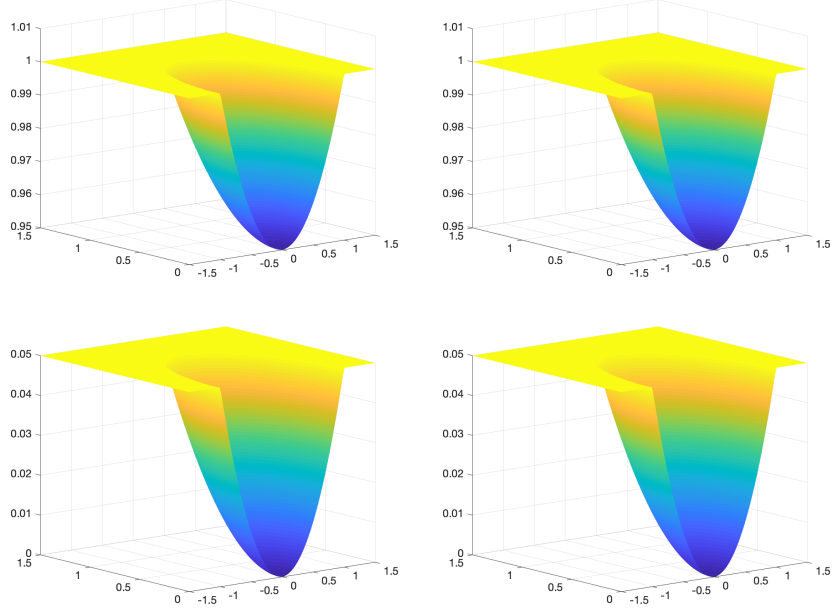Figure 3.7: Example 2: c (top row) and ρ (bottom row) computed by proposed numerical scheme (left column) on a uniform mesh with $\Delta x = \Delta y = 3/128$ compare with the exact values of the test case (right column) at time $t = 5 \times 10^{-2}$.

Figure 3.8: Example 3: velocity field (u, v) (top), oxygen concentration c (mid) and bacteria concentration ρ (bottom) computed at time $t = 1.2 \times 10^{-3}$.
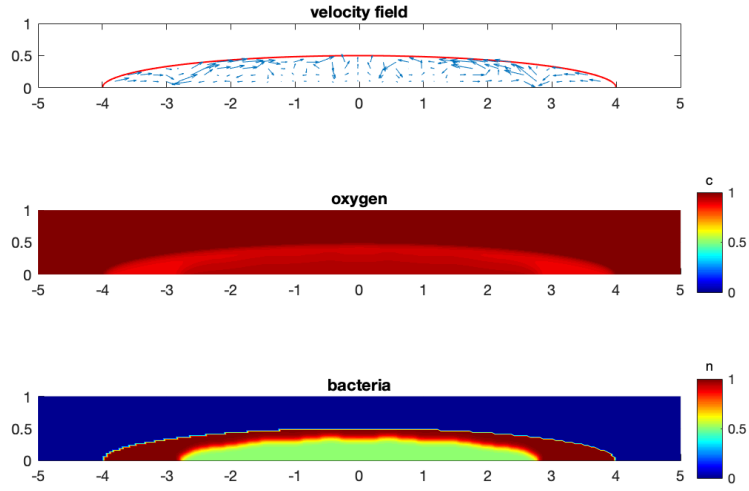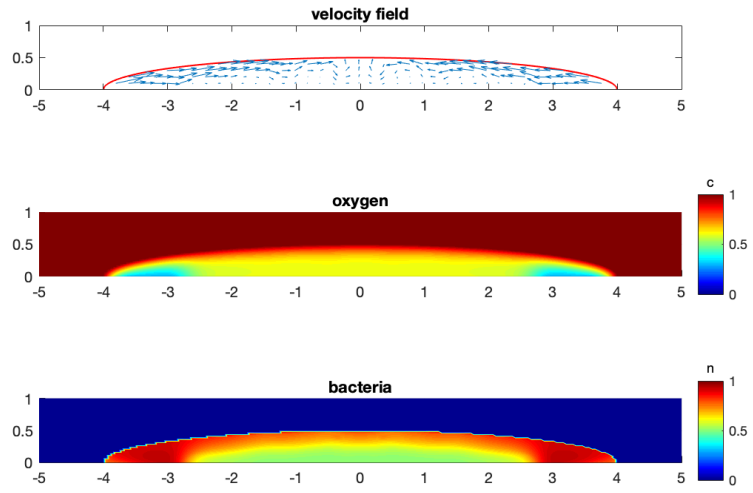
Figure 3.9:   Example 3: velocity field (u, v) (top), oxygen concentration c (mid) and bacteria concentration ρ (bottom) computed at time $t = 8 \times 10^{-3}$.

CHAPTER

4

CONCLUSIONS AND FUTURE WORK

In this thesis, we developed finite-volume-finite-difference schemes for approximating the chemotaxis system and related models. The major contributions of two projects are following:

- First we derived and implemented a second-order and fourth-order hybrid FVFD schemes for chemotaxis equations, and performed 3 numerical experiments to demonstrate that the developed numerical schemes can preserve the positivity of the solutions and capture the blow-up phenomenon of the PKS model. We also extended the developed schemes to the two-species chemotaxis system and investigated the

different types of singularities of each specie for the multi-species system.

- Second, we developed and study a hybrid FVFD scheme for the chemotaxis-fluid system defined on the domain with a curved boundary. In our developed numerical scheme, we applied the immersed interface method and the augmented method to treat the (irregular) grid points near the curved boundary. We presented 2 numerical results for the numerical scheme, demonstrating that the numerical scheme is smooth in the domain with a curved boundary and the numerical solutions converge to the exact solutions. We also performed a numerical experiment to investigate behavior of the bacteria in Bacillus subtilis suspension in a thin chamber.

In the future, we plan to work with scientist in biology and modeling to investigate the chemotaxis-fluid model, figure out proper domains and parameters corresponding to variety of collective phenomenon of the bacteria, and perform more experiment to simulate the bioconvection patterns. More over, we intend to investigate additional numerical approaches and computational techniques to simulate chemotaxis and related phenomenon.

REFERENCES

[1] Adler, A. (1975). Chemotaxis in bacteria. *Ann. Rev. Biochem.*, 44:341–356.

[2] Anderson, C. and Greengard, C. (1985). On vortex methods. *SIAM J. Numer. Anal.*, 22(3):413–440.

[3] Arminjon, P., Viallon, M.-C., and Madrane, A. (1997). A finite volume extension of the lax-friedrichs and nessyahu-tadmor schemes for conservation laws on unstructured grids. *Int. J. Comput. Fluid Dyn.*, 9:1–22.

[4] Ascher, U. M., Ruuth, S. J., and Spiteri, R. J. (1997). Implicit-explicit runge-kutta methods for time-dependent partial differential equations. *Applied Numerical Mathematics*, 25(2-3):151–167.

[5] Ascher, U. M., Ruuth, S. J., and Wetton, B. T. (1995). Implicit-explicit methods for time-dependent partial differential equations. *SIAM Journal on Numerical Analysis*, 32(3):797–823.

[6] Beale, J. T. and Majda, A. (1982a). Vortex methods. I. Convergence in three dimensions. *Math. Comp.*, 39(159):1–27.

[7] Beale, J. T. and Majda, A. (1982b). Vortex methods. II. Higher order accuracy in two and three dimensions. *Math. Comp.*, 39(159):29–52.

[8] Beale, J. T. and Majda, A. (1985). High order accurate vortex methods with explicit velocity kernels. *J. Comput. Phys.*, 58:188–208.

[9] Bell, J. B., Colella, P., and Glaz, H. M. (1989). A second-order projection method for the incompressible navier-stokes equations. *Journal of Computational Physics*, 85(2):257 – 283.

[10] Bianco, F., Puppo, G., and Russo, G. (1999). High order central schemes for hyperbolic systems of conservation laws. *SIAM J. Sci. Comput*, 21:294–322.

[11] Bollermann, A., Noelle, S., and Lukáčová-Medviďová, M. (2011). Finite volume evolution Galerkin methods for the shallow water equations with dry beds. *Commun. Comput. Phys.*, 10(2):371–404.

[12] Bonner, J. T. (1967). *The cellular slime molds*. Princeton University Press, Princeton, New Jersey, 2nd edition.

[13] Bouchut, F. (2004). *Nonlinear stability of finite volume methods for hyperbolic conservation laws and well-balanced schemes for sources*. Frontiers in Mathematics. Birkhäuser Verlag, Basel.

[14] Brown, D. L., Cortez, R., and Minion, M. L. (2001). Accurate projection methods for the incompressible navier–stokes equations. *Journal of Computational Physics,* 168(2):464 – 499.

[15] Bryson, S., Kurganov, A., Levy, D., and Petrova, G. (2005). Semi-discrete central-upwind schemes with reduced dissipation for hamilton-jacobi equations. *IMA J. Numer. Anal.,* 25:113–138.

[16] Bryson, S. and Levy, D. (2003). High-order semi-discrete central-upwind schemes for multi-dimensional Hamilton-Jacobi equations. *J. Comput. Phys.,* 189(1):63–87.

[17] Budrene, E. O. and Berg, H. C. (1991). Complex patterns formed by motile cells of escherichia coli. *Nature,* 349:630–633.

[18] Budrene, E. O. and Berg, H. C. (1995). Dynamics of formation of symmetrical patterns by chemotactic bacteria. *Nature,* 376:49–53.

[19] Calvez, V. and Carrillo, J. A. (2006). Volume effects in the Keller-Segel model: energy estimates preventing blow-up. *J. Math. Pures Appl. (9),* 86(2):155–175.

[20] Chertock, A. (2017). A practical guide to deterministic particle methods. In *Handbook of Numerical Methods for Hyperbolic Problems,* volume 18 of *Handbook of Numerical Analysis,* pages 177–202. Elsevier.

[21] Chertock, A., Fellner, K., Kurganov, A., Lorz, A., and Markowich, P. A. (2012a). Sinking, merging and stationary plumes in a coupled chemotaxis-fluid model: a high-resolution numerical approach. *J. Fluid Mech.,* 694:155–190.

[22] Chertock, A. and Kurganov, A. (2008). A positivity preserving central-upwind scheme for chemotaxis and haptotaxis models. *Numer. Math.,* 111:169–205.

[23] Chertock, A., Kurganov, A., Wang, X., and Wu, Y. (2012b). On a chemotaxis model with saturated chemotactic flux. *Kinet. Relat. Models,* 5(1):51–95.

[24] Childress, S. and Percus, J. K. (1981). Nonlinear aspects of chemotaxis. *Math. Biosc.,* 56:217–237.

[25] Choquin, J. and Huberson, S. (1989). Particles simulation of viscous flow. *Computers & Fluids,* 17(2):397–410.

[26] Chorin, A. J. (1973). Numerical study of slightly viscous flow. *J. Fluid Mech.,* 57(4):785–796.

[27] Chorin, A. J. and Marsden, J. E. (1993). *A mathematical introduction to fluid mechanics,* volume 4 of *Texts in Applied Mathematics.* Springer-Verlag, New York, third edition.

[28] Christov, I. and Popov, B. (2008). New nonoscillatory central schemes on unstructured triangulations for hyperbolic systems of conservation laws. *J. Comput. Phys.*, 227:5736–5757.

[29] Cohen, A. and Perthame, B. (2000). Optimal approximations of transport equations by particle and pseudoparticle methods. *SIAM J. Math. Anal.*, 32(3):616–636.

[30] Cohen, M. H. and Robertson, A. (1971). Wave propagation in the early stages of aggregation of cellular slime molds. *J. Theor. Biol.*, 31:101–118.

[31] Conca, C., Espejo, E., and Vilches, K. (2011). Remarks on the blowup and global existence for a two species chemotactic Keller-Segel system in $\mathbb{R}^2$. *European J. Appl. Math.*, 22(6):553–580.

[32] Constantin, L. A. and Kurganov, A. (2006). Adaptive central-upwind schemes for hyperbolic systems of conservation laws. In *Hyperbolic problems: theory, numerics and applications. I*, pages 95–103. Yokohama Publ., Yokohama.

[33] Cottet, G.-H. and Koumoutsakos, P. D. (2000). *Vortex methods.* Cambridge University Press, Cambridge.

[34] Degond, P. and Mas-Gallic, S. (1989). The weighted particle method for convection-diffusion equations. part 1 and part 2. *Math. Comp.*, 53:485–525.

[35] Degond, P. and Mustieles, F. J. (1990). A deterministic approximation of diffusion equations using particles. *SIAM J. Sci. Stat. Comp.*, 11(2):293–310.

[Di Francesco et al.] Di Francesco, M., Lorz, A., and Markowich, P. Chemotaxis–fluid coupled model for swimming bacteria with nonlinear diffusion: global existence and asymptotic behavior. Preprint.

[Duan et al.] Duan, R.-J., Lorz, A., and Markowich, P. Global solutions to the coupled chemotaxis-fluid equations. Preprint.

[38] Epshteyn, Y. (2012). Upwind-difference potentials method for Patlak-Keller-Segel chemotaxis model. *J. Sci. Comput.*, 53(3):689–713.

[39] Epshteyn, Y. and Izmirlioglu, A. (2009). Fully discrete analysis of a discontinuous finite element method for the Keller-Segel chemotaxis model. *J. Sci. Comput.*, 40(1-3):211–256.

[40] Epshteyn, Y. and Kurganov, A. (2008). New interior penalty discontinuous galerkin methods for the Keller-Segel chemotaxis model. *SIAM J. Numer. Anal.*, 47:386–408.

[41] Espejo, E. E., Stevens, A., and Suzuki, T. (2012). Simultaneous blowup and mass separation during collapse in an interacting system of chemotactic species. *Differential Integral Equations*, 25(3-4):251–288.

[42] Espejo, E. E., Stevens, A., and Velázquez, J. J. L. (2010). A note on non-simultaneous blow-up for a drift-diffusion model. *Differential Integral Equations*, 23(5-6):451–462.

[43] Espejo, E. E., Vilches, K., and Conca, C. (2013). Sharp condition for blow-up and global existence in a two species chemotactic Keller-Segel system in $\mathbb{R}^2$. *European J. Appl. Math.*, 24:297–313.

[44] Espejo Arenas, E. E., Stevens, A., and Velázquez, J. J. L. (2009). Simultaneous finite time blow-up in a two-species model for chemotaxis. *Analysis (Munich)*, 29(3):317–338.

[45] Evans, M. W. and Harlow, F. H. (1957). The particle-in-cell method for hydrodynamic calculations. Technical Report LA-2139, Los Alamos Scientific Laboratory.

[46] Fasano, A., Mancini, A., and Primicerio, M. (2004). Equilibrium of two populations subject to chemotaxis. *Math. Models Methods Appl. Sci.*, 14:503–533.

[47] Filbet, F. (2006). A finite volume scheme for the patlak-keller-segel chemotaxis model. *Numer. Math.*, 104:457–488.

[48] Friedrichs, K. O. (1954). Symmetric hyperbolic linear differential equations. *Comm. Pure Appl. Math.*, 7:345–392.

[49] GHORAI, S. and HILL, N. A. (1999). Development and stability of gyrotactic plumes in bioconvection. *Journal of Fluid Mechanics*, 400:1–31.

[50] Godlewski, E. and Raviart, P.-A. (1996). *Numerical approximation of hyperbolic systems of conservation laws*, volume 118 of *Applied Mathematical Sciences*. Springer-Verlag, New York.

[51] Godunov, S. K. (1959). A difference method for numerical calculation of discontinuous solutions of the equations of hydrodynamics. *Mat. Sb. (N.S.)*, 47 (89):271–306.

[52] Gottlieb, S., Ketcheson, D., and Shu, C.-W. (2011). *Strong stability preserving Runge-Kutta and multistep time discretizations*. World Scientific Publishing Co. Pte. Ltd., Hackensack, NJ.

[53] Gottlieb, S., Shu, C.-W., and Tadmor, E. (2001). Strong stability-preserving high-order time discretization methods. *SIAM Rev.*, 43:89–112.

[54] Hald, O. H. (1991). Convergence of vortex methods. In *Vortex methods and vortex motion*, pages 33–58. SIAM, Philadelphia, PA.

[55] Harlow, F. H. (1964). The particle-in-cell computing method for fluid dynamics. In Alder, B., Fernbach, S., and Rotenberg, M., editors, *Methods in Computational Physics*, volume 3, pages 319–343. Academic Press, New York.

[56] Herrero, M. A. and Velázquez, J. J. L. (1997). A blow-up mechanism for a chemotaxis model. *Ann. Scuola Normale Superiore*, 24:633–683.

[57] Hillen, T. and Painter, K. (2001). Global existence for a parabolic chemotaxis model with prevention of overcrowding. *Adv. in Appl. Math.*, 26(4):280–301.

[58] Hillen, T. and Painter, K. J. (2009). A user's guide to PDE models for chemotaxis. *J. Math. Biol.*, 58(1-2):183–217.

[59] Hillesdon, A. J. and Pedley, T. J. (1996). Bioconvection in suspensions of oxytactic bacteria: linear theory. *J. Fluid Mech.*, 324:223–259.

[60] Hillesdon, A. J., Pedley, T. J., and Kessler, O. (1995). The development of concentration gradients in a suspension of chemotactic bacteria. *Bull. Math. Bio.*, 57(2):299–344.

[61] Hockney, R. W. and Eastwood, J. W. (2010). *Computer Simulation Using Particles*. CRC Press.

[62] Hopkins, M. and Fauci, L. J. (2002). A computational model of the collective fluid dynamics of motile micro-organisms. *J. Fluid Mech.*, 455:149–174.

[63] Horstmann, D. (2003). From 1970 until now: The keller-segel model in chemotaxis and its consequences i. *Jahresber. DMV*, 105:103–165.

[64] Horstmann, D. (2004). From 1970 until now: The keller-segel model in chemotaxis and its consequences ii. *Jahresber. DMV*, 106:51–69.

[65] Hundsdorfer, W. and Verwer, J. G. (2013). *Numerical solution of time-dependent advection-diffusion-reaction equations*, volume 33. Springer Science & Business Media.

[66] Jiang, G.-S. and Tadmor, E. (1998). Nonoscillatory central schemes for multidimensional hyperbolic conservation laws. *SIAM J. Sci. Comput.*, 19(6):1892–1917 (electronic).

[67] Keller, E. F. and Segel, L. A. (1970). Initiation of slime mold aggregation viewed as an instability. *J. Theor. Biol.*, 26:399–415.

[68] Keller, E. F. and Segel, L. A. (1971a). Model for chemotaxis. *J. Theor. Biol.*, 30:225–234.

[69] Keller, E. F. and Segel, L. A. (1971b). Traveling bands of chemotactic bacteria: A theoretical analysis. *J. Theor. Biol.*, 30:235–248.

[70] Kim, J. and Moin, P. (1985). Application of a fractional-step method to incompressible navier-stokes equations. *Journal of Computational Physics*, 59(2):308 – 323.

[71] Kröner, D. (1997). *Numerical schemes for conservation laws*. Wiley-Teubner Series Advances in Numerical Mathematics. John Wiley & Sons Ltd., Chichester.

[72] Kurganov, A. and Levy, D. (2000). Third-order semi-discrete central scheme for conservation laws and convection-diffusion equations. *SIAM J. Sci. Comput.*, 22:1461–1488.

[73] Kurganov, A. and Lin, C.-T. (2007). On the reduction of numerical dissipation in central-upwind schemes. *Commun. Comput. Phys.*, 2:141–163.

[74] Kurganov, A. and Liu, Y. (2012). New adaptive artificial viscosity method for hyperbolic systems of conservation laws. *J. Comput. Phys.*, 231:8114–8132.

[75] Kurganov, A. and Lukáčová-Medviďová, M. (2014). Numerical study of two-species chemotaxis models. *Discrete Contin. Dyn. Syst. Ser. B,* 19:131–152.

[76] Kurganov, A. and Petrova, G. (2000). Central schemes and contact discontinuities. *M2AN Math. Model. Numer. Anal.*, 34(6):1259–1275.

[77] Kurganov, A. and Petrova, G. (2001). A third-order semi-discrete genuinely multidimensional central scheme for hyperbolic conservation laws and related problems. *Numer. Math.*, 88(4):683–729.

[78] Kurganov, A. and Petrova, G. (2005). Central-upwind schemes on triangular grids for hyperbolic systems of conservation laws. *Numer. Methods Partial Differential Equations,* 21:536–552.

[79] Kurganov, A. and Petrova, G. (2006). Adaptive central-upwind schemes for hamilton-jacobi equations with nonconvex hamiltonians. *J. Sci. Comput.*, 27:323–333.

[80] Kurganov, A., Petrova, G., and Popov, B. (2007). Adaptive semi-discrete central-upwind schemes for nonconvex hyperbolic conservation laws. *SIAM J. Sci. Comput.*, 29:2381–2401.

[81] Kurganov, A. and Tadmor, E. (2000a). New high resolution central schemes for nonlinear conservation laws and convection-diffusion equations. *J. Comput. Phys.*, 160:241–282.

[82] Kurganov, A. and Tadmor, E. (2000b). New high-resolution semi-discrete central scheme for hamilton-jacobi equations. *J. Comput. Phys.*, 160:720–742.

[83] Kurokiba, M. and Ogawa, T. (2003). Finite time blow-up of the solution for a nonlinear parabolic equation of drift-diffusion type. *Diff. Integral Eqns,* 4:427–452.

[84] Lax, P. D. (1954). Weak solutions of nonlinear hyperbolic equations and their numerical computation. *Comm. Pure Appl. Math.*, 7:159–193.

[85] LeVeque, R. J. and Li, Z. (1994). The immersed interface method for elliptic equations with discontinuous coefficients and singular sources. *SIAM Journal on Numerical Analysis,* 31(4):1019–1044.

[86] Levy, D., Puppo, G., and Russo, G. (1999). Central WENO schemes for hyperbolic systems of conservation laws. *M2AN Math. Model. Numer. Anal.*, 33(3):547–571.

[87] Li, Z. (1994). *The immersed interface method: A numerical approach for partial differential equations with interfaces.* PhD thesis, University of Washington.

[88] Li, Z. (1998). A fast iterative algorithm for elliptic interface problems. *SIAM Journal on Numerical Analysis*, 35(1):230–254.

[89] Li, Z. (2003). An overview of the immersed interface method and its applications. *Taiwanese journal of mathematics*, 7(1):1–49.

[90] Li, Z. and Ito, K. (2006). *The immersed interface method: numerical solutions of PDEs involving interfaces and irregular domains.* SIAM.

[91] Li, Z., Ji, H., and Chen, X. (2017). Accurate solution and gradient computation for elliptic interface problems with variable coefficients. *SIAM journal on numerical analysis*, 55(2):570–597.

[92] Li, Z., Lai, M.-C., He, G., and Zhao, H. (2010). An augmented method for free boundary problems with moving contact lines. *Computers & Fluids*, 39(6):1033 – 1040.

[93] Lie, K.-A. and Noelle, S. (2003a). An improved quadrature rule for the flux-computation in staggered central difference schemes in multidimensions. *J. Sci. Comput.*, 63:1539–1560.

[94] Lie, K.-A. and Noelle, S. (2003b). On the artificial compression method for second-order nonoscillatory central difference schemes for systems of conservation laws. *SIAM J. Sci. Comput.*, 24(4):1157–1174.

[95] Liotta, S. F., Romano, V., and Russo, G. (2000). Central schemes for balance laws of relaxation type. *SIAM J. Numer. Anal.*, 38:1337–1356.

[96] Liu, J.-G. and Lorz, A. (2011). A coupled chemotaxis-fluid model: Global existence. *Annales de l'I.H.P. Analyse non linéaire*, 28(5):643–652.

[97] Liu, X.-D. and Tadmor, E. (1998). Third order nonoscillatory central scheme for hyperbolic conservation laws. *Numer. Math.*, 79(3):397–425.

[98] Lorz, A. (2010). Coupled chemotaxis fluid model. *Math. Models Methods Appl. Sci.* To appear.

[99] Lu, G. Y. and Wong, D. W. (2008). An adaptive inverse-distance weighting spatial interpolation technique. 34(9):1044–1055.

[100] Marrocco, A. (2003). 2d simulation of chemotaxis bacteria aggregation. *M2AN Math. Model. Numer. Anal.*, 37:617–630.

[101] Mas-Gallic, S. (1987). A deterministic particle method for the linearized boltzmann equation. *Transport Theory and Stat. Phys.*, 16:855–887.

[102] Mas-Gallic, S. and Raviart, P. A. (1986). Particle approximation of convection-diffusion equations. International Report 86013, Université Pierre et Marie Curie.

[103] Metcalfe, A. M. and Pedley, T. J. (1998). Bacterial bioconvection: weakly nonlinear theory for pattern selection. *J. Fluid Mech.*, 370:249–270.

[104] Nanjundiah, V. (1973). Chemotaxis, signal relaying and aggregation morphology. *J. Theor. Biol.*, 42:63–105.

[105] Nessyahu, H. and Tadmor, E. (1990). Nonoscillatory central differencing for hyperbolic conservation laws. *J. Comput. Phys.*, 87(2):408–463.

[106] Nordmark, H. O. (191). Rezoning of higher order vortex methods. *J. Comput. Phys.*, 97:366–397.

[107] Pareschi, L. (2001). Central differencing based numerical schemes for hyperbolic conservation laws with relaxation terms. *SIAM J. Numer. Anal.*, 39:1395–1417.

[108] Pareschi, L., Puppo, G., and Russo, G. (2005). Central Runge-Kutta schemes for conservation laws. *SIAM J. Sci. Comput.*, 26(3):979–999 (electronic).

[109] Pareschi, L. and Russo, G. (2005). Implicit-Explicit Runge-Kutta schemes and applications to hyperbolic systems with relaxation. *J. Sci. Comput.*, 25(1-2):129–155.

[110] Patlak, C. S. (1953). Random walk with persistence and external bias. *Bull. Math: Biophys.*, 15:311–338.

[111] Perthame, B. (2004). PDE models for chemotactic movements: parabolic, hyperbolic and kinetic. *Appl. Math.*, 49:539–564.

[112] Perthame, B. (2007). *Transport equations in biology*. Frontiers in Mathematics. Birkhäuser Verlag, Basel.

[113] Prescott, L. M., Harley, J. P., and Klein, D. A. (1996). *Microbiology*. Wm. C. Brown Publishers, Chicago, London, 3rd edition.

[114] Puckett, E. G. (1993). Vortex methods - an introduction survey of selected research topics. In Gunzburger, M. and Nicolaides, R., editors, *Incompressible computational fluid dynamics - Trends and advances*, pages 335–407. Cambridge University Press.

[115] Raviart, P.-A. (1985). An analysis of particle methods. In *Numerical methods in fluid dynamics (Como, 1983)*, volume 1127 of *Lecture Notes in Math.*, pages 243–324. Springer, Berlin.

[116] Russo, G. (2005). Central schemes for conservation laws with application to shallow water equations. In *Trends and Applications of Mathematics to Mechanics*, pages 225–246. Springer Milan.

[117] Saito, N. (2007). Conservative upwind finite-element method for a simplified Keller-Segel system modelling chemotaxis. *IMA J. Numer. Anal.*, 27(2):332–365.

[118] Shu, C.-W. (1998). Essentially non-oscillatory and weighted essentially non-oscillatory schemes for hyperbolic conservation laws. In *Advanced numerical approximation of nonlinear hyperbolic equations (Cetraro, 1997)*, volume 1697 of *Lecture Notes in Math.*, pages 325–432. Springer, Berlin.

[119] Strehl, R., Sokolov, A., Kuzmin, D., and Turek, S. (2010). A flux-corrected finite element method for chemotaxis problems. *Computational Methods in Applied Mathematics*, 10(2):219–232.

[120] Sweby, P. K. (1984). High resolution schemes using flux limiters for hyperbolic conservation laws. *SIAM J. Numer. Anal.*, 21(5):995–1011.

[121] Tuval, I., Cisneros, L., Dombrowski, C., Wolgemuth, C. W., Kessler, J. O., and Goldstein, R. E. (2005). Bacterial swimming and oxygen transport near contact lines. *PNAS*, 102:2277–2282.

[122] Tyson, R., Lubkin, S. R., and Murray, J. D. (1999a). A minimal mechanism for bacterial pattern formation. *Proc. Roy. Soc. Lond. B*, 266:299–304.

[123] Tyson, R., Lubkin, S. R., and Murray, J. D. (1999b). Model and analysis of chemotactic bacterial patterns in a liquid medium. *J. Math. Biol.*, 38(4):359–375.

[124] Tyson, R., Stern, L. G., and LeVeque, R. J. (2000). Fractional step methods applied to a chemotaxis model. *J. Math. Biol.*, 41:455–475.

[125] van Kan, J. (1986). A second-order accurate pressure-correction scheme for viscous incompressible flow. *SIAM Journal on Scientific and Statistical Computing*, 7(3):870–891.

[126] van Leer, B. (1979). Towards the ultimate conservative difference scheme. V. A second-order sequel to Godunov's method. *J. Comput. Phys.*, 32(1):101–136.

[127] Velázquez, J. J. L. (2004a). Point dynamics in a singular limit of the Keller-Segel model. I. Motion of the concentration regions. *SIAM J. Appl. Math.*, 64(4):1198–1223 (electronic).

[128] Velázquez, J. J. L. (2004b). Point dynamics in a singular limit of the Keller-Segel model. II. Formation of the concentration regions. *SIAM J. Appl. Math.*, 64(4):1224–1248 (electronic).

[129] Witteveen, J. and Bijl, H. (2009). Explicit mesh deformation using inverse distance weighting interpolation.

[130] Wolansky, G. (2002). Multi-components chemotactic system in the absence of conflicts. *European J. Appl. Math.*, 13:641–661.

[131] Woodward, D., Tyson, R., Myerscough, M., Murray, J., Budrene, E., and Berg, H. (1995). Spatio-temporal patterns generated by S. typhimurium. *Biophys. J.*, 68:2181–2189.